# Photonic Sensor based on Surface-Enhanced Raman Scattering for the Detection of Trace Chemicals

**By**

**Navneet Kaur**

A dissertation submitted to the Faculty of Graduate Studies

Lakehead University

In partial fulfillment of the requirements for the degree of

Doctor of Philosophy

Chemistry and Material Science

Department of Physics

April 2025

# Abstract

The research presented in this thesis describes the development of a three-dimensional (3D) tapered optical fiber-based surface-enhanced Raman scattering (SERS) sensor for detecting trace chemicals. The developed system was capable of detecting rhodamine 6G (R6G) and crystal violet (CV) at Picomolar (pM) levels. A Scanning electron microscope (SEM) and an optical microscope were used to characterize the tapered fiber. The unique characteristics of the fabricated SERS substrate, such as the uniform distribution of analyte around a particular diameter of the fiber and a specific location where maximum SERS intensity was observed, have been presented. The developed sensor was used in the real-time detection of chemicals, allowing immediate adjustments. The detection limit of $10^{-7}$ M for R6G and $10^{-8}$ M for CV was achieved in real time.

A seedless method was used to synthesize gold nanorods (GNRs) with localized surface plasmon resonance (LSPR) closer to the excitation wavelength. The prepared GNRs were tweezed successfully on the tapered fiber surface, and a minimum detectable limit of 10 pM was achieved for CV.

A plasmonic structure using Zinc (Zn) and Zinc Oxide (ZnO) was developed using optical tweezing along the tapered fiber length. The effect of single and double tweezing was investigated. This plasmonic structure has potential applications in biosensing.

# Publications and Contributions

## JOURNAL PUBLICATIONS

1. **N. Kaur** and G. Das, "Three-dimensional plasmonic substrate as surface-enhanced Raman spectroscopy (SERS) tool for the detection of trace chemicals," *Journal of Raman Spectroscopy*, vol. 55, no. 4, pp. 473-480, 2024.
2. **N. Kaur** and G. Das, "Plasmonic structure of zinc (Zn) and zinc oxide (ZnO) on a tapered optical fiber," *Optical Materials Express*, vol. 12, no. 9, pp. 3821-3828, 2022.
3. **N. Kaur,** J. O. Trevisanutto, and G. Das, "Plasmonic structure on a tapered optical fiber for application as a surface-enhanced Raman spectroscopy substrate," *Microwave and Optical Technology Letters*, vol. 63, pp. 2776-2781, 2021.
4. **N. Kaur** and G. Das, "Gold nanorods and their application in Surface-Enhanced Raman Spectroscopy," manuscript preparation is in progress.
5. **N. Kaur** and G. Das, "Real-time detection of chemicals using tapered optical fiber," Revised manuscript to be submitted in *Optica Continuum, 2025*.

## CONFERENCE PROCEEDINGS

1. **N. Kaur,** Varsha, and G. Das, "Surface-enhanced Raman spectroscopy (SERS) for the detection of Rhodamine 6G and Crystal Violet," Optics Biophotonics Congress: Optics in the Life Sciences, DTh2C.7, Vancouver, April 2023.
2. **N. Kaur** and G. Das, "ZnO Plasmonic Structure on a Tapered Optical Fiber," OSA Optical Sensors and Sensing Congress, JTh6A.39, Washington, DC, USA, July 2021.

## CONFERENCES

1. **N. Kaur** and G. Das, “Development of a 3D surface-enhanced Raman scattering (SERS) substrate for the detection and quantification of chemicals at lower concentrations,” ASA, CSSA, SSSA International Annual Meeting, St. Louis, MO, USA, 2023.

2. **N. Kaur** and G. Das, “Optical fiber probe for the detection of chemicals: Rhodamine 6G and Crystal Violet,” Canadian Association of Physicists (CAP), University of New Brunswick, June 2023.

3. **N. Kaur,** Varsha, and G. Das, “Surface-enhanced Raman spectroscopy (SERS) for the detection of Rhodamine 6G and Crystal Violet,” Optica Biophotonics Congress: Optics in Life Sciences, Vancouver, April 2023.

4. **N. Kaur** and G. Das, “ZnO plasmonic structure on a tapered optical fiber,” OSA Optical Sensors and Sensing Congress, Washington, DC, USA, July 2021.

**This thesis is dedicated to my baby daughter, Elaahi Kaur Gill.**

# Acknowledgments

I want to thank my supervisor, Dr. Gautam Das for giving me an opportunity to pursue my research and to be part of the Photonics Research Group at Lakehead University. My gratitude goes to him, as his unwavering support and guidance throughout these years have helped me compile this dissertation. A special thanks to my committee members, Dr. Mark Gallagher and Dr. Justin Jiang, for their regular input and valuable discussions to complete this project successfully.

I would also like to thank all the past and current members of the Photonics Research Group. My time with Dr. Joshua O. Trevisanutto, Varsha, and Dr. Jyothis Thomas was wonderful, and our scientific discussions contributed to achieving the goals.

I want to give a very special thanks to my husband, Simardeep Singh Gill. I am fortunate to have him in my life, as his presence and constant love and support made this journey more beautiful. Words are powerless to thank my beautiful baby girl, Elaahi Kaur Gill, who chose me as her mom and gave me the very important title of “mother.”

The blessings of God and my parents, Parminder Kaur and Avtar Singh, played a crucial role in my well-being and achieving the set targets.

# Contents

**Abstract** ..... II

**Publications and Contributions** ..... III

**Acknowledgments** ..... VI

**Chapter 1** ..... 1

Introduction ..... 1

1.1 Optical Fiber ..... 1

1.2 Tapered Optical Fiber (TOF) ..... 6

1.3 Modes in a Cylindrical Waveguide ..... 10

1.4 Introduction to Raman Spectroscopy ..... 11

1.5 Surface – Enhanced Raman Spectroscopy (SERS) ..... 15

1.6 Developments in the fabrication of fiber & non-fiber-based SERS substrate . 19

1.7 Optical Tweezing (OT) ..... 22

1.8 Thesis Organization ..... 26

**Chapter 2** ..... 31

Three-dimensional (3D) plasmonic substrate as a surface-enhanced Raman spectroscopy (SERS) tool for the detection of trace chemicals ..... 31

2.1 Introduction ..... 31

2.2 Dynamic etching process ..... 35

2.3 Manufacturing fiber-based SERS substrate and its characteristics ..... 40

2.4 Raman Spectroscopy results ..... 43

2.5 Revised dimensions of the tapered fiber ..... 56

2.6 Modifications in the experimental set-up ..... 58

2.7 Conclusion ..... 72

**Chapter 3** ..... 73

Plasmonic structure of zinc (Zn) and zinc oxide (ZnO) on a tapered optical fiber ..... 73

3.1 Introduction ..... 73

3.2 Methodology ..... 76

3.3 Effect of tweezing conditions on the distribution of Zn, ZnO, and GNRs ..... 78

3.4 Conclusion ..... 89
Chapter 4 ..... 91
Gold Nanorods (GNRs) preparation and their applications in SERS ..... 91
4.1 Introduction ..... 91
4.2 Gold nanorods synthesis methods ..... 93
4.3 GNRs synthesis recipe ..... 101
4.4 Instrumentation ..... 108
4.5 CTAB and cytotoxicity of CTAB molecules ..... 113
4.6 Role of each chemical used in the reaction ..... 115
4.7 Surface-Enhanced Raman Scattering (SERS) applications ..... 119
4.8 Conclusion ..... 127
Chapter 5 ..... 129
Real-time detection ..... 129
5.1 Introduction ..... 129
5.2 Methodology ..... 133
5.3 Results and Discussion ..... 135
5.4 Conclusion ..... 140
Chapter 6 ..... 142
Potential Applications of the developed SERS substrate ..... 142
6.1 Introduction ..... 142
6.2 Methodology ..... 143
6.3 Raman spectroscopy results and discussion ..... 144
6.4 Conclusion ..... 151
Chapter 7 ..... 152
Conclusion and Future Work ..... 152

## List of Figures

**Figure 1.1:** Showing the basic structure of an optical fiber (a) cross-section (or front view) and (b) 3D view. ..... 2
**Figure 1.2:** Ray diagram showing the light propagation through an optical fiber [2]..... 4
**Figure 1.3:** Comparison of MMF and SMF [3]. ..... 5
**Figure 1.4:** The image shows the penetration depth, $d_p$, at the core-cladding interface. .. 8
**Figure 1.5:** (a) Schematic and (b) Scanning Electron Microscope (SEM) image of the TOF showing the cladding diameter and tapered length. ..... 9
**Figure 1.6:** The energy level diagram represents three conditions: Stokes, anti-Stokes, and Rayleigh scattering. ..... 14
**Figure 1.7:** Schematic of localized surface plasmon resonance (LSPR) from metal nanosphere. ..... 18
**Figure 1.8:** Schematic of the ray-optic model for the optical tweezers. ..... 24
**Figure 1.9:** SEM image showing the ring structure formed by GNRs (A.R. = 3.8) along the tapered fiber length using optical tweezing. ..... 27
**Figure 2.1:** Schematic depicting the dynamic etching process [88]. ..... 37
**Figure 2.2:** Scanning electron microscope (SEM) image of the tapered optical fiber..... 37
**Figure 2.3:** Electric field distribution of $LP_{01}$ ($HE_{11}$) and $LP_{11}$ ($HE_{21}$) modes in the core and cladding of the fiber. ..... 39
**Figure 2.4:** Schematic of the experimental set-up of optical tweezing. ..... 41
**Figure 2.5:** SEM images showing the GNRs distribution on the tapered optical fiber: (a) random distribution near the tip and (b) denser distribution in the middle region [16]..... 42
**Figure 2.6:** An optical image of the tapered region showing the density variation of GNRs near the tip and middle region (taken by a camera). ..... 43
**Figure 2.7:** Raman spectrum of the R6G powder placed on a coverslip. ..... 44
**Figure 2.8:** Comparing the Raman spectrum near tip region: (a) Fiber+R6G, (b) Fiber+GNRs+R6G. ..... 46
**Figure 2.9:** Schematic of the experimental set-up. ..... 46
**Figure 2.10:** Optical image of a tweezed tapered fiber with sprinkled R6G along the length (taken by a camera). ..... 47
**Figure 2.11:** Comparing the Raman spectrum in the middle region: (a) Fiber+R6G, (b) Fiber+GNRs+R6G. ..... 48
**Figure 2.12:** Raman spectrum excited by 785 nm of ZnO..... 49
**Figure 2.13:** Comparing Raman spectra of ZnO powder: (a) near the tip region and (b) in the middle region. ..... 51
**Figure 2.14:** Schematic of the dip and dry method. ..... 52
**Figure 2.15:** Raman spectra of R6G comparing with and without GNRs for R6G at $10^{-3}$ M concentration. ..... 53

**Figure 2.16**: Raman spectrum of R6G at $10^{-7}$ M concentration in middle region (integration time: 7000 ms and average scans: 5). ..... 54
**Figure 2.17:** (a) Schematic showing the drop-casting method, and (b) diagram showing the evaporation stage of the drop (1) drop just cast, (2) after a few minutes of evaporation, and (3) after complete evaporation. ..... 55
**Figure 2.18:** SEM image showing tip diameter of the probe approx. 35 um with GNRs ring-like structure along the tapered length. ..... 57
**Figure 2.19:** SEM image showing the intact shape of GNRs at the tip. ..... 57
**Figure 2.20:** Schematic showing the experimental set-up of (a) tweezing process and (b) dip and dry process, where height, h of drop size is identical in both cases. ..... 59
**Figure 2.21:** Raman spectra show the intensity variation at nine different angular positions at the specific diameter of (a) the tip region and (b) the middle region of the tapered fiber probe. The inset shows the enlarged view of three peaks. ..... 61
**Figure 2.22:** Schematic showing the details of the experimental set-up to collect Raman spectra from the tapered fiber probe. ..... 62
**Figure 2.23:** Schematic of the tapered fiber showing 12 locations and their distance from the tip. ..... 63
**Figure 2.24:** Stock solution of $10^{-5}$ M concentration of (a) R6G and (b) CV for Raman analysis. ..... 64
**Figure 2.25:** (a) Raman spectra and (b) bar graph representing the uniformity of the SERS intensity at five different angular positions for location 1 for a concentration $10^{-9}$ M of CV at 1170 $cm^{-1}$ characteristic peak [93]. ..... 66
**Figure 2.26:** The trend representing the maximum SERS intensity at location 7, which is 210 μm away from the tip [93]. ..... 67
**Figure 2.27:** SEM image showing the fiber diameter (34.6 μm) where maximum SERS intensity was obtained. The inset shows the distribution of GNRs at that location [93]. ... 68
**Figure 2.28:** Chemical structures of (a) R6G (Sigma Aldrich) and (b) CV (Sigma Aldrich). ..... 69
**Figure 2.29:** SERS spectra comparing different concentrations of (a) R6G ($10^{-8}$ M to $10^{-13}$ M) and (b) CV (Sigma Aldrich) [93]. ..... 71
**Figure 3.1:** SEM image of GNRs and ZnO nanostructure on a carbon tape, (a) ZnO (10's of nm in length and Hexagonal in shape) with GNRs (Length: 67 nm, diameter: 10 nm, AR: 6.7), and (b) magnified image showing the ZnO-NR. ..... 77
**Figure 3.2:** Schematic showing the manufacturing process of the ZnO-NRs and GNRs-based SERS substrate. ..... 78
**Figure 3.3:** SEM image showing the distribution of GNRs and ZnO nanostructures along the tapered fiber length on middle and end regions of the tapered fiber using double tweezing. ..... 79
**Figure 3.4:** SEM image showing the (a) width of the rings and (b) separation between the rings along the tapered fiber length obtained using double tweezing. ..... 80

**Figure 3.5:** An enlarged image of the ring is used to show the ZnO nanostructure and GNRs..... 81
**Figure 3.6**: SEM image showing the ring-like structure along the fiber length obtained using single tweezing (1064 nm). ..... 82
**Figure 3.7:** Optical image showing the ring structure along the tapered fiber after double tweezing. ..... 83
**Figure 3.8:** (a) SEM image showing the patches of ZnO+GNRs along the fiber length, (b) magnified image of the patch to show ZnO and GNRs distribution, and (c) EDS results confirming the presence of Zn and O. ..... 85
**Figure 3.9:** UV-visible spectrum of ZnO. ..... 85
**Figure 3.10:** XRD spectrum of ZnO nanostructure. ..... 86
**Figure 3.11:** Comparing absorption spectra of ZnO with or without CTAB. ..... 87
**Figure 3.12:** TEM image of the ZnO nanostructure. ..... 88
**Figure 3.13:** SEM image of Zn dust on a carbon tape. ..... 89
**Figure 3.14:** An SEM image showing the plasmonic structure of Zn and GNRs was obtained using single tweezing. Inset is the magnified image of one of the rings. ..... 89
**Figure 4.1:** An experimental set-up shows the mixing of CTAB in water using a stirring hot plate. ..... 104
**Figure 4.2:** Color of the solution (a) right after the reaction and (b) after five and half hours of reaction (or before centrifugation). ..... 105
**Figure 4.3:** (a) sketch showing centrifuge vials (red color shows sedimentation (also known as an original solution after re-dispersing in water) after centrifuging the solution for 10 minutes at 14,500 rpm, (b) the original picture of the vial showing precipitation at the bottom after centrifugation (supernatant was removed). ..... 106
**Figure 4.4:** Original (O) and supernatant (S) solutions were .5 minutes at 14,500 rpm. 107
**Figure 4.5:** Centrifuged (O), (S), and (S1) solutions for 18 minutes at 14.500 rpm..... 108
**Figure 4.6:** (a) Original (O), (b) supernatant (S), and supernatant (S1) solution color appearance after centrifugation. ..... 109
**Figure 4.7:** UV-visible absorption spectra comparing (O), (S), and (S1) solutions. ..... 110
**Figure 4.8:** TEM image of the lab-prepared GNRs (mean AR = 3.6 ± 0.6). ..... 110
**Figure 4.9:** TEM image of GNRs showing the inter-planar spacing, d= 0.20 nm, (b) profile confirming the value of interplanar spacing, d. ..... 112
**Figure 4.10:** SEM image showing the GNRs distribution on the tapered fiber. ..... 120
**Figure 4.11:** Magnified SEM image showing the intact GNRs on the fiber surface. .... 120
**Figure 4.12:** SEM-EDS analysis confirming the presence of gold on the specific segment (red circle) of a tapered fiber tweezed with synthesized GNRs. ..... 122
**Figure 4.13:** Optical image of a tapered fiber, which shows the distribution of synthesized GNRs along the length when tweezed using 1064 nm laser wavelength (taken using a phone camera). ..... 123
**Figure 4.14:** Microscope set-up. ..... 124

**Figure 4.15:** SERS spectra of CV comparing two concentrations ($10^{-3}$ M and $10^{-11}$ M). ..... 124
**Figure 4.16:** Raman spectra comparing lab-prepared and Nanopartz GNRs for CV at $10^{-3}$ M concentration. ..... 126
**Figure 4.17:** Comparing Raman spectra of two locations (locn_1 and locn_2) for the same fiber with $10^{-3}$ M concentration of CV. ..... 127
**Figure 5.1:** Experimental set-up for real-time detection. ..... 134
**Figure 5.2:** Raman spectra from R6G powder using flat-end fiber for alignment check. ..... 135
**Figure 5.3:** Comparing Raman spectra of different concentrations ($10^{-1}$ M to $10^{-7}$ M) of R6G in GNRs solution using bare fiber for real-time detection. ..... 136
**Figure 5.4:** Comparing Raman spectra of different concentrations ($10^{-3}$ M to $10^{-9}$ M) of R6G in water solution using tweezed fiber for real-time detection. ..... 137
**Figure 5.5:** Comparing Raman spectra of different concentrations ($10^{-3}$ M to $10^{-9}$ M) of CV in GNRs solution using bare fiber for real-time detection. ..... 139
**Figure 5.6:** Comparing Raman spectra of different concentrations ($10^{-3}$ M to $10^{-9}$ M) of CV in water solution using tweezed fiber for real-time detection. ..... 140
**Figure 6.1:** (a) Molecular structure of Glyphosate (Sigma Aldrich, Canada), and (b) Raman spectra comparing different concentrations ($10^{-2}$ M to $10^{-4}$ M) of Glyphosate mixed in ethanol. ..... 146
**Figure 6.2:** (a) Molecular structure of Xanthohumol (Sigma Aldrich, Canada), and (b) Raman spectra comparing different concentrations ($10^{-4}$ M to $10^{-6}$ M) of Xanthohumol mixed in ethanol. ..... 147
**Figure 6.3:** Raman spectra represent the uniformity in intensity at five angular positions of location 7. ..... 148
**Figure 6.4:** Image of the hops plant at LUARS. ..... 150
**Figure 6.5:** Image of (a) hops flower, (b) leaf, and (c) raisins present on the leaf. ..... 150
**Figure 6.6:** Raman spectra showing peaks for three different types of hops plants. ..... 151

## List of Tables

**Table 1:** Table showing the concentration and volume of each chemical used in the seedless method to prepare GNRs. ..... 102

## List of Abbreviations

AR: Aspect Ratio

AMPA: Aminomethylphosphonic Acid

ALD: Atomic Layer Deposition

AgNPs: Silver Nanoparticles

AuNPs: Gold Nanoparticles

BDAC: Benzyldimethylexadecylammoniumchloride

CE: Chemical Enhancement

CMC: Critical Micelle Concentration

CT: Charge Transfer

CTAB: Cetyltrimethylammonium Bromide

CV: Crystal Violet

CVD: Chemical Vapor Deposition

EDS: Energy Dispersive Spectroscopy

EM: Electromagnetic mechanism

FDA: Food and Drug Administration

GC: Gas Chromatography

GC-MS: Gas Chromatography with Mass Spectroscopy

GLY: Glyphosate

GNRs: Gold Nanorods

HF: Hydrofluoric

HOMO: Highest Occupied Molecular Orbital

HPLC: High Performance Liquid Chromatography

IR: Infrared

LoD: Detection Limit

LSPR: Localized Surface Plasmon Resonance

LI-SERS: Liquid Interface assisted SERS

LUARS: Lakehead University Agricultural Research Station

LUMO: Lowest Unoccupied Molecular Orbital

MMF: Multi Mode Fiber

NA: Numerical Aperture

NCP: Narrow Channel Processor

ND: Neurodegenerative Disease

NIs: Nanoislands

NRs: Nanorods

NSs: Nanospheres

ORC: Oxidation and Reduction Cycling

OT: Optical Tweezing

PCF: Photonic Crystal Fiber

PD: Parkinson's Disease

PEG-SH: Polyethylene Glycol thiols

PLD: Pulsed Laser Deposition

R6G: Rhodamine 6G

Rh B: Rhodamine B

RSD: Relative Standard Deviation

RTP: Rotating Tube Processor

SANS: Small Angle Neutron Scattering

SAXS: Small Angle X-Ray Scattering

SEM: Scanning Electron Microscope

SERS: Surface-Enhanced Raman Spectroscopy

SM: Single Molecule

SMF: Single Mode Fiber

SPR: Surface Plasmon Resonance

TEM: Transmission Electron Microscope

TIR: Total Internal Reflection

TOF: Tapered Optical Fiber

TSPR: Transverse Surface Plasmon Resonance

UV-Vis: Ultraviolet-Visible

XN: Xanthohumol

XRD: X-Ray Diffraction

3D: Three-Dimensional

4-ATP: 4-Aminothiophenol

4-MBA: 4-Mecraptobenzoic Acid

Intensity: Intensity (counts), Raman Intensity/Arbitr. Units

# Chapter 1

# Introduction

## 1.1 Optical Fiber

Optical fiber is a thin cylindrical waveguide with a solid cylindrical core of refractive index $n_1$. The core is surrounded by a coaxial cylinder of refractive index, $n_2$, known as the cladding. Another layer, the outer jacket (also known as buffer coating), around the cladding provides extra strength to the optical fiber and makes it more robust. According to the fundamental laws of optics, the most critical parameter of any transparent medium is the refractive index, n. The well-known Snell's law governs the refraction of light at the interface between two transparent media. In optical fiber design, the core has a higher refractive index than the cladding, and the light transmitted through the core follows the principle of "Total Internal Reflection" (TIR). Light propagating in the optical fiber, which satisfies the TIR at the core-cladding interface, remains confined in the core and propagates along the fiber length. Based on the explanation from electromagnetic theory, tunneling of optical energy through the interface is possible, and the wave that carries this energy is called the evanescent wave.

Figure 1.1 shows an optical fiber's cross-sectional and three-dimensional (3D) view. The concept of the optical fiber was first introduced in 1966 by K. C. Kao [1]. The material used to manufacture fiber is either glass (silica) or plastic.

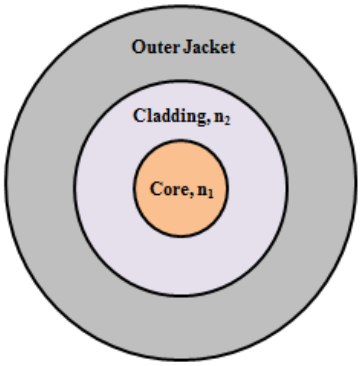


(a)

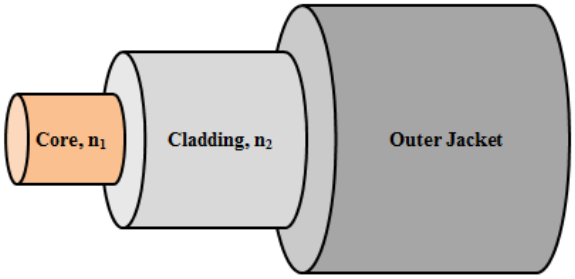


(b)

**Figure 1.1:** Showing the basic structure of an optical fiber (a) cross-section (or front view) and (b) 3D view.

Figure 1.2 shows the ray optics representation of light propagation in an optical waveguide. An incident ray falls on the core, $n_1$, from the outer medium of refractive

index, n, at angle Θ with respect to the fiber axis. The ray propagates inside the fiber core and follows TIR when ϕ is greater than the critical angle ($\phi_c$). Also, the angle of incidence Θ should be less than or equal to the acceptance angle ($\Theta_{max}$). If a ray strikes the interface outside of the acceptance angle, it will be refracted to the cladding, as illustrated in Figure 1.2. The critical angle ($\phi_c$) can be obtained by applying Snell's law as given in equation (1), which supports the TIR [2]:

$$\sin(\phi_c) = n_2/n_1 \quad (1)$$

The amount of light propagated through the fiber depends on the acceptance angle $\Theta_{max}$. The value of the acceptance angle is:

$$n \sin \Theta_{max} = NA = \sqrt{(n_1^2 - n_2^2)} \quad (2)$$

The term NA in equation (2) is the numerical aperture, which determines the light-gathering capacity of an optical fiber and is also helpful for calculating the source-to-fiber power coupling efficiencies. The NA is a dimensionless quantity with values ranging from 0.14 to 0.5. NA can also be described in terms of the relative refractive index, Δ of an optical fiber (equation 3) [2].

$$NA = n_1\sqrt{2\Delta} \quad (3)$$

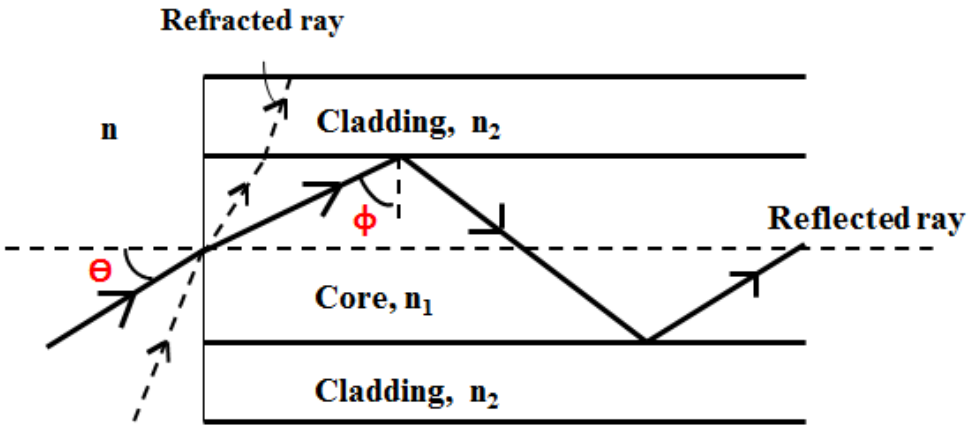


**Figure 1.2:** Ray diagram showing the light propagation through an optical fiber [2].

After understanding the basic theory, it is important to know the applications and properties of optical fibers. Optical fibers have several advantages for communication as they have higher information-carrying capacity than coaxial copper cable or microwave systems. Another attraction for optical fibers is their low manufacturing cost and lightweight along with the low transmission loss (0.2 dB/km), which is advantageous in telecommunication [3]. Unlike copper cables, the signal propagating through the optical fiber does not interfere with other signals, and they are easy to install and cost-effective to transport. Therefore, it has attracted defense, banking, etc., fields to provide high signal security at incredibly high speed. Along with telecommunication, optical fibers play an important role in advancing chemical sensing, medical imaging, and biosensing, which opens doors to exploring more opportunities.

While choosing the manufacturing materials for the optical fibers, several factors should be considered based on the respective applications, such as flexibility, durability, weather conditions, ruggedness, cost, etc. Optical fibers can be manufactured using glass

or plastic. Glass fibers are generally made of oxide glasses such as silicon dioxide ($SiO_2$), and plastic fibers are made of polymers (such as polymethyl methacrylate (PMMA) and polystyrene). This work utilized glass fibers as they offer a high melting point, and glass remains intact up to several hundred degrees centigrade. Another advantage of glass fibers is that they transmit visible and infrared light. $SiO_2$ fiber has a refractive index of 1.458, which can be varied by adding dopants to the silica. The most used dopants are boric oxide ($B_2O_3$), germanium oxide ($GeO_2$), or phosphorous pentoxide ($P_2O_5$). The glass core's refractive index can be increased by adding $GeO_2$ and $P_2O_5$, whereas doping with $B_2O_3$ decreases it [2].

Depending on the size of the core and the modes supported by an optical fiber, they can be classified into two types:

1. Single-mode fiber (SMF)
2. Multi-mode fiber (MMF)

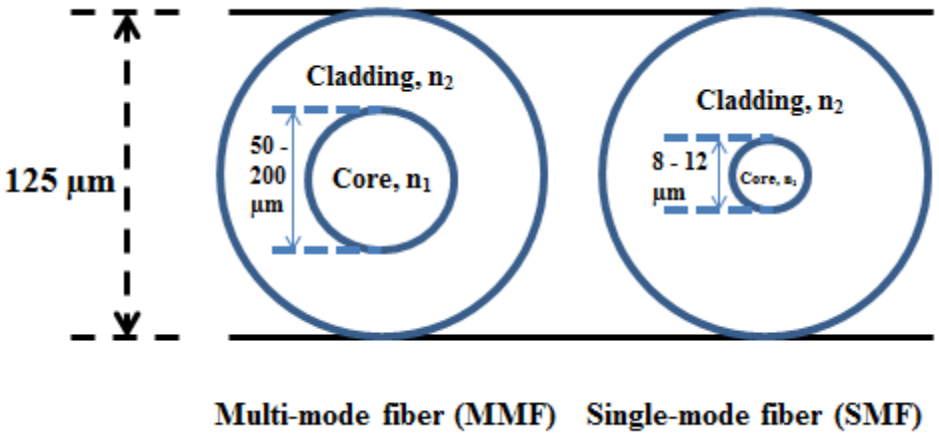


**Figure 1.3:** Comparison of MMF and SMF [3].

Single-mode fiber's core diameter is smaller, ranging from 8 – 12 μm, and allows only one mode to propagate, i.e., the fundamental mode $LP_{01}$ or $HE_{11}$ mode. Because of their large transmission bandwidth, SMFs are widely used for long-haul communications. On the other hand, the core diameter of MMF is 50 – 200 μm and used for short-distance communications. The MMF supports hundreds of modes to propagate in the fiber, and each mode travels with a different group velocity. Therefore, modes launched at the same time will reach the other end of the fiber at slightly different times. This time delay among many modes in MMF causes the optical signal to broaden as it propagates and is known as intermodal or multipath dispersion. Group velocity, $v_g = 1/(d\beta/d\omega)$ where $\beta$ is the propagation constant, which depends on the mode and fiber design (SMF or MMF), and $\omega$ is the angular frequency of the wave, is the key concept to understanding the intermodal dispersion. This phenomenon limits the use of MMF in long-haul communications. Both fibers have their advantages. Fiber optical sensors offer a wide range of benefits such as being lightweight, cost-effective, highly sensitive, unaffected by electrical signals, and free from corrosion. This technology has been used in many areas, including healthcare, environmental monitoring, food security, and defense [4-6].

## 1.2 Tapered Optical Fiber (TOF)

Until this point, the discussion was centered on classic optical fibers, which are cylindrical. There is another approach where the shape of these cylindrical fibers can be manipulated based on their applications. The tapered optical fiber (TOF) is one example that has potential applications in biosensing by enabling the label-free detection of

biomolecules [7]. The other important field in which TOF finds an application is monitoring the contamination in food and water bodies, which can impact both human and aquatic life. Due to the TOF sensor's compact size, light weight, cost-effectiveness, high stability, and ability to study remotely, it has become an attractive field of research in many areas, which includes the preparation of SERS (Surface-Enhanced Raman Spectroscopy) substrates [8], trapping yeast cells [9], glucose sensing [10], biological and chemical sensing [11].

A TOF can be prepared using various methods such as heat and pulling, polishing, chemical etching [12]. As discussed previously, the launched light remains confined in the core while propagating, and the evanescent field decays exponentially in the cladding. The light must interact with the fiber's surrounding medium for sensing applications. This can be achieved by removing the cladding and exposing the core to the outer medium, where the evanescent field can come out and interact with the surrounding environment, which will now act as the cladding (air, water, etc.). Figure 1.4 shows the penetration depth, $d_p$, which is the distance the evanescence field extends beyond the core-cladding interface. At this distance, the evanescent field decreases to 1/e of its value at the interface [13]. Equation 4 is the mathematical expression of the penetration depth, $d_p$:

$$d_p = \frac{\lambda}{2\pi\,(n_1^2 sin^2\phi - n_2^2)^{1/2}} \qquad (4)$$

Where $\lambda$ is the wavelength of the light source, $n_1$ and $n_2$ are the refractive indices of the core and cladding, respectively, and $\phi$ is the incident angle of the light at the core-cladding interface [13].

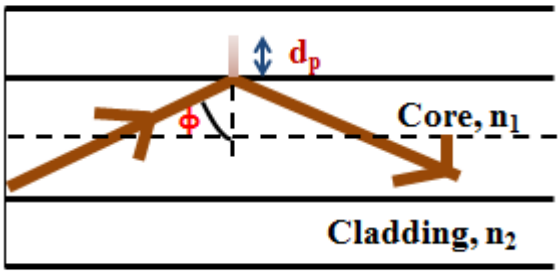


**Figure 1.4:** The image shows the penetration depth, $d_p$, at the core-cladding interface.

In this research, the dynamic etching method [12,14,15] was used to obtain the tapered shape of the optical fiber. In the dynamic etching process, 1.5 ml of hydrofluoric (HF) acid of 50% concentration was used to etch the cylindrical fiber. Along the length of the tapered region (Figure 1.5), the core of the optical fiber was exposed to the outer medium, which acts as cladding.

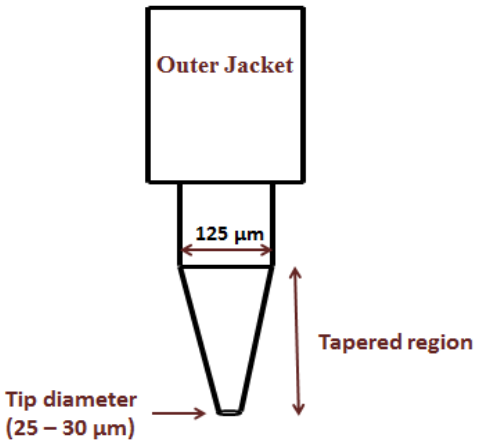


(a)

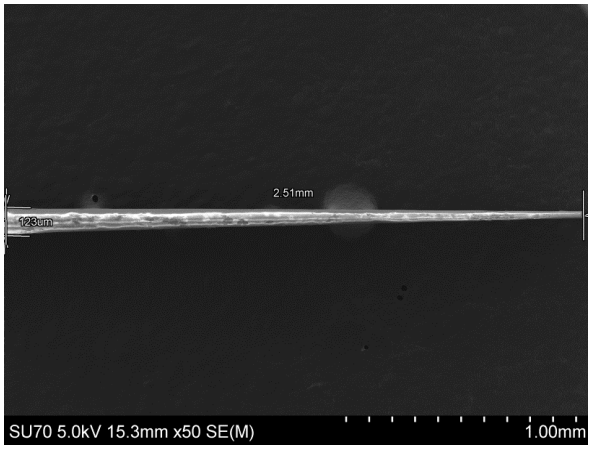


(b)

**Figure 1.5:** (a) Schematic and (b) Scanning Electron Microscope (SEM) image of the TOF showing the cladding diameter and tapered length.

To prepare the tapered fiber, the following steps have been followed: (a) an MMF with core and cladding diameters of 110 μm and 125 μm, respectively, were used, (b) about 1 cm of the buffer jacket was stripped away using the fiber stripper, and debris was cleaned using alcohol, (c) a flat end of the fiber was prepared using a fiber cleaver, (d) the cleaved section was then immersed perpendicularly in HF acid which was covered with an organic solvent (iso-octane) to prevent the evaporation of the acid into the atmosphere, (e) the fiber was then pulled from the acid using a translational stage controlled by computer software at a specific speed to obtain the desired length and tip diameter of the TOF. The length of the tapered fiber varies according to the withdrawal speed [16]. The characteristics of the TOF (e.g., tapered length, tip diameter, etc.) were studied using a Scanning Electron Microscope (SEM).

## 1.3 Modes in a Cylindrical Waveguide

The ray model described in section 1.2 was used to understand light propagation through optical fibers. However, it is crucial to solve Maxwell's equations to better understand optical fibers' optical power propagation mechanism. When solving these equations, one will get the characteristic parameters such as propagation constant, V-number, and mode field distributions [16]. In general, the mode field is the distribution of the electromagnetic field within the core and cladding. The propagation constant, β, is one of the key parameters characterizing the phase velocity and guiding conditions of each mode in an optical fiber, is defined as:

$$\beta = \frac{2\pi n_{eff}}{\lambda} = k\, n_{eff} \tag{5}$$

where $k$ is the propagation vector, $n_{eff}$ is the effective refractive index, and λ is the wavelength of the light in a vacuum. A mode remains guided if β follows the following condition:

$$n_2 k \leq \beta \leq n_1 k \tag{6}$$

where $n_1$ and $n_2$ are the refractive indices of core and cladding, respectively, and $k = 2\pi/\lambda$. If $\beta \leq n_2 k$ then the power comes out of the core as it propagates along the fiber and leaks into the cladding region. These are called “leaky modes,” which contain significant power in short fibers [2].

Another vital parameter on which the number of modes the fiber supports depends is the V number. V number can be expressed as follows:

$$V = \frac{2\pi a}{\lambda}\sqrt{(n_1^2 - n_2^2)} = \frac{2\pi a}{\lambda} NA \quad (7)$$

where a is the core radius, and V is a dimensionless quantity.

The number of modes (M) supported by the fiber can be expressed in terms of V as follows:

$$M = \frac{V^2}{2} \quad (8)$$

Under the weakly guided approximation (i.e., where the core and cladding refractive index difference (Δ), $\Delta < 0.01$), an optical fiber with $V < 2.405$ supports only the fundamental mode. If the core is exposed to the surrounding medium for sensing applications, such as tapered optical fiber (TOFs), resulting in significantly large Δ. Under these conditions, weakly guided approximation no longer holds, and one must solve the vector wave equation. Once V exceeds 2.405, the fiber can guide multiple modes and be classified as MMF [2].

## 1.4 Introduction to Raman Spectroscopy

Due to its numerous advantages, Raman spectroscopy has been chosen for research applications in optical fiber-based sensing. Raman spectroscopy is an important technique that uses the inelastic scattering of light to determine the structural information

of a molecule. Scattering is a process that causes electromagnetic waves to deviate from their original path due to interactions with the molecules. When monochromatic light interacts with matter, two types of scattering occur: (a) elastic or Rayleigh scattering and (b) inelastic or Raman scattering. Elastic scattering occurs when the scattered photon has the same energy (same wavelength or frequency) as the incident light that struck the sample. Therefore, the molecule returns to its original energy state after the interaction, causing no net energy exchange between the light and the molecule. Inelastic or Raman scattering occurs when the scattered photon has a different energy than the incident light that interacted with the sample. This energy difference corresponds to the molecule's vibrational (or rotational) energy changes. As a result, the scattered light shifts in frequency or wavelength, which enables Raman spectroscopy to fingerprint specific molecular vibrations.

In 1923, a German physicist, A. Smekel, first predicted Raman scattering [17]. Later, an Indian physicist, Sir Chandrasekhara Venkata Raman (1888 – 1970), experimentally observed the inelastic scattering effect in 1928 [18]. Raman was awarded the Nobel Prize in 1930 for his contribution to the scattering of light, and the discovery was named after him, known as the “Raman effect”. The ability of Raman scattering to analyze samples non-destructively, with minimal sample preparation, has made Raman spectroscopy incredibly useful in scientific and industrial domains.

Figure 1.6 illustrates the Rayleigh and Raman scattering via an energy-level diagram and is explained below:

1. Photon absorption (virtual state): A photon from incident monochromatic light excites the molecule from its ground vibrational state to a short-lived virtual energy state.

2. Stokes Raman scattering: If, after the interaction, the scattered photon has less energy than the incident photon, it means the molecule has gained this energy and transitioned to a higher vibrational level. Thus, the scattered photon has a longer wavelength or lower frequency. This process is called Stokes Raman scattering.

3. Anti-Stokes Raman scattering: If the molecule is already in an excited state before interaction (only possible for a fraction of thermally excited molecules), it might lose some of the vibrational energy to the scattered photon. Thus, the scattered photon will gain energy and have a shorter wavelength or higher frequency. This process is called anti-Stokes Raman scattering.

At a given temperature, the distribution of molecules across various vibrational energy levels follows Boltzmann distribution. The fraction of molecules in a particular excited vibrational state ν is proportional to $\exp\left(-E_\nu / k_B T\right)$, where $E_\nu$ is the vibrational energy of that state, $k_B$ is the Boltzmann constant, and T is the absolute temperature. In Raman scattering, Stoke lines are usually much stronger than the anti-Stoke lines at or near room temperature. This is due to the population of the molecules in the first excited vibrational state (which is a requirement for anti-Stokes emission) follows the Maxwell-Boltzmann distribution law and being much less than relative to the ground state. Hence, fewer photons undergo anti-Stoke scattering, making these lines less intense [17,19].

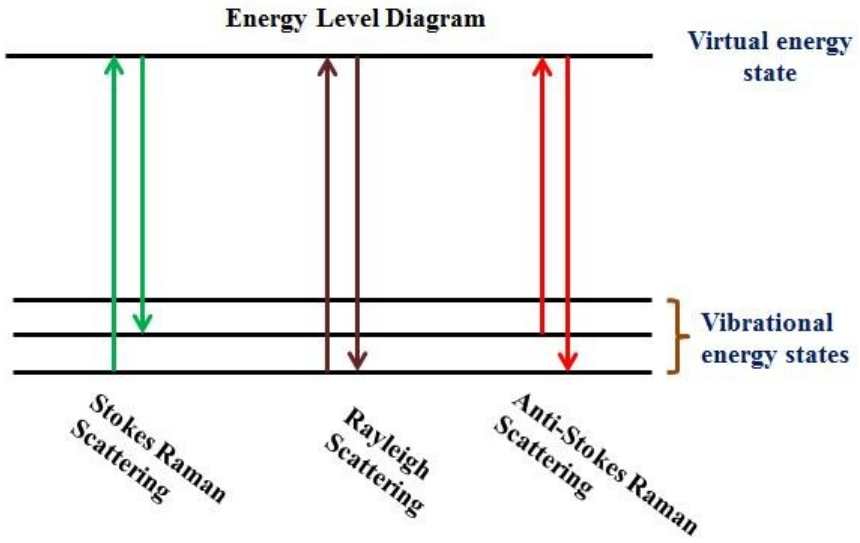


**Figure 1.6:** The energy level diagram represents three conditions: Stokes, anti-Stokes, and Rayleigh scattering.

What is the significance of the Raman shifts? The frequency shift of the scattered photon relative to the incident photon tells how much vibrational energy was either gained or lost by the molecule during the scattering process. These are named Raman shifts and produce characteristic fingerprint peaks to identify the molecular bonds. Since each compound has unique vibrational energies, Raman spectroscopy became a powerful tool for characterizing and identifying known or unknown compounds in chemistry, biology, and industrial settings.

In 1934, G. Placzek [17] proposed the classical theory, also known as polarizability theory, to explain the Raman effect. From electrostatics, one knows that incident electromagnetic radiation can induce a dipole moment when light interacts with a material. The strength of the induced dipole moment, μ, is:

$$\mu = \alpha \bar{E} \qquad (9)$$

where α is the polarizability of the molecule, and $\bar{E}$ is the electric field's strength. Polarizability describes the ease with which the electron cloud of a molecule can be distorted, and it is a material property that depends on the molecular structure and the nature of the bonds. For a molecule or vibrational transition to be Raman active, the molecule should undergo a change in polarizability during the vibration [17,20].

## 1.5 Surface – Enhanced Raman Spectroscopy (SERS)

The Raman signal is generally very weak, as only 1 in $10^7$ photons is inelastically scattered. One method of increasing the intensity of the Raman signal involves a roughened metallic substrate. The first observation of Surface – Enhanced Raman Spectroscopy (SERS) was made by Fleischmann and co-workers in 1974 when an enhanced Raman signal was obtained by adsorbing pyridine molecule on a silver electrode roughened using successive oxidation-reduction cycles [21]. They proposed that to study the molecules on the electrode surface, it is necessary to have a high surface area on the roughened metallic surface. Later, in 1977, Jeanmaire et al. and Creighton et al. confirmed that a significant Raman intensity was observed when a roughened metallic substrate was used and enhancement was obtained of the order $10^6$. Most early studies for SERS focused on pyridine on roughened silver electrodes [22,23]. Various preliminary experiments have shown that SERS is a 'nanostructured effect,' not so much of a 'surface effect,' and M. Moskovits demonstrated the role of surface plasmon resonances in SERS [24].

The exact nature of the enhancement of Raman signals is not fully known. However, of the numerous mechanisms to explain SERS, electromagnetic enhancement (EM) and chemical enhancement (CE) are two widely accepted mechanisms. The EM mechanism is the more dominant because the enhancement of the Raman signal arises from localized surface plasmon resonance (LSPR), which involves the excitation of conduction band electrons localized on a metal particle by electromagnetic radiation, inducing a collective oscillation. The localized surface plasmon resonance (LSPR) effect generates a high-energy field at the metal particle surface; however, this high-energy field decays rapidly in space with increasing distance from the surface. Consequently, the incident electromagnetic field acting on an analyte molecule adsorbed onto the metal particle's surface is amplified by this high-energy field. Therefore, the analyte that is in close proximity to the metallic particle will experience an increase in field intensity compared with those molecules not in close proximity. This increase in field intensity experienced by an analyte molecule will result in an enhanced Raman scattered signal [25-29]. Typically, chemical enhancement in SERS is believed to stem from the formation of chemical bonds, resonance phenomena, and light-induced charge transfer (CT), which occurs between the molecules and the substrate [30-32]. These effects can potentially influence the geometric or electronic structure of the adsorbed molecules, resulting in detectable shifts in spectra and changes in intensity. The charge transfer (CT) in SERS refers to the phenomenon where electrons are transferred between the analyte molecule and the metal substrate, resulting in enhanced Raman signals. Based on the chemical enhancement theory, CT is believed to contribute to SERS enhancement factors and was first demonstrated by Gersten and co-workers in 1979 [33]. When a molecule is adsorbed

onto a metal surface, photo-induced electrons can be either excited from the highest occupied molecular orbital (HOMO) to the Fermi level of the metal or from the Fermi level of the metal to the lowest unoccupied molecular orbital (LUMO) of the molecule [25].

SERS has a significant scope in the field of nanoscience and nanotechnology. The discovery of SERS has produced enormous interest in metallic nanoparticles whose dimensions are smaller than the mean free path of electrons and have dielectric constants different from the bulk metal. To create strong surface plasmon resonances (SPR), experiments are commonly performed with coinage metals such as copper (Cu), silver (Ag), and gold (Au) because they are noble and d-d band transitions make them fall in the visible part of the spectrum. This property makes them ideal for SERS and related applications because the excitation source (e.g., visible laser) can match the metal's plasmon resonance, thereby amplify the electromagnetic fields around nanoparticles surfaces. To understand SERS and its capabilities, one must understand the mechanism for LSPR in metallic nanoparticles.

The electric field from incoming light creates a dipole in the metallic nanoparticle by separating the charges within the particle. There is a restoring force trying to compensate for this displacement. When the dipole oscillation caused by these forces is in resonance with the frequency of the incident light, a LSPR has been achieved. This resonance condition results in more absorption, which leads to the enhancement of the electric field and becomes a key to SERS's high sensitivity [34,35]. Also, metal nanoparticles possess unique optical properties dependent on their size, shape, and dielectric environment [36,37]. The different shape of the nanoparticle produces different

LSPR frequencies [38]. Figure 1.7 shows that the free electrons in a metal nanosphere oscillate at a frequency determined by the incident light. This figure represents the example of a metallic nanosphere or nanoparticle.

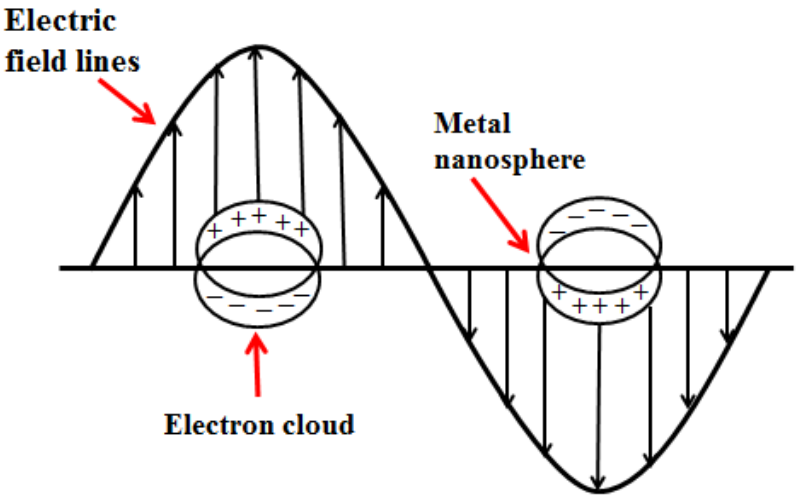


**Figure 1.7:** Schematic of localized surface plasmon resonance (LSPR) from metal nanosphere.

The symmetric shape of a metallic nanosphere gives a single LSPR wavelength dependent upon its material and diameter. For example, when the diameter of the gold spherical particle was 20 nm, LSPR was observed at ∽ 520 nm, which is due to gold's electron density, its dielectric properties, and symmetry of the nanoparticles [39]. The present research used gold nanorods (GNRs) for SERS substrate preparation on a tapered optical fiber. The anisotropic shape of GNRs is advantageous because it allows two localized surface plasmon resonance frequencies, i.e., one along the diameter (transverse)

and the other along the length (longitudinal) of the nanorod [40]. The LSPR of the GNRs can be tuned by varying the aspect ratio (AR = length to diameter ratio) of the nanorod.

## 1.6 Developments in the fabrication of fiber and non-fiber-based SERS substrate

In the present world, human health and environmental safety are of the utmost concern worldwide. Toxic or hazardous materials such as harmful chemicals used in the food industry, infectious or poisonous chemicals thrown into water bodies, explosives that are a threat to mankind, etc., which are capable of risking both human and environmental health, are essential to detect and control at a very early stage.

Several methods have been used in detecting trace chemicals, such as gas chromatography (GC), high-performance liquid chromatography (HPLC) with mass spectroscopy (MS), and gas chromatography with mass spectroscopy (GC-MS) [41]. These above-mentioned methods require expensive instrumentation, sample pre-treatment and trained personnel. However, SERS, being a non-destructive technique which is highly sensitive, eliminates all the above-discussed drawbacks [41]. Further, the high sensitivity and specificity of SERS lead to the possibility of a single-molecule (SM) detection [42]. In research findings, it was concluded that the sensitivity of the metallic nanomaterials-based SERS substrates can be manipulated by their shape, size, and the distance between these particles [43-48].

The non-optical fiber-based SERS substrates encompass a variety of materials and structures designed to enhance the Raman signal. The most common techniques for

manufacturing SERS-optimized substrates include nanosphere, on-wire, electron-beam (e-beam), and nanoimprint lithography. Among all the lithographic methods, e-beam lithography provides high stability and reproducibility. However, the maintenance of the lab equipment is expensive, and a tedious process [49]. Other methodologies used in developing SERS substrates are (a) oxidation and reduction cycling (ORC) – in this method, repeated oxidation-reduction cycles are applied to the silver (Ag) surface to prepare a rough surface at the nanoscale level [21], electrochemical roughening – in this method metallic surfaces are placed in a highly acidic solution which helps to roughen them [50]. In 2022, Zhen et al. [51] proposed a 2-dimensional SERS substrate where a molybdenum carbide ($Mo_2C$) film was prepared using the chemical vapor deposition (CVD) method. A finite element method and density functional theory was used to demonstrate the theoretical analysis. The detection limit for R6G and CV was $10^{-8}$ M and $10^{-6}$ M, respectively. In 2022, Sugioka and co-workers manufactured a highly sensitive SERS device for the early-stage detection of virus infections and Alzheimer's disease [52]. A unique liquid interface-assisted SERS (LI-SERS) method was applied to adsorb the analyte molecules on the SERS substrate. This substrate was able to detect the biomolecules in the range of pM-fM. In one of the most recent articles, Zhang et al. developed a flexible SERS substrate and achieved $10^{-12}$ M detection limit for R6G [53]. Also, the SERS substrate was used to detect pollutants such as ziram and 2-naphthalene thiol in apple juice and lake water. Soma et al. presented a review from the last 3-4 years describing the recent developments of SERS substrates, which are highly efficient in detecting toxic materials such as explosives, drugs, dyes, pesticides, etc. [54]. In reference 52, Pei et al. shows the work done by researchers to develop sensitive and flexible SERS

substrates using paper/filter paper, cotton buds, 3-D sponge, nanofiber mat, fabric, etc. It provides a comprehensive report on substrates and their detection limit and suggests that many research advancements are possible in this field.

Optical-fiber-based SERS substrates are an alternative to traditional substrates where a highly sensitive 3D substrate can be manufactured [55]. Various chemicals used in agriculture and textiles industries are harmful and require monitoring and detection, such as pesticides (which may leave residue on fruits and vegetables) and dyes (which may drain into the water bodies and harm both human and aquatic life) [56]. The regulatory agencies (e.g., FDA) have set a minimum allowable limit on these chemicals. In 2016, Zhang et al. reported an optical fiber-based probe by deposition of Ag nanoparticles (AgNPs) on the tapered fiber tip by chemical deposition. The AgNPs were not uniformly distributed on the nanoprobe and obtained a $10^{-7}$ M sensitivity for the R6G [57]. In 2019, Ran et al. demonstrated the development of fiber-based SERS probes, where silver-coated gold nanostars (Au@Ag NSs) were coated onto the flat end of the fiber, which gives a detection limit of $10^{-8}$ M for Rhodamine B (Rh B) [58]. In 2020, Milenko et al. proposed and demonstrated a fiber probe with micro-lensed multimode optical fiber and gold nano-film. The probe showed a detection limit of $10^{-7}$ M for the R6G [59]. In 2022, Yu et al. fabricated a SERS substrate based on the tapered optical fiber on which AgNPs were coated using multiple cycle light-induced deposition technology, and the reported limit of detection for R6G was $10^{-11}$ M [60]. In 2014, Liu et al. developed a 3D SERS substrate by decorating the flat fiber end with approximately 100 nm AgNPs using polymerization and a thermal-induced process. The CV detection limit was $10^{-7}$ M [61]. In 2015, Xie et al. developed a 3D optical fiber-based SERS sensor using Au nanoparticles

and nanogratings. They used nanoscale 3D printing technology, thermal evaporation, and UV pulse laser irradiation to detect $10^{-6}$ M crystal violet (CV) in ethanol solution [62]. Zhou et al. 2020 reported an optical fiber SERS probe where Au nanorods were deposited using a laser-induced evaporation self-assembly method. The minimum detection limit for CV and R6G was $10^{-8}$ M and $10^{-10}$ M, respectively [63]. In 2021, Gu et al. proposed the fabrication of dense monolayer AuNPs on the end face of the optical fiber using a seed-mediated growth method for SERS and obtained a detection limit for both CV and R6G down to $10^{-8}$ M [64]. Despite the various existing SERS substrates, there are still opportunities to manufacture a compact and cost-effective SERS substrate that can provide high sensitivity, stability, and reproducibility.

## 1.7 Optical Tweezing (OT)

In 1986, Arthur Ashkin first reported the trapping of dielectric particles using a single-beam gradient force radiation-pressure trap, and this phenomenon is known as 'Optical Tweezing' (OT) [65]. In 2018, he was awarded a Nobel Prize for his pioneering work. In his experiment, a cell in a water solution was trapped using a spatially filtered argon-laser light at 514.5 nm. The laser was directed through a high-numerical-aperture (NA = 1.25) water-immersion microscope objective, which focused a strongly converging beam downward into a glass cell filled with water. The experiment also reported that a 10 μm glass sphere (refractive index = 1.6) was trapped in water by using fluorescence to show the trajectories of the incident and scattering light beams. In the study, dielectric particles (size in the range of 25 nm to 10 μm) in a water solution were trapped. In 1978, A.

Ashkin reported for the first time the stable trapping, cooling, and manipulation of the atoms using a single-beam gradient force radiation-pressure particle trap [66]. Two intense laser beams from opposite sides were focused on an atomic-sized particle to create the trap. These results confirm the principles of optical tweezers (OTs), which further became a powerful tool in various research fields. In 1987, A. Ashkin and co-workers proposed the trapping and manipulation of biological samples, e.g., viruses and bacteria, using a visible laser, which was further changed to infrared (IR) light so that less optical damage would be caused to the living cells. Providing a damage-free environment, the reproduction of yeast cells and Escherichia coli (E. coli) was observed, and this technique opened up numerous doors in microbiology [67].

Ray optics can help describe the trapping of dielectric particles where the transfer of momentum from refracted light results in two forces: (a) gradient force and (b) scattering force. Figure 1.8 illustrates the optical trapping of a dielectric particle using a ray diagram based on the principles of refraction and optical momentum transfer. The size of the particle (diameter, d) is larger than the incident light (wavelength, $\lambda$) and follows the Mie regime. Light carries momentum ($P = h/\lambda$), and when the direction of light changes due to refraction, the photon's momentum also changes and corresponds to a force ($F = dP/dt$). The diagram shows that a laser beam converges through a high NA lens and diverges again below the laser focus. Both rays, a and b, undergo refraction, causing a momentum change in the photons. Therefore, according to the law of conservation of momentum, the particle will experience a reaction force ($F_a$ and $F_b$) in the opposite direction to momentum change ($dP_a$ and $dP_b$). The resulting force, gradient force ($F_{grad}$), or trapping force, generally pulls the particle towards the highest intensity region

(beam waist). Also, some of the light is reflected or scattered by the particle, creating a force along the beam's propagation direction, known as scattering force ($F_{scat}$). The dielectric particle will move towards laser focus (in the upward direction) when $F_{grad} >> F_{scat}$ and will be stably trapped [65].

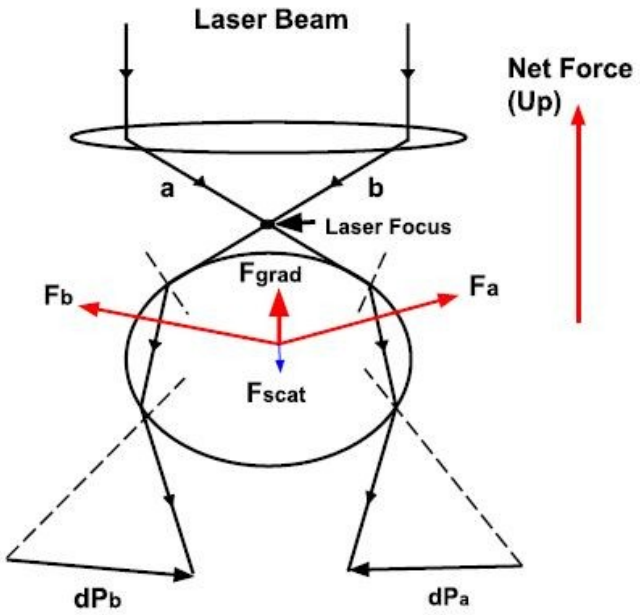


**Figure 1.8:** Schematic of the ray-optic model for the optical tweezers.

In the case of metallic particles, the electromagnetic field induces the dipole moment ($p = n_m^2 \alpha E$, where p is the induced dipole moment, $n_m$ is the refractive index of the surrounding medium, α is the electric dipole polarizability tensor, and E is the incident electric field), which causes the particle to move and rotate. In the case of a simple plane wave, optical forces were divided into two components: gradient force and scattering force [68].

A laser beam interacting with metallic nanoparticles experiences two forces [69]:

1) **Gradient force ($F_g$):**

$$F_g = \frac{1}{4} Re\ (\alpha) \nabla |\varepsilon|^2 \qquad (10)$$

where α is the electric polarizability of the particle, and ε is the electric field's complex amplitude.

2) **Scattering force** $(F_s)$:

$$F_s = \sigma_{ext} \frac{n_2}{c} S \qquad (11)$$

where $\sigma_{ext}$ is the extinction cross-section, c is speed of light, $S$ is the Poynting vector, and $n_2$ is the refractive index of the outer medium.

The basic principle of optical trapping states that for stable trapping, the magnitude of the gradient force should exceed the scattering force [69]. How is the trapping of dielectric particles different from the trapping of metallic particles? Since refraction is the basis of the optical trapping for dielectric particles, light gets reflected in the case of metals, leading to large radiation pressure and the inability to generate enough gradient force. However, in 1994, K. Svoboda and S. M. Block experimentally demonstrated that Rayleigh particles (particle size smaller than the incident wavelength) can be stably trapped in 3D using optical tweezers. Also, the magnitude of the gradient force depends on the particle's polarizability; the scattering force depends on the beam's intensity as well as the square of the polarizability [70].

In this work, optical tweezing was used to develop a SERS substrate. We demonstrated that the developed SERS substrate can detect trace chemicals.

## 1.8 Thesis Organization

### 1.8.1 Objective of the thesis

In this research, ***the main objective was to develop a cost-effective, compact, sensitive and easy to operate 3-dimensional (3D) tapered optical fiber (TOF) based SERS substrate to detect harmful chemicals at very low concentrations in real-time.*** The chemicals that were tested with the prepared SERS substrate are listed as below:

**(a) Rhodamine 6G (R6G)** - a synthetic dye that is being used in food, cosmetic, pharmaceutical, and plastics industries.

**(b) Crystal Violet (CV)** - which is being used in aquaculture to prevent diseases and infections in fish and seafood farming because of its anti-parasitic and anti-microbial properties.

**(c) Glyphosate** - a widely used herbicide which has carcinogenic effects.

**(d) Xanthohumol** - a compound found in Humulus lupulus, also called hops that contribute to the bitter flavor of hops.

To accomplish the goal, an optical fiber-based 3D SERS substrate or SERS probe was manufactured following a dynamic etching and optical tweezing (OT) process, which

was first demonstrated by the Photonics Research Group at Lakehead University [15]. This significant achievement was made by etching cylindrical optical fiber to a nanometer tip (∽ 100 nm), which was then successfully covered with GNRs along the tapered fiber length using Optical Tweezing (OT). In the optical tweezing process, a laser (1064 nm-8.4 mW) was used and the evanescent wave traps GNRs (AR= 3.8) onto the fiber surface. A ring (or grating-like) structure was observed along the tapered fiber length, which was confirmed by using a Scanning Electron Microscope (SEM) as shown in Figure 1.9, which is known as a plasmonic structure.

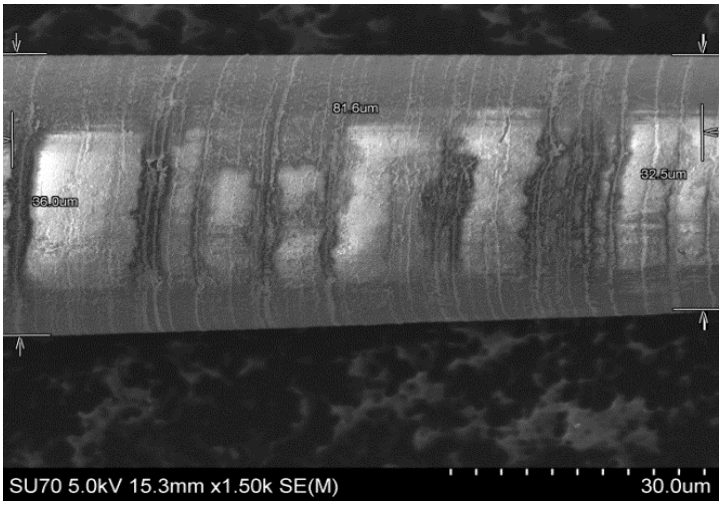


**Figure 1.9:** SEM image showing the ring structure formed by GNRs (A.R. = 3.8) along the tapered fiber length using optical tweezing.

### 1.8.2 Contributions

In this chapter, we discussed the fundamental design, principle, and types of optical fiber. It briefly describes tapered optical fiber (TOF) preparation and its characteristics. The basics of Raman Spectroscopy, SERS, and optical tweezing have been presented in detail

as different methods for developing the fabrication of fiber and non-fiber-based SERS substrates. The following chapters describe the research work and accomplishments.

**Chapter 2** explains the preparation of a three-dimensional SERS substrate using a dynamic etching process and optical tweezing. The dip and dry method has been used for analyte adsorption on the SERS substrate, and a detailed description has been given. The unique features of the fabricated SERS sensor are also presented. The results for the minimum detectable limit (LoD) for two chemicals, R6G and CV, are shown down to the pico-molar level.

This research work was published in:

1. N. Kaur and G. Das, "Three-dimensional plasmonic substrate as surface-enhanced Raman spectroscopy (SERS) tool for the detection of trace chemicals," *Journal of Raman Spectroscopy*, vol. 55, no. 4, pp. 473-480, 2024.

2. N. Kaur, J. O. Trevisanutto, and G. Das, "Plasmonic structure on a tapered optical fiber for application as a surface-enhanced Raman spectroscopy substrate," *Microwave and Optical Technology Letters*, vol. 63, pp. 2776-2781, 2021.

**Chapter 3** describes the preparation of Zn and ZnO-based plasmonic structures along the fiber length using optical tweezing. The effect of single and double tweezing conditions on the distribution of Zn and ZnO was explored.

This research work was published in:

1. N. Kaur, and G. Das, "Plasmonic structure of zinc (Zn) and zinc oxide (ZnO) on a tapered optical fiber," *Optical Materials Express*, vol. 12, no. 9, pp. 3821-3828, 2022.

**Chapter 4** includes the synthesis of small gold nanorods using the seedless method; their characterization and applications in SERS were determined. A simple and reproducible recipe was given, and LoD was determined using lab-synthesized GNRs.

1. N. Kaur and G. Das, "Gold nanorods and their application in Surface-Enhanced Raman Spectroscopy," Manuscript preparation in progress.

**Chapter 5** reports the application of the developed TOF in the real-time detection of chemicals. Two cases were explored: (i) Bare tapered fiber (TOF) was dipped in the analyte and GNRs solution, and (ii) tweezed TOF was dipped in the analyte solution. The LoD for both cases using two chemicals was determined.

1. N. Kaur and G. Das, "Real-time detection of chemicals using tapered optical fiber*,"* Revised manuscript to be submitted in *Optica Continuum, 2025*.

**Chapter 6** includes the Raman spectra of two critical chemicals, Glyphosate and Xanthohumol, which have significant interest in agriculture. Also, Raman spectra obtained from HOPs flowers from homegrown hops plants are presented, which will help build a database for chemicals in hops.

The partial research work was presented at a conference where two chemicals (Glyphosate and Xanthohumol) were bought from Sigma Aldrich, Canada:

1. N. Kaur and G. Das, “Development of a 3D surface-enhanced Raman scattering (SERS) substrate for the detection and quantification of chemicals at lower concentrations”, ASA, CSSA, SSSA International Annual Meeting, St. Louis, MO, USA, 2023.

**Chapter 7** concludes the research work and discusses the future direction of this project.

# Chapter 2

## Three-dimensional (3D) plasmonic substrate as a surface-enhanced Raman spectroscopy (SERS) tool for the detection of trace chemicals

*Optical fiber-based SERS sensors can detect trace chemicals with high sensitivity and selectivity.* ***This chapter discusses*** *the fabrication technique of the 3D tapered optical fiber-based SERS substrate (also known as SERS probe). The "dip and dry" method is introduced, which describes adsorbing the analyte along the tapered fiber length. The step-by-step procedure is discussed to achieve the best sensitivity for the widely used probe molecule rhodamine 6G (R6G). The unique characteristics and features of the developed substrate will be discussed, which include the sensitivity of R6G and crystal violet (CV).*

## 2.1 Introduction

As discussed in the previous chapter, Raman spectroscopy is an inelastic light scattering technique that provides the molecules' vibrational fingerprint and structural

characteristics. Minimal sample preparation is required to obtain Raman Spectroscopy of a chemical. It has contributed to understanding the chemical composition of substances in solid, liquid, and gaseous states [71,72]. However, the Raman signal is weak, and it is difficult to detect when the amount of substance is at low concentrations [73]. The first breakthrough in the field of SERS happened in 1974 when M. Fleischmann first reported the Raman spectra of pyridine adsorbed at an electrochemically roughened silver electrode [21]. In 1977, Van Duyne and co-workers reported an enhancement factor of $10^6$ due to the roughened metallic surface. It took them many attempts and several rejections to publish this work because, at that time, the concept of surface-enhancement was not believed. This work was eventually published in 1977, demonstrating that the strong Raman signal was due to the roughness of metal surfaces, and this phenomenon was later called surface-enhanced Raman scattering or SERS [22]. To justify Van Duyne's work, other groups confirmed and reported similar results independently [23]. Despite the invention, Duyne's first paper did not mention the SERS term. Still, later, it became a standard terminology whenever enhanced Raman scattering happens due to the roughened metallic surfaces.

In 1985, Martin Moskovits [25] did comprehensive review on SERS, based on hundreds of molecules adsorbed on different metal surfaces, such as copper (Cu), silver (Ag), gold (Au), lithium (Li), sodium (Na), potassium (K), indium (In), aluminum (Al), platinum (Pt), and rhodium (Rh). Ag is the most studied metal for SERS; however, because of its lower chemical stability, specifically for biosensing, it is preferable to use gold. The discovery of SERS made researchers interested in preparing and characterizing SERS active nanomaterials.

SERS requires preparing a roughened metallic surface that enhances or amplifies the Raman signal from the adsorbed molecule. This section will focus on nanomaterials instead of the previous chapter, in which SERS substrates were generally described. Over the years, many researchers prepared different-sized and shaped nanomaterials for use as SERS substrates, e.g., silver nanospheres [74,75], gold nanoparticles [76], gold nanorods [77,78], gold nanocubes [79], and gold nanostars [80]. Controlling the particle's shape and size allows one to tune the LSPR peak of nanoparticles effectively. LSPR is a phenomenon that occurs when metallic nanomaterials absorb and scatter light at different wavelengths. It arises from the collective oscillation of free electrons on the metal surface when excited by incident light. These oscillations create an electromagnetic field around the particle; with the particle size < 100 nm, the free electrons are confined to the particle surface, known as a localized surface plasmon. The resonance condition occurs when the incident light's frequency matches the plasmon frequency in the nanoparticle. At this condition, the nanoparticle's absorption and scattering of light are enhanced significantly [81,82]. Gold nanorods have unique properties as their plasmon band, or LSPR, can be tuned in the both visible and near-infrared portions of the electromagnetic spectrum by adjusting the aspect ratio.

Many researchers spent decades unraveling the effect of the roughened metallic surface, which enhances the Raman scattering of the molecule. After years of debate, it was established that two mechanisms should be taken into consideration:

a) a electromagnetic (EM) enhancement mechanism, and
b) a chemical enhancement or charge-transfer (CT) mechanism.

Although the above two phenomena have different or independent modes of operation, they still occur simultaneously [81]. In 2008, Van Duyne and co-workers reviewed the factors contributing to enhancing the Raman signal and agreed that the EM enhancement mechanism is the dominant factor in SERS [48]. The EM enhancement mechanism affects the Raman scattering intensity because the scattering intensity is proportional to the square of the induced dipole moment, $\mu_{ind}$, which is proportional to the incident field, E (equation 9, **Chapter 1**). A more detailed explanation for both the EM enhancement mechanism and CT can be found in **Chapter 1**.

After adsorbing the analyte on the SERS substrates, the Raman signal is amplified based on the EM and CT mechanisms. The magnitude of the EM and CT enhancement is affected by material, shape, size, and arrangement of nanostructures on the substrate. Therefore, choosing a reproducible, reliable, stable, highly sensitive, and cost-effective SERS substrate is essential for successful chemical detection.

Compared with conventional Raman spectroscopy, SERS can amplify the Raman signal up to $10^{14}$-$10^{15}$ times, and in 1997 made it possible to detect a single molecule (SM) [83,84]. In the initial stage of SERS, most substrates were fabricated using (a) oxidation and reduction cycling – where repeated oxidation-reduction cycles are applied to metallic (Ag) surface to obtain nanoscale roughness [21], (b) electrochemically roughened electrodes - where metallic surfaces are kept in a highly acidic solution to chemically roughen the metallic surfaces [50].

Why the detection of chemicals at the trace level is important? As we know, various chemicals used in agriculture and textile industries, such as pesticides – residue

on fruits and vegetables, and dyes – drained into water bodies can harm humans and aquatic life, which is the matter that needs utmost attention. Regulatory agencies such as the Food and Drug Administration (FDA) have set a minimum allowable limit on these chemicals or a complete ban on a few due to their toxicity and potential risk of causing genetic change. Two chemicals, rhodamine 6G (R6G) and crystal violet (CV), are widely used in the food and textile industries. R6G is also highly used in the cosmetic, pharmaceutical, and plastic industries. Due to the growing demand for aquaculture products, manufacturers use CV because of its anti-parasitic and anti-microbial properties to prevent diseases and infections in fish and seafood farming. Although these chemicals are not permitted in the food industry, they are still readily available as they are widely used in the textile industry, coupled with regulatory monitoring. Also, waste disposal from industries negatively impacts aquatic and human life. Therefore, it is important to have highly efficient and sensitive methods to detect them at low concentration [56,85,86].

## 2.2 Dynamic etching process

In the following section, we discuss the manufacturing process of the optical fiber-based SERS substrate. The tapered shape of an optical fiber was obtained from the cylindrical-shaped multi-mode fiber (MMF) with core and cladding diameters of 110 μm and 125 μm, respectively, using a simple and low-cost, dynamic etching method. First, one centimeter of fiber jacket was removed using a fiber stripper, and isopropyl alcohol was used to clean the debris. In the next step, a fiber cleaver was used to make the flat end, and a microscope was used to ensure the cleaved end was flat. The prepared flat end was

then immersed perpendicularly in 50% hydrofluoric (HF) (∽1.5 ml) acid, readily available from commercial vendors, and stored in a plastic vial with a lid. Covering the HF acid with organic solvent during the etching process is crucial to protect the surroundings from harmful vapors [87]. In this case, a layer of iso-octane was used on top of the HF, which not only keeps the environment free from contamination but also maintains the acid height in the vial to get consistent dimensions (tapered length and tip diameter). In the final step, the fiber was withdrawn at a specific speed to obtain the tapered fiber's desired length and tip diameter.

Figure 2.1 shows the schematic of the dynamic etching process, where fiber was held using a homemade fiber holder connected to a vertical translational stage controlled by computer software. In the previous work, the dimensions of the tapered fiber and its effect on the GNRs distribution along the fiber length was explored, and it was suggested that the length of the tapered fiber should be greater than 1 mm; otherwise, GNR shape will not be intact after tweezing [16]. The proposed method provides reliable and reproducible tapered fibers. The tapered fiber was characterized using a scanning electron microscope (SEM), as shown in Figure 2.2.

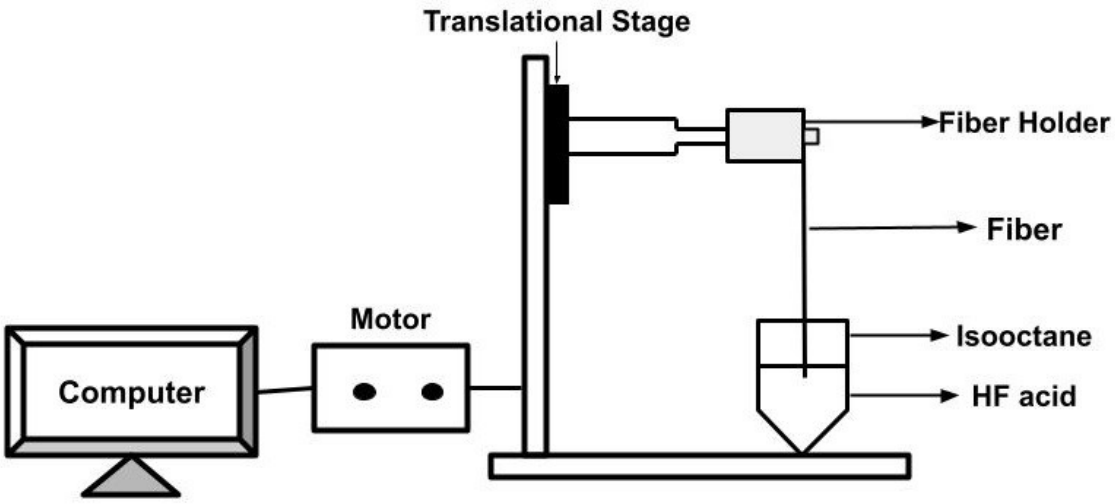


**Figure 2.1:** Schematic depicting the dynamic etching process [88].

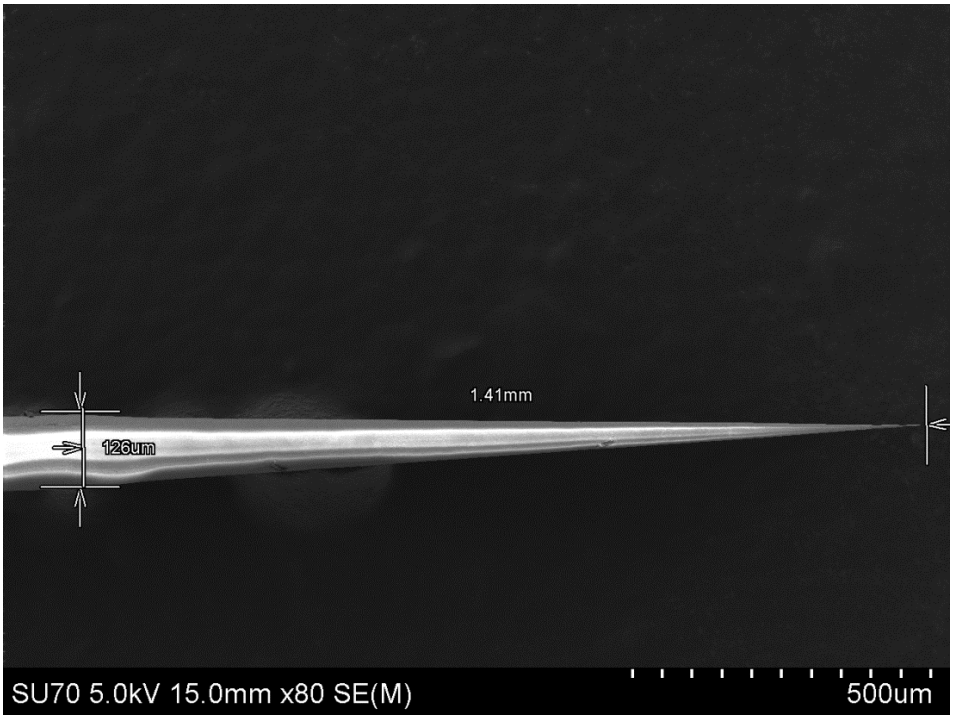


**Figure 2.2:** Scanning electron microscope (SEM) image of the tapered optical fiber.

A more detailed discussion about the characteristics of the tapered optical fiber compared to **Chapter 1** will follow here. The tapering of cylindrical fiber allows the electromagnetic radiation typically confined to the core to have a stronger interaction with the surrounding medium outside the dielectric waveguide. The light propagation through tapered fibers can be understood by using the concept of modes and mode-field distribution. A MATLAB simulation tool was used to obtain the mode-field distribution for different modes, solving Maxwell's vector equation (Downloaded with permission from MATLAB toolbox) [89]. Figure 2.3 illustrates how light in $LP_{01}$ (or $HE_{11}$) fundamental mode does not experience any loss and stays in the fiber until the tip, whereas $LP_{11}$ (or $HE_{21}$) mode experiences loss of light in the cladding, which in the tapered region is the surrounding medium. The number of modes coming out of the tapered region depends on the tapered slope. Therefore, in the tapered region, the evanescent wave interacts with the surrounding environment, which has chemical and biosensing applications [16].

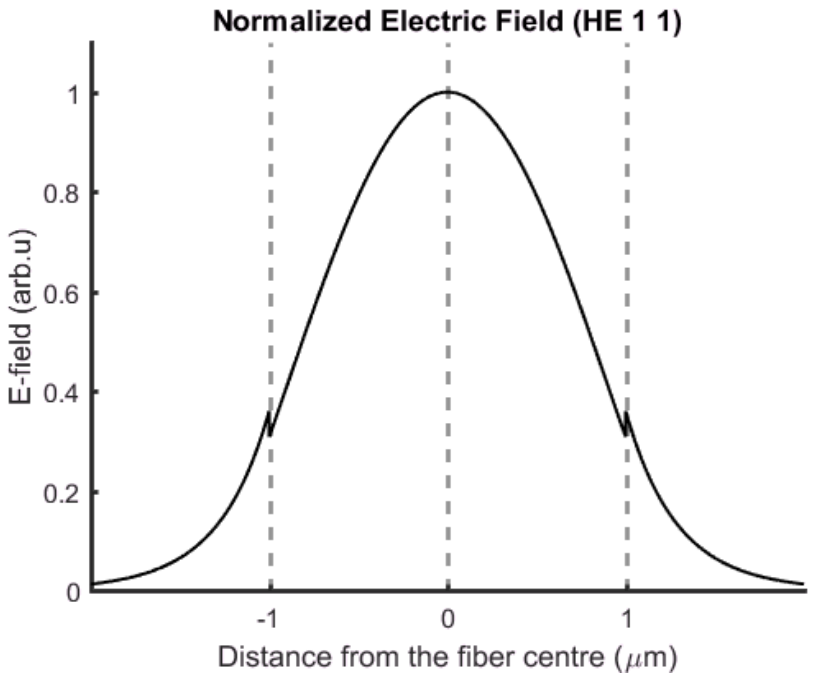


(a)

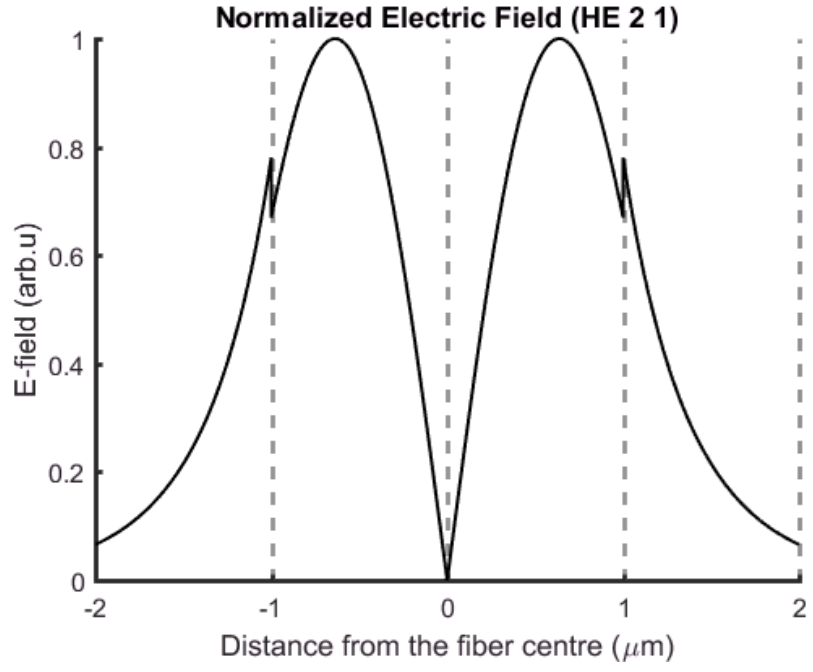


(b)

**Figure 2.3:** Electric field distribution of LP $_{01}$ ($HE_{11}$) and $LP_{11}$ ($HE_{21}$) modes in the core and cladding of the fiber.

## 2.3 Manufacturing fiber-based SERS substrate and its characteristics

Once a tapered fiber with optimum dimensions is prepared, the next step is to create a rough metallic surface along the tapered fiber length, an essential requirement for SERS. As discussed earlier, there are several methods to do so, but in this case, a method known as optical tweezing (OT) was used. A. Ashkin pioneered the field of trapping atoms and received the Nobel Prize in Physics in 2018 [65,[90] using a laser beam, which became a versatile tool in physics and biology. This process is more desirable than the other existing methods because of its miniaturized and simple set-up, effectiveness, high flexibility, and capability to manipulate the distribution of metallic nanostructures by changing the laser wavelength.

Figure 2.4 demonstrates the process of optical tweezing where a laser at 1064 nm wavelength with 8.5 mW power was used to tweeze GNRs on the tapered fiber surface. The laser light was coupled to the untapered end of the fiber, and the tapered end was immersed in a 250 µl drop of GNRs (AR = 6.4) solution placed on the microscope coverslip. The light propagating through the core will escape out in the tapered region, known as an evanescent field, and interact with the GNR solution. The evanescent field produces gradient and scattering forces, and optical tweezing occurs when the gradient force is greater than the scattering force. Kaur et al. explained the physics behind these forces and how they compel the GNRs to deposit on the fiber surface and form a ring-like plasmonic structure [16]. GNRs get deposited on the fiber surface and form a ring-like plasmonic structure when the magnitude of the gradient force is greater than the

scattering force [91]. It is essential to have optimum laser coupling to the fiber's core at the untapered end.

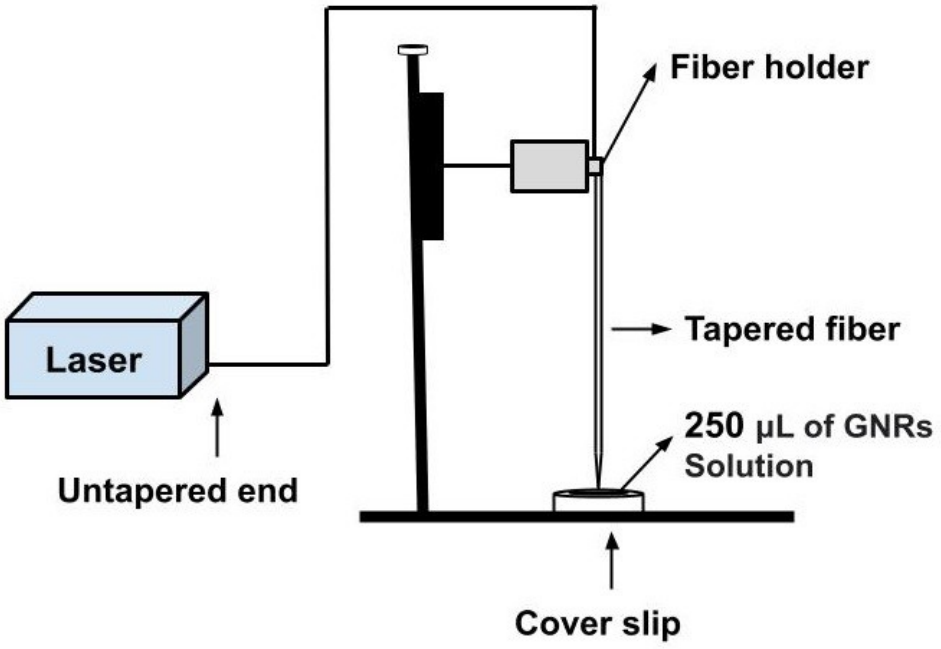


**Figure 2.4:** Schematic of the experimental set-up of optical tweezing.

The tapered fiber was divided into three regions: tip (~100 nm – 16 µm) region, middle (16 µm – 30 µm) region, and end (30 µm – 45 µm) region based on the observation of the GNRs distribution. The characteristics of the tapered fiber were studied using SEM. Figures 2.5 (a) and (b) show an enlarged view of the GNRs distribution near the tip (lighter) and middle (consistent rings), respectively. The GNRs density is different in these three regions because of the number of modes and their interference at the particular location of the tapered fiber. The density variation of the GNRs was observed where the middle region is more significantly covered with GNRs than the tip region. Figure 2.6 is the optical image of the developed SERS substrate.

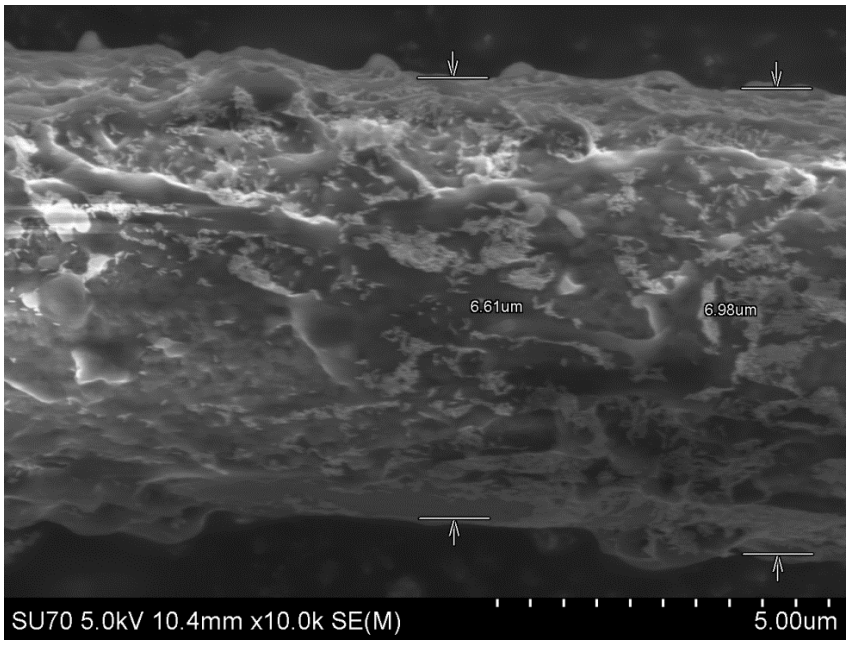


(a)

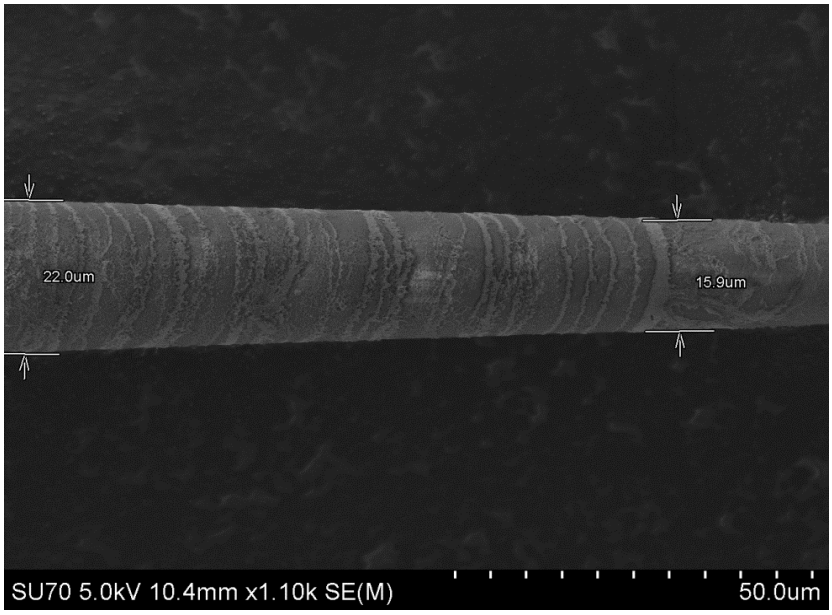


(b)

**Figure 2.5:** SEM images showing the GNRs distribution on the tapered optical fiber: (a) random distribution near the tip and (b) denser distribution in the middle region [16].

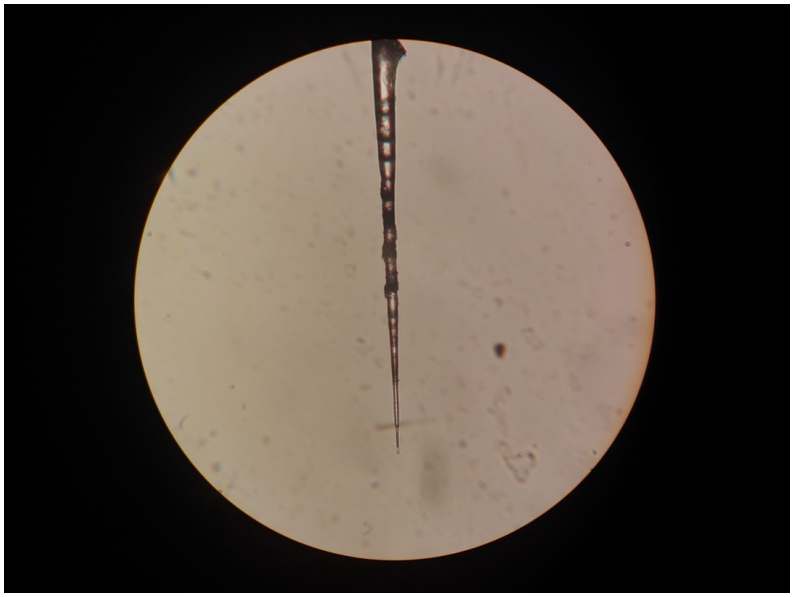

**Figure 2.6:** An optical image of the tapered region showing the density variation of GNRs near the tip and middle region (taken by a camera).

## 2.4 Raman Spectroscopy results

Two methods were followed to adsorb an analyte on the prepared substrate: (a) sprinkling and (b) dip and dry. Before putting the analyte on the fiber surface, a large mass of the chemical Rhodamine 6G (R6G) was placed on the microscope coverslip to obtain the Raman spectrum, which was used as a reference (Figure 2.7). R6G was used as a probe molecule to study the performance of the prepared tweezed optical fiber.

An Ocean Optics Raman System[1] was used to obtain the Raman spectra. The excitation laser wavelength is 785 nm with a default working distance of 7.5 mm.

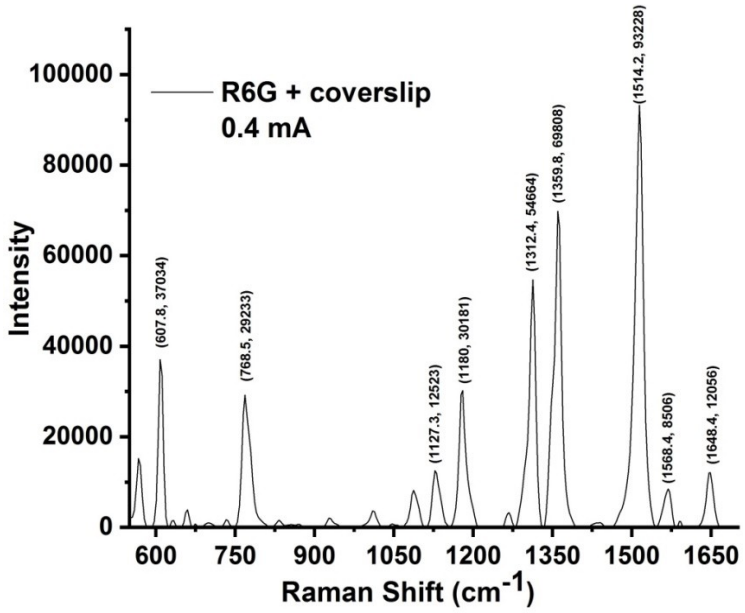


**Figure 2.7:** Raman spectrum of the R6G powder placed on a coverslip.

### 2.6.1 Sprinkling method

Figure 2.8 (a) and (b) show the Raman spectra of the sprinkled R6G near the tip region without and with GNRs, respectively. R6G was taken on a clean spatula (washed with isopropyl alcohol) and was brought on top of the fiber (which was held horizontally using a fiber holder under the excitation laser) and then was shaken so that fine powder could settle onto the fiber surface. Figure 2.9 shows the schematic of the experimental set-up used to collect data from the tweezed fiber covered with the analyte (green dots on the

[1] Ocean Insight, QE Pro Raman Series

tweezed fiber tip show the analyte molecules). In both regions, the diameter of the fiber is extremely small, which means it can hold only a tiny amount of analytes, especially near the tip. It was verified using a probe camera, as shown in Figure 2.10, to obtain an optical image. The intensity count was higher when the GNRs were present, and many distinguishable Raman peaks were visible. Figure 2.11 (a) and (b) show the Raman spectra recorded in the middle region without and with GNRs when R6G was sprinkled. In this region, the GNRs distribution is much denser than the tip region, and the intensity count also reaches a higher number. These results confirmed that the prepared plasmonic structure on the tapered fiber can behave as a powerful SERS tool to enhance the Raman signal.

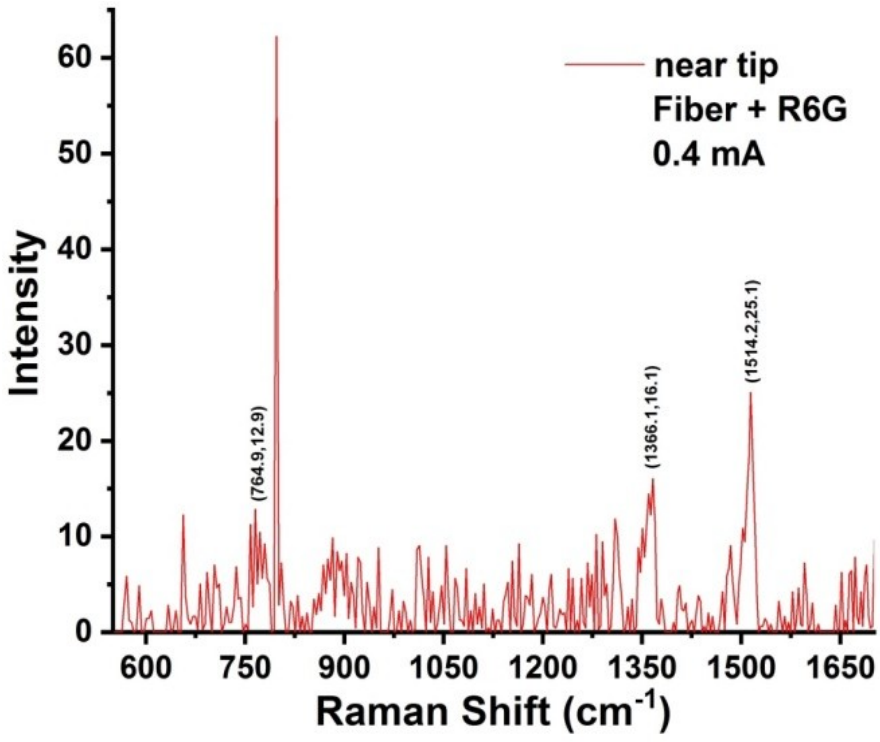


(a)

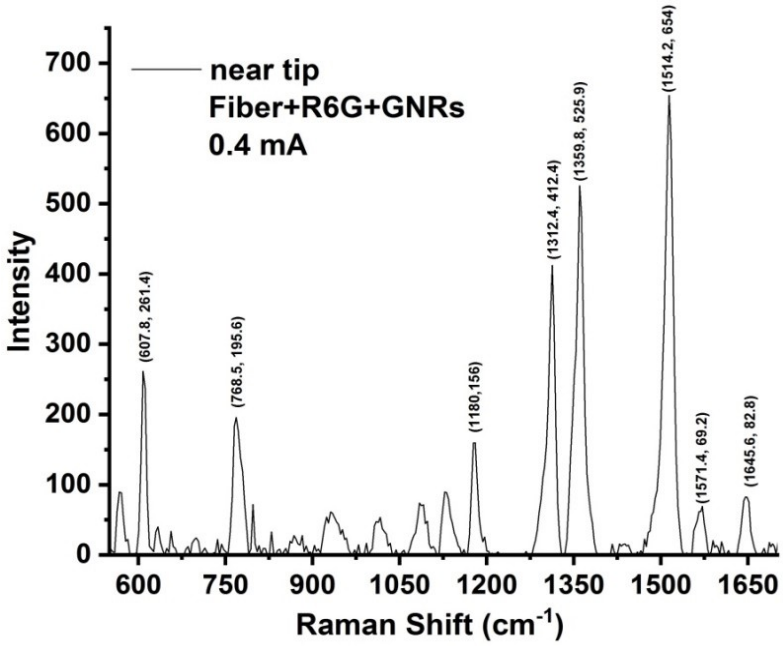


(b)

**Figure 2.8:** Comparing the Raman spectrum near tip region: (a) Fiber+R6G, (b) Fiber+GNRs+R6G.

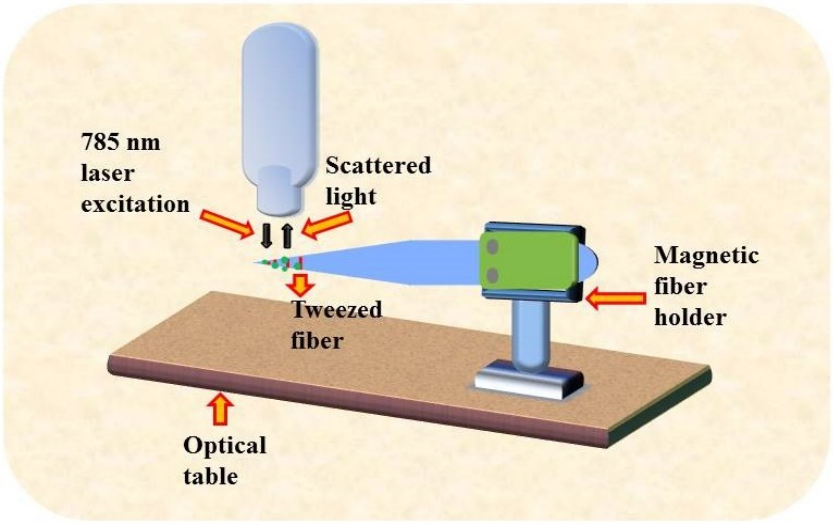


**Figure 2.9:** Schematic of the experimental set-up.

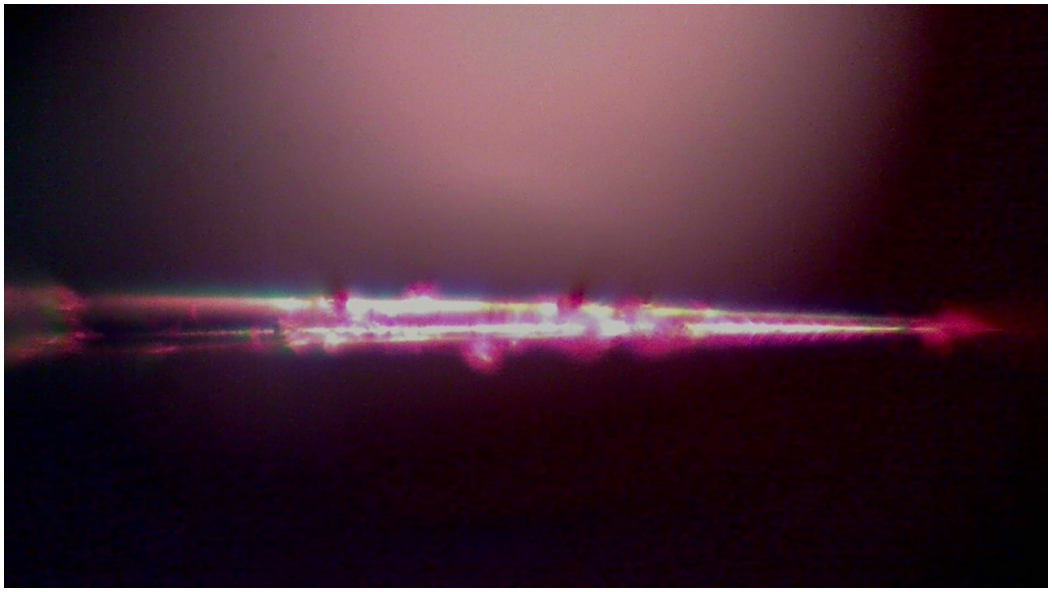

**Figure 2.10:** Optical image of a tweezed tapered fiber with sprinkled R6G along the length (taken by a camera).

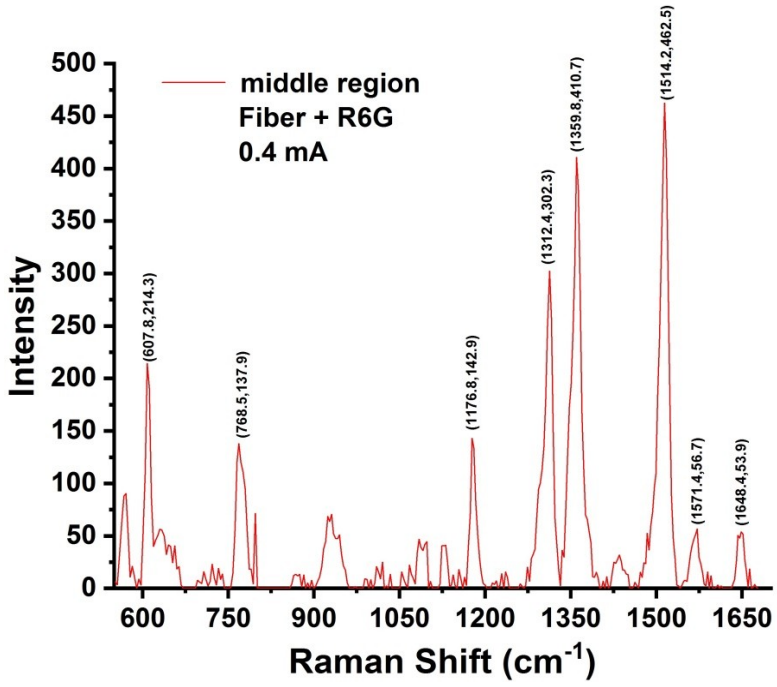


(a)

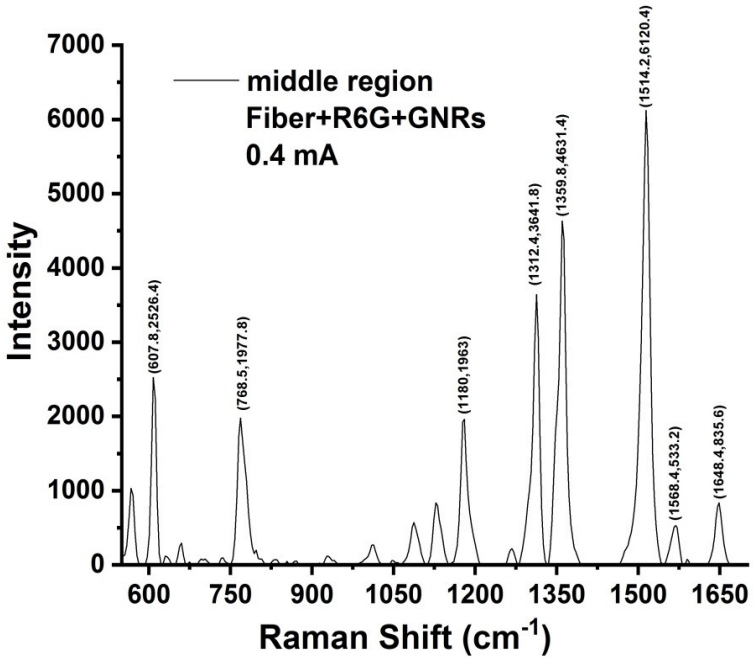


(b)

**Figure 2.11:** Comparing the Raman spectrum in the middle region: (a) Fiber+R6G, (b) Fiber+GNRs+R6G.

The excitation laser wavelength was 785 nm at 10.5 mW (current = 0.4 mA). In Figures 2.7, 2.8, and 2.11, the integration time was 1000 ms, average scans were 5, and the total exposure time was 5 seconds. All the experimental conditions were kept the same for comparison.

To test the functionality of the substrate, a metal compound, Zinc Oxide (ZnO), was tested by sprinkling on the tapered fiber probe to obtain its Raman spectrum. A pile of ZnO was placed on a coverslip to obtain the expected Raman spectrum (Figure 2.12). For this measurement, the same excitation laser wavelength of 785 nm with ∽100 mW power (current = 0.6 mA) laser excitation was used. The integration time was 1000 ms,

and the number of scans averaged was 5. When this bulk mass was present, a high-intensity count was obtained for the ZnO.

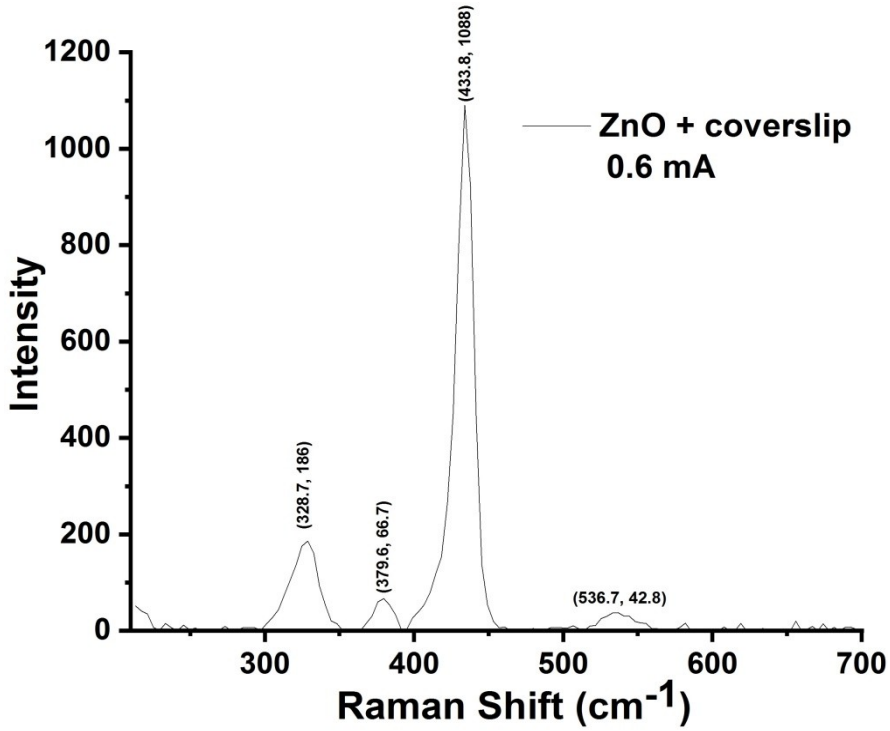


**Figure 2.12:** Raman spectrum excited by 785 nm of ZnO.

Similar to R6G, the ZnO Raman spectra were obtained near the tip and the middle region of the tapered fiber covered with GNRs (Figure 2.13 (a) and (b)). The sprinkling method was used to adsorb ZnO onto the fiber probe. The Raman spectrum was obtained by averaging five scans and 5000 ms integration time, which gives 25 seconds of total exposure time. A 785 nm laser excitation laser wavelength with ∽168 mW power (current = 0.7 mA). A higher power was required to obtain the spectra for ZnO compared to R6G. Although the intensity count is high near the tip region, the peak at 437.7 $cm^{-1}$ is more distinguished in the middle region because of the denser GNR distribution. It is

noticeable that the amount of analyte present on the fiber is negligible compared to that on the coverslip.

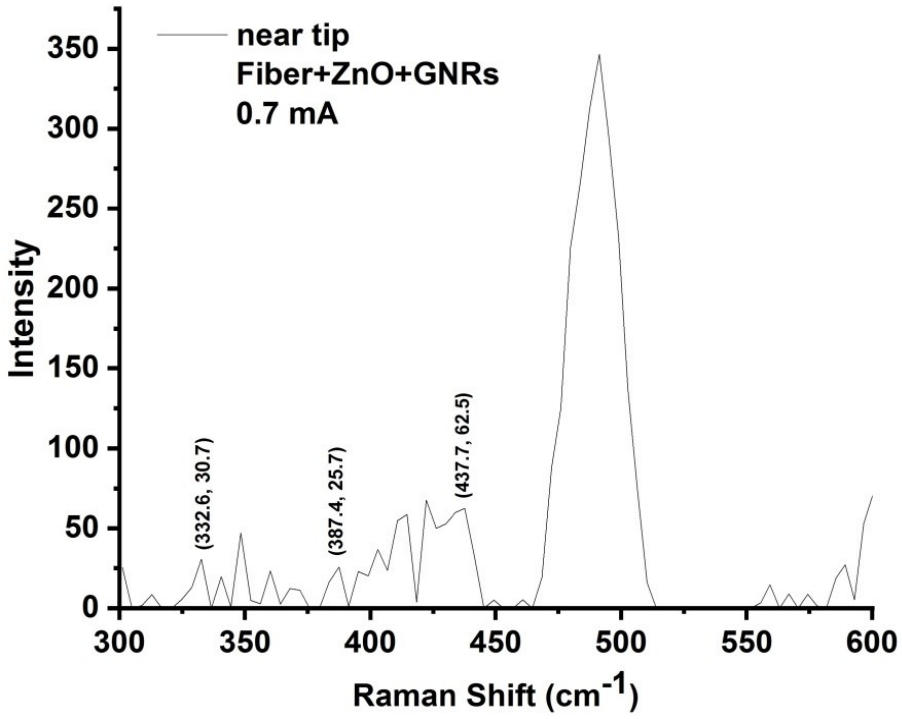


(a)

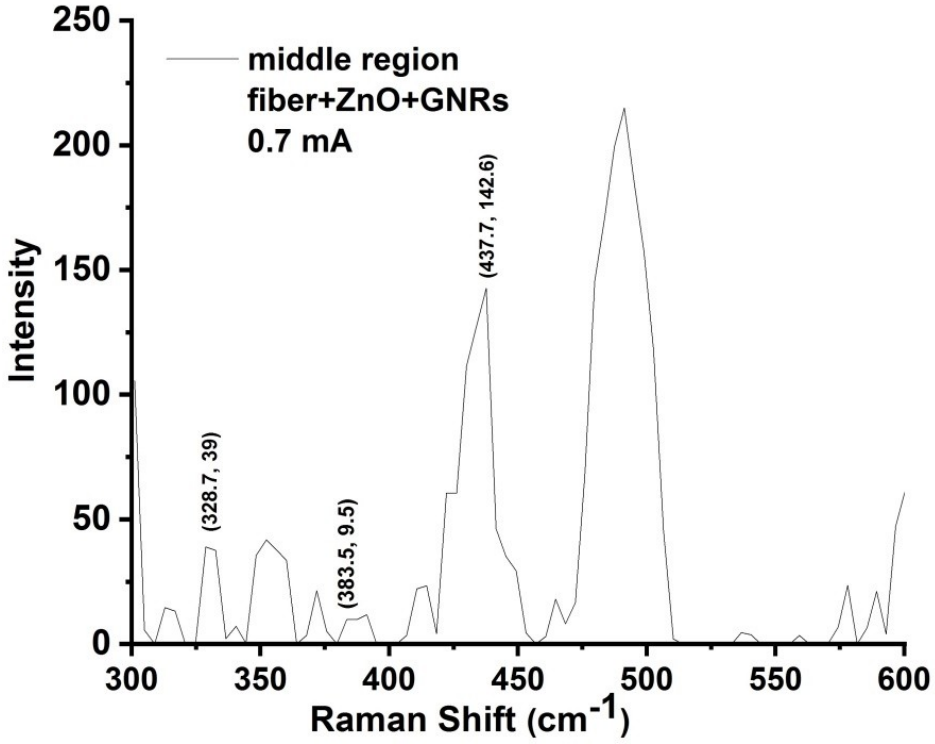


(b)

**Figure 2.13:** Comparing Raman spectra of ZnO powder: (a) near the tip region and (b) in the middle region.

### 2.6.2 Dip and dry method

Sprinkling was an unreliable method as the analyte's exact concentration is inconsistent. Therefore, it is essential to introduce an acceptable method where an exact concentration of the analyte on the fiber surface can be known to determine the detection limit, which will further decide the sensitivity of the fabricated substrate. A dip and dry method was presented where an exact concentration of R6G was mixed in nanopore water, and the tapered fiber covered with GNR rings was dipped in ∽ 65 µl drop of analyte solution for

adsorption along the fiber length. The schematic of the set-up used for dip and dry is shown in Figure 2.14. Raman spectra were obtained and studied once the drop dried. It took ∽ 1.5 hours for the drop to dry completely. Two fiber samples were prepared to observe the enhancement from GNRs. The first was bare tapered fiber with R6G on it, and the second sample was with tapered fiber with a GNRs distribution covered with R6G. Figure 2.15 compares with and without GNRs near the tip region for R6G at $10^{-3}$ M concentration. The integration time was 7000 ms, and five scan average. The laser power used in both cases was 65.8 mW (0.5 mA). The R6G peaks were more distinguishable when GNRs were present on the fiber. This strongly indicates that the developed fiber probe can be used as an excellent SERS substrate.

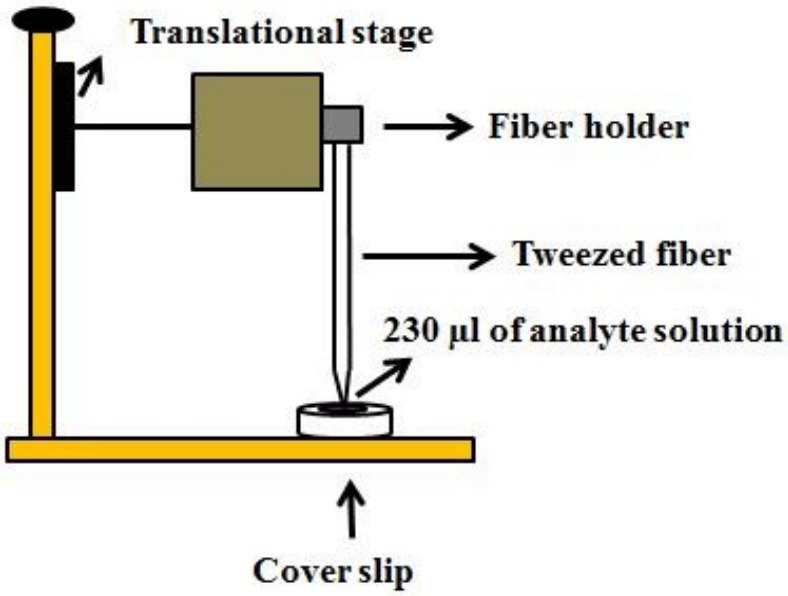


**Figure 2.14:** Schematic of the dip and dry method.

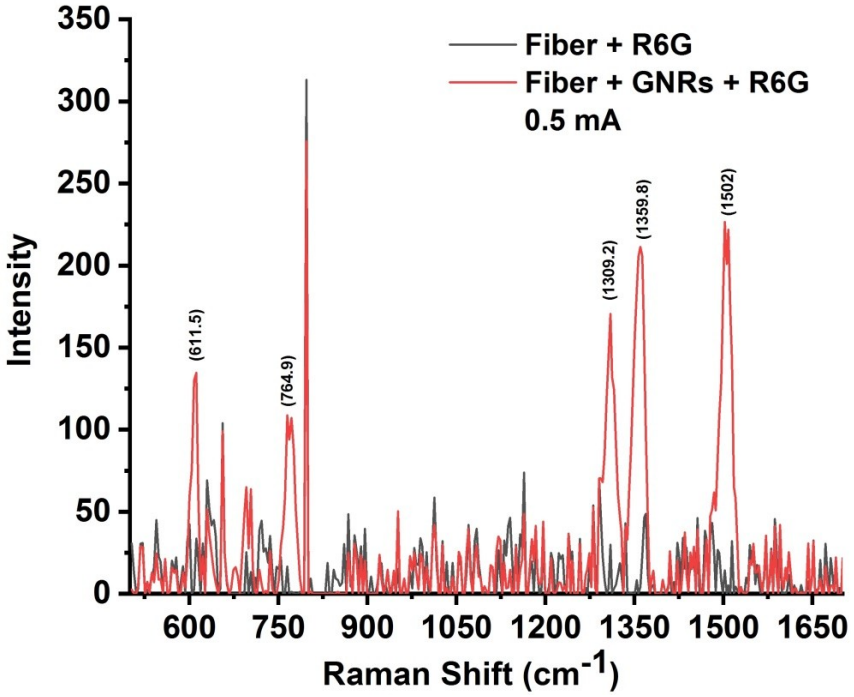


**Figure 2.15:** Raman spectra of R6G comparing with and without GNRs for R6G at $10^{-3}$ M concentration.

After verifying the significant enhancement due to the presence of the GNRs experimentally, six samples with concentrations $10^{-3}$, $10^{-4}$, $10^{-5}$, $10^{-6}$, $10^{-7}$, and $10^{-8}$ M of R6G were prepared to determine the detection limit. A few Raman peaks for R6G at $10^{-7}$ M were visible. Therefore, the $10^{-7}$ M detection limit for R6G in our first article was reported as shown in Figure 2.16 [88].

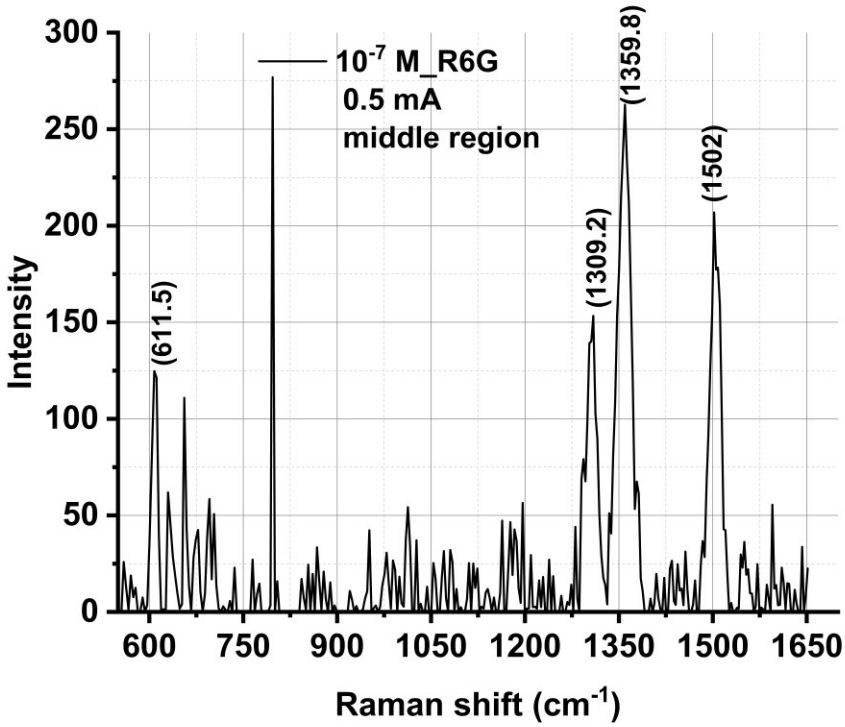


**Figure 2.16**: Raman spectrum of R6G at $10^{-7}$ M concentration in middle region (integration time: 7000 ms and average scans: 5).

Now that the process of substrate manufacturing and analyte adsorption has been outlined, the next question is: what other methods or improvements in the existing dip and dry method can be made to increase the sensitivity of the substrate? First, the drop-casting method was tried. Figure 2.17 (a) shows the schematic of the drop-casting process. As illustrated, the tweezed fiber was kept on a coverslip, and a drop of R6G was cast onto the fiber. The fiber was held stable on the coverslip using scotch tape. The primary issue encountered was that the surface area of fiber near the tip and middle region is too small, and the drop has the natural tendency to spread over the coverslip. A classic coffee ring pattern was observed when the solvent (water) evaporated completely,

which means there is a solvent flow with the analyte particles from the center towards the edge [92]. Figure 2.17 (b) shows the three stages from the time when the droplet was just placed, after a few minutes of evaporation, and once it is completely dried. Therefore, the chances are very low that the analyte will stay on a substrate with such small dimensions. The other disadvantage of this method is that the laser will not only be focused on the fiber but also on the coverslip, which will give the Raman peaks from both the analyte and coverslip. The above-mentioned reasons make this method non-viable.

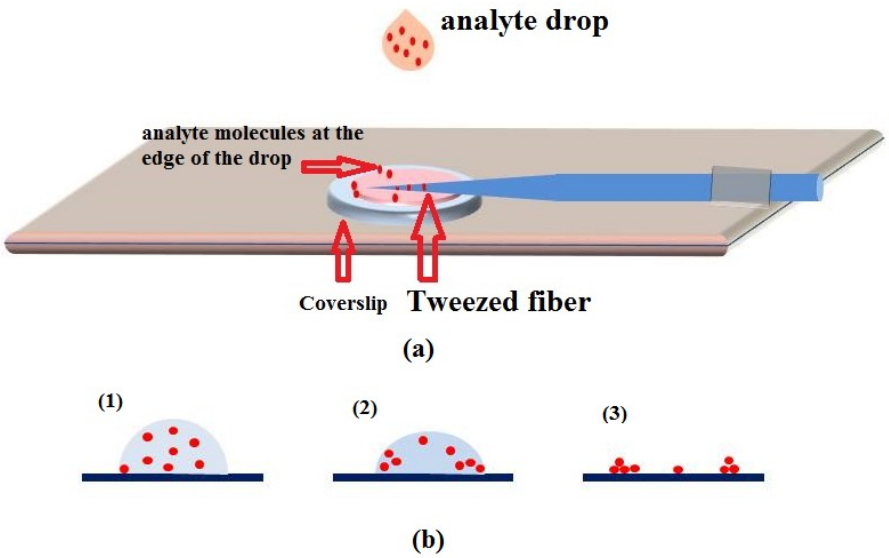


**Figure 2.17:** (a) Schematic showing the drop-casting method, and (b) diagram showing the evaporation stage of the drop (1) drop just cast, (2) after a few minutes of evaporation, and (3) after complete evaporation.

At this stage it is determined that the performance of the SERS substrate depends on (A) fabrication and design of the substrate, (B) adsorption of the analyte and (C) data collection from the fiber probe. We identified a few challenges, one of which was

obstructing the enhanced sensitivity of the substrate. The rest of the chapter describes the challenges and how we resolved them.

## 2.5 Revised dimensions of the tapered fiber

The first challenge was the size of the tapered fiber's tip. Until this point, nanometer-sized tips were used in all the experiments. The tip diameter of the fiber probe was optimized to make it more robust, as the nanometer-sized tip is easily breakable. The tip diameter was changed from ~ 100 nm to ~ 35 μm. Figure 2.18 is the SEM image showing the modified probe. The probe's tip diameter change did not alter its properties as far as GNRs distribution is concerned. It was achieved by changing the withdrawal speed of the fiber from HF acid. The speed was increased from 0.00084 mm/s to 0.0016 mm/s, and the diameter of the tapered fiber decreased uniformly from 125 μm to ∽ 35 μm. The time to etch the fiber was reduced from one and a half hours to approximately 30 minutes. Another important observation was made that the GNRs were intact in shape at the tip (Figure 2.19). Therefore, no modifications were needed in the tweezing conditions, i.e., the same laser power and technique were used.

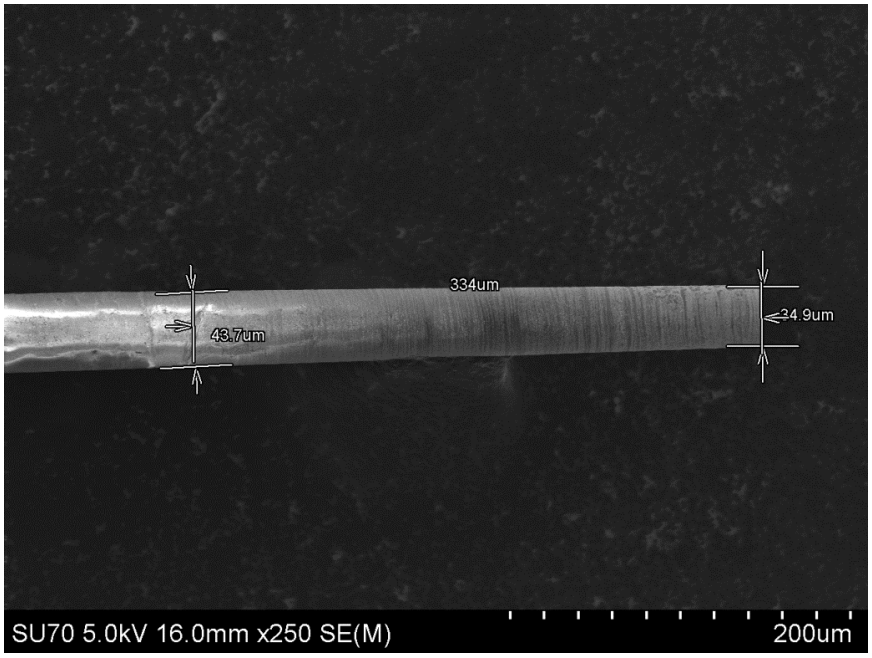


**Figure 2.18:** SEM image showing tip diameter of the probe approx. 35 um with GNRs ring-like structure along the tapered length.

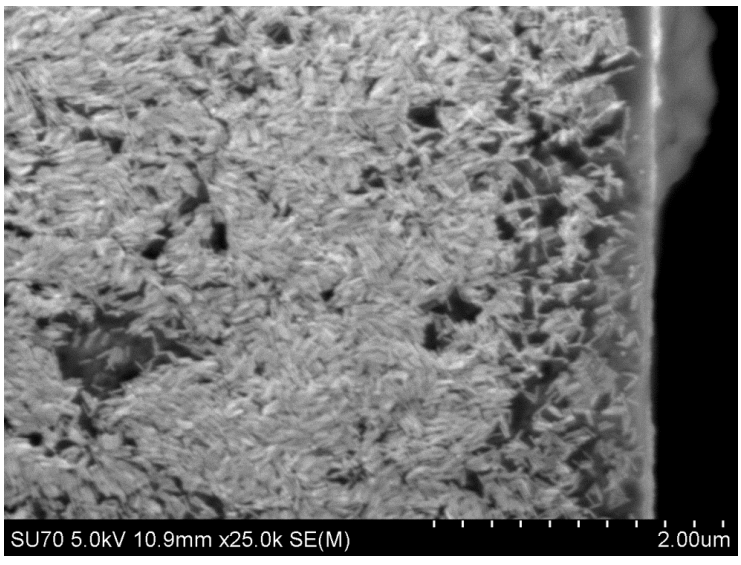


**Figure 2.19:** SEM image showing the intact shape of GNRs at the tip.

## 2.6 Modifications in the experimental set-up

As discussed earlier, sprinkling and drop casting were not efficient methods to determine the sensitivity in terms of adsorption of the analyte on the substrate. However, the dip and dry method detected a $10^{-7}$ M concentration for R6G. However, it was believed that there was still room for improvement in the experimental methodology as significant sensitivity was not achieved. First, it was observed that the height of the GNRs solution drop should match the height of the analyte solution drop to ensure that the height of the tapered fiber dipped in both solutions remains the same. Therefore, for tweezing and adsorption, a 230 µl drop size was used with the drop height (h), similar in each case. Figure 2.20 (a) and (b) describe the above-mentioned process. The same set-up was used for both experiments. The analyte molecules must be distributed uniformly around the diameter of the tapered fiber along the length of the tweezed tapered portion, forming a three-dimensional tapered fiber-based SERS substrate.

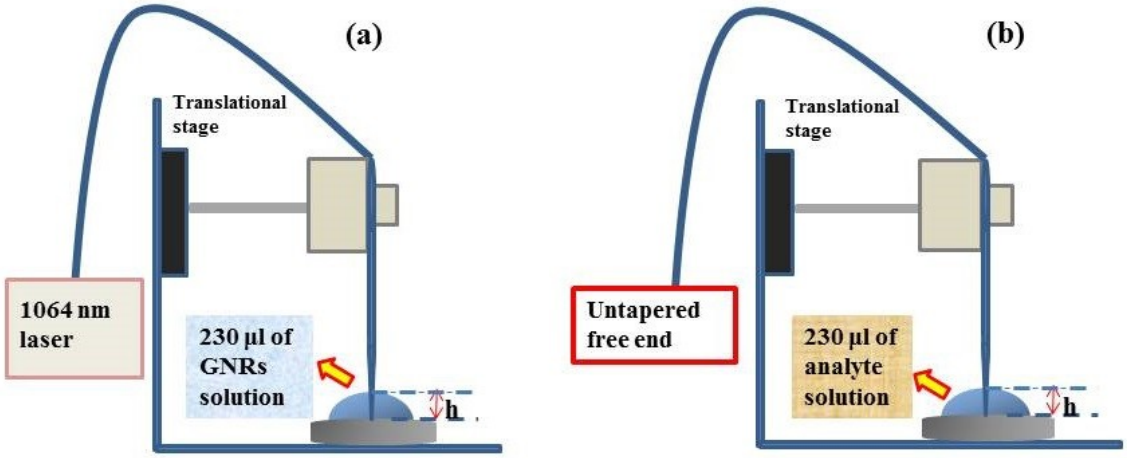


**Figure 2.20:** Schematic showing the experimental set-up of (a) tweezing process and (b) dip and dry process, where height, h of drop size is identical in both cases.

To develop a 3D substrate, it was important to build a precise mechanical system to ensure the 360-degree rotation of the tapered fiber probe on its axis under the laser beam. The idea was to see whether the analyte distribution is uniform at a particular diameter, which can be obtained from the intensity count. Numerous attempts were made to develop a homemade fiber mount that can be rotated around its axis. Initially, the Raman spectroscopic data of crystal violet (CV) analyte with various concentrations was obtained near the tip and middle region of the tweezed fiber. Figure 2.21 (a) and (b) shows the intensity variation for the Raman spectrum collected for $10^{-7}$ M concentration of CV. The Raman spectroscopy data was collected at 9 angular positions (0º, 45º, 90º, 135º, 180º, 225º, 270º, 315º, and 360º) at a specific diameter. The intensity variation represents the non-uniformity of the analyte. However, it was due to the set-up used in

the experiment. Further, we are collecting data at one particular location from the tip where GNRs distribution is approximately uniform.

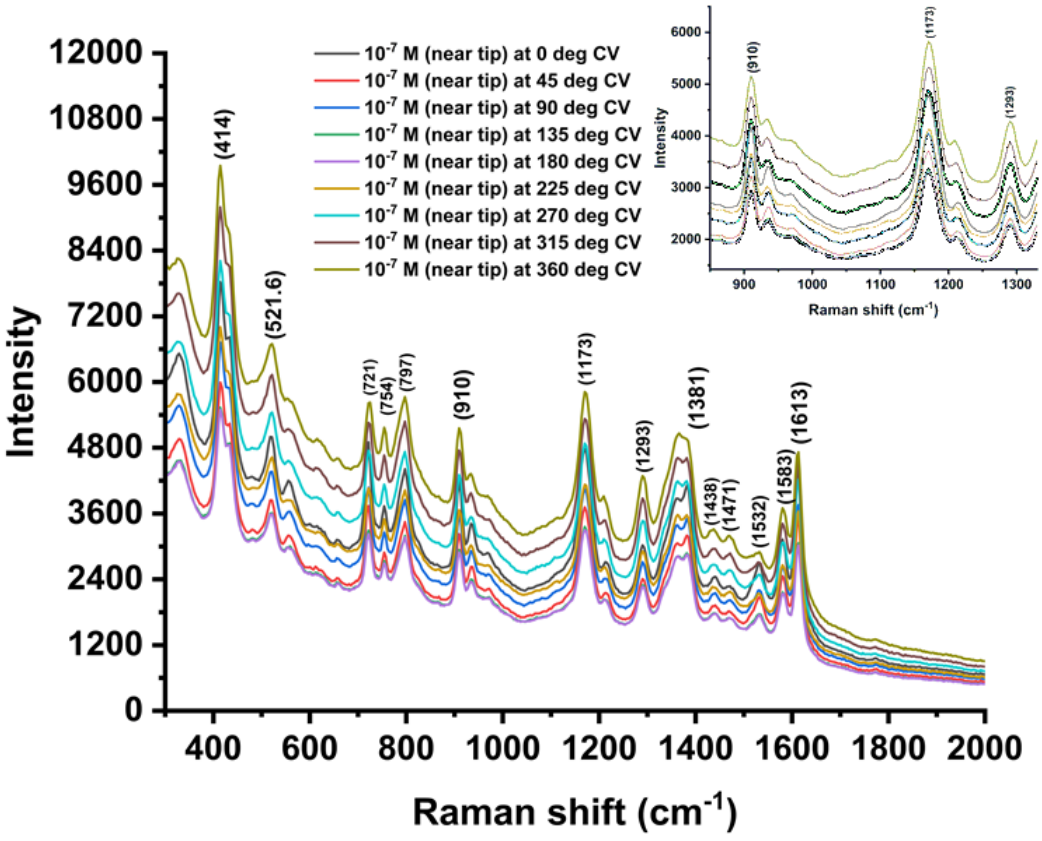


(a)

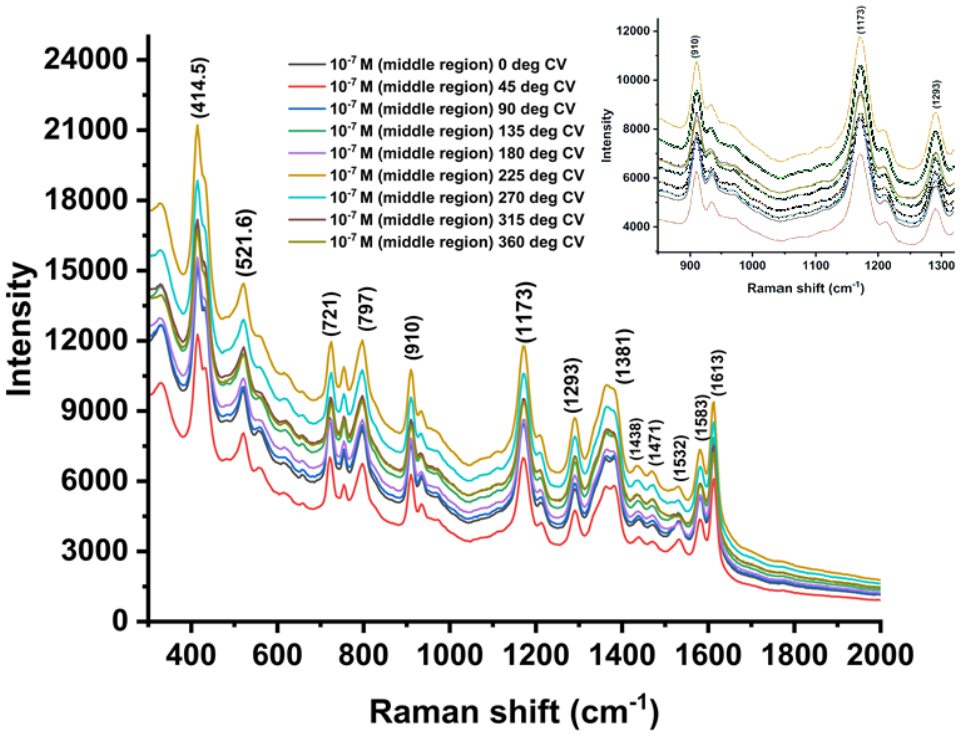


(b)

**Figure 2.21:** Raman spectra show the intensity variation at nine different angular positions at the specific diameter of (a) the tip region and (b) the middle region of the tapered fiber probe. The inset shows the enlarged view of three peaks.

One source of error observed during experiments was that the tapered fiber was not held straight under the laser beam, which means not all the scattered light was not collected by the collection optics fitted with the system; one contributing factor to this could be that the chuck (it is a component used to hold the fiber straight and can be safely integrated into the optical set-ups) was tightened more than required, which resulted in bending of the tapered fiber. Additionally, near the tip and middle region, there is a broad range to work with; therefore, an accurate micrometer is required to monitor the back-and-forth movement of the tapered fiber probe as it is aligned under the laser. Thus, to

overcome the shortcomings of the set-up, a small length of tapered fiber was allowed to hang out of the fiber chuck, which was closed gently to avoid the extra pressure on the probe, and a differential micrometer was introduced in the set-up, which can accurately control the fiber movement back-and-forth and was mounted on a three-axis stage. Figure 2.22 shows the schematic of the fabricated fiber mount to collect the Raman spectra [93].

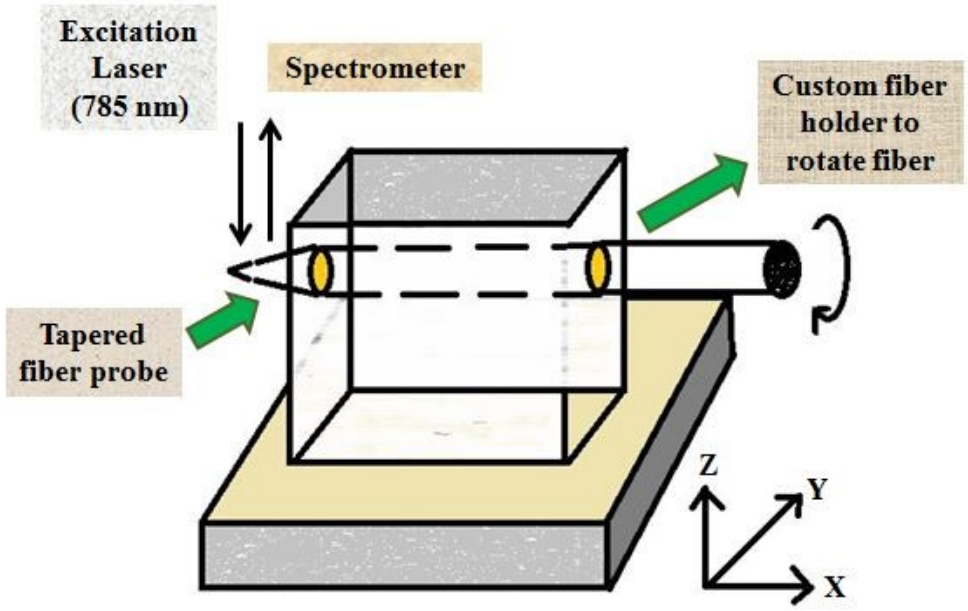


**Figure 2.22:** Schematic showing the details of the experimental set-up to collect Raman spectra from the tapered fiber probe.

The Raman spectra were collected using the improved set-up version at 12 locations (or diameters) along the tapered fiber probe. At each location, five angular positions (0º, 90º, 180º, 270º, and 360º) were explored to observe the uniformity of the analyte. The tip of the fiber was considered as a reference point, and the first location was

considered 30 µm away from the tip (named locn_1), and each location tested was 30 µm apart from the other. Figure 2.23 shows the 12 locations and distance from the fiber tip.

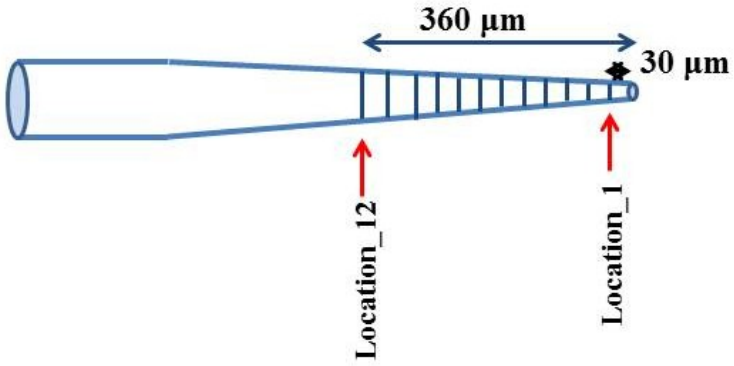


**Figure 2.23:** Schematic of the tapered fiber showing 12 locations and their distance from the tip.

After making the above-described changes, an aqueous stock solution of R6G (Sigma-Aldrich, dye content 99%) and CV (Sigma-Aldrich, analytical standard) was prepared with a concentration of $10^{-5}$ M as shown in Figure 2.24 (a) and (b).

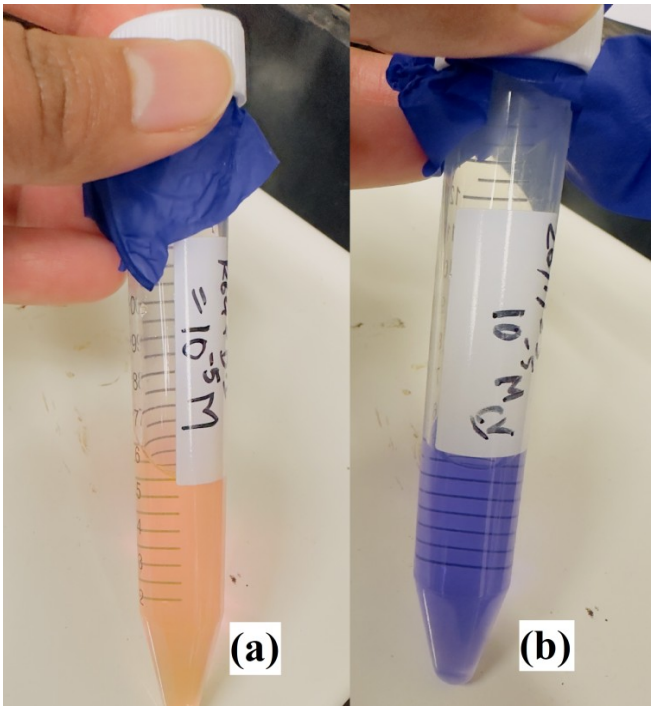


**Figure 2.24:** Stock solution of $10^{-5}$ M concentration of (a) R6G and (b) CV for Raman analysis.

Diluting the stock solution, a range of solutions from $10^{-7}$ M to $10^{-13}$ M were prepared to determine the detection limit of the two chemicals, which will further represent the sensitivity of the tapered fiber probe. A fiber was first etched and tweezed using GNRs with AR of 3.8 (length = 19 nm, diameter = 5 nm) from Nanopartz (NPz), USA. The reason behind choosing these GNRs is to match the 785 nm excitation wavelength with the LSPR wavelength of the GNRs. It will enhance the interactions with GNRs because the GNRs absorb the incident laser radiation more effectively. For each Raman spectrum, we averaged 5 scans, the integration time was 2000 ms, and the spectrum was saved after three scans, resulting in a total exposure time of 30 seconds. The excitation laser has a power of 10.8 mW. Figure 2.25 (a) shows the Raman spectrum obtained for $10^{-9}$ M conc. of CV at a particular location on the tapered fiber, which is

situated 30 μm (named locn_1) from the fiber tip and at five angular positions. Figure 2.25 (b) is the bar graph showing the uniformity in the SERS intensity at different angular positions (0º to 360º) at locn_1. The results verified the uniform distribution of both GNRs and analyte molecules. The other 11 locations were explored on the same substrate by moving the fiber back and forth, and consistent results were observed. In statistical terms, the relative standard deviation (RSD) values of Raman intensities for a particular peak were calculated at all 12 locations to determine the uniformity of the substrate along with the analyte distribution. RSD was calculated using below [94]:

$$RSD = \sqrt{\frac{\sum_{i=1}^{n}(I_i - I_{avr.})^2}{(n-1)}}\ \frac{1}{I_{avr.}} \qquad (1)$$

where n is the size of the sample data set in the present case, it is the number of collected Raman spectra, $I_i$ represents the Raman intensity of each characteristic peak, $I_{avr.}$ is the average intensity of the Raman signal. The RSD values calculated for CV with concentration $10^{-9}$ M at 1170 $cm^{-1}$ characteristic peak were 1.86%, 2.7%, 1.96%, 0.68%, 1.15%, 0.99%, 2.21%, 1.42%, 3.08%, 2.92%, 3.7%, and 5.5%, respectively, from location 1 (30 μm from tip) to location 12 (360 μm from tip) representing a good uniformity of the fabricated plasmonic substrate across the entire area [94]. Therefore, dip and dry proved to be an outstanding method for analyte adsorption, establishing the homogeneous distribution of the analyte molecules at a specific location. This unique feature of the developed tapered fiber as a 3D probe allows the substrate to be placed at a particular location with any angular position.

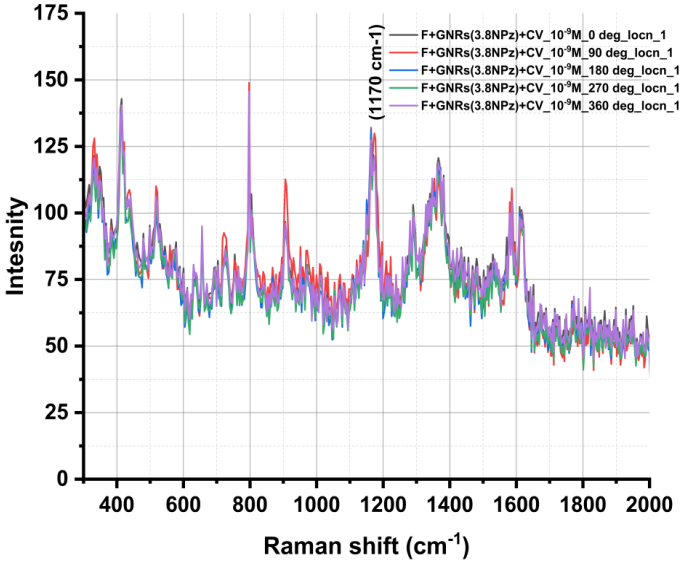


(a)

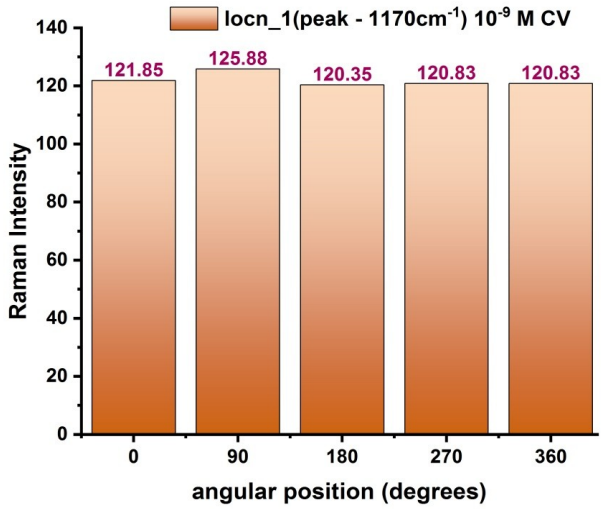


(b)

**Figure 2.25:** (a) Raman spectra and (b) bar graph representing the uniformity of the SERS intensity at five different angular positions for location 1 for a concentration $10^{-9}$ M of CV at 1170 $cm^{-1}$ characteristic peak [93].

Another important observation was made from the same experiment, which determines the practical location where SERS intensity is high compared to other locations on the substrate. At location 7, 210 μm away from the tip, the SERS intensity reaches its maximum magnitude, as revealed in Figure 2.26 for CV ($10^{-9}$ M, 1170 $cm^{-1}$). The fiber diameter at this location is ∽ 36.4 μm, and a denser GNRs distribution was present compared to the other areas of the fiber, as shown in Figure 2.27. Therefore, based on the probe's design, one can focus the excitation laser at this location for optimum SERS collection. These results were verified by repeating the experiments for both R6G and CV at all 12 locations and five angular positions (0º to 360º) from $10^{-7}$ M to $10^{-13}$ M concentrations.

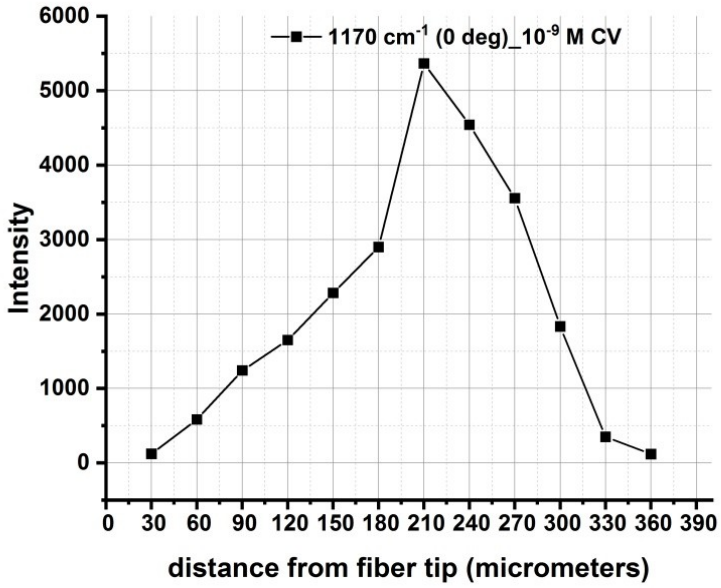


**Figure 2.26:** The trend representing the maximum SERS intensity at location 7, which is 210 μm away from the tip [93].

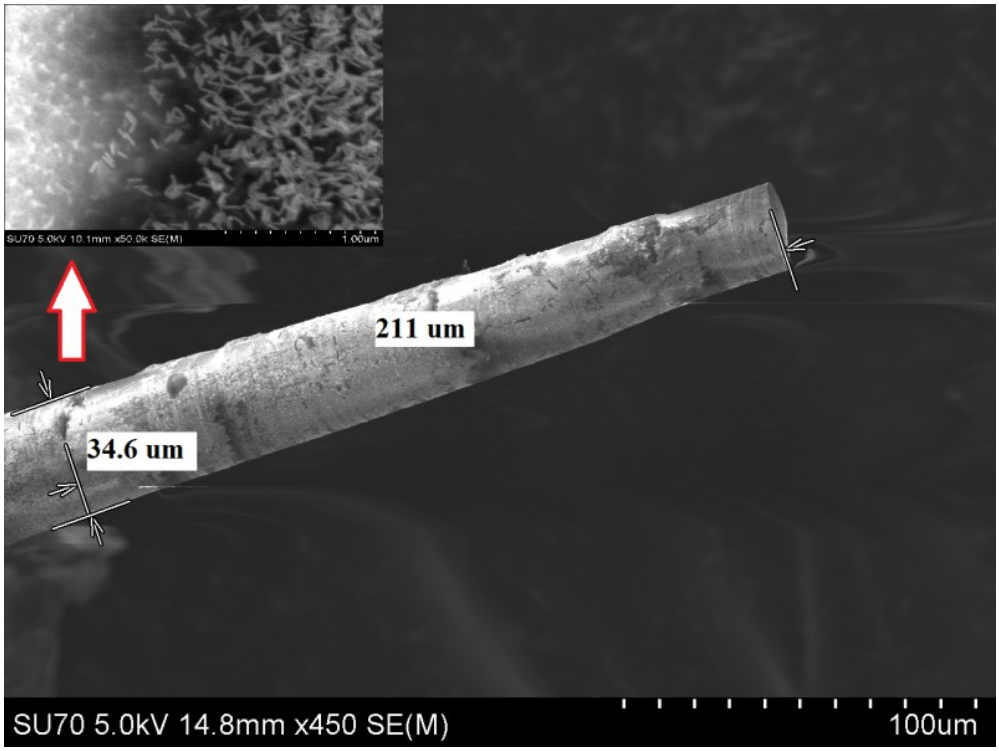


**Figure 2.27:** SEM image showing the fiber diameter (34.6 μm) where maximum SERS intensity was obtained. The inset shows the distribution of GNRs at that location [93].

Figure 2.28 (a) and (b) illustrate the chemical structure of R6G and CV, respectively. Figure 2.29 (a) and (b) show the SERS spectra of R6G and CV at different concentrations. Using the tapered fiber probe, the trace detection of R6G and CV was achieved successfully, and the detection limit (LoD) was determined to be $10^{-12}$ M in both cases. The SERS signal indicates a decrease in intensity with decreasing concentration. The detection sensitivity of the developed SERS substrate was understood from the characteristic peaks of each chemical (R6G: 772 $cm^{-1}$ and 1502 $cm^{-1}$ and CV: 414.5 $cm^{-1}$, 728.8 $cm^{-1}$, and 1170 $cm^{-1}$), which were then compared from $10^{-8}$ M to $10^{-13}$ M for R6G and $10^{-7}$ M to $10^{-12}$ M for CV, respectively. These peaks were distinguishable

until the $10^{-12}$ M concentration in both cases, which is displayed graphically. The obtained characteristic peaks for both R6G and CV match the data reported in the literature [6,95].

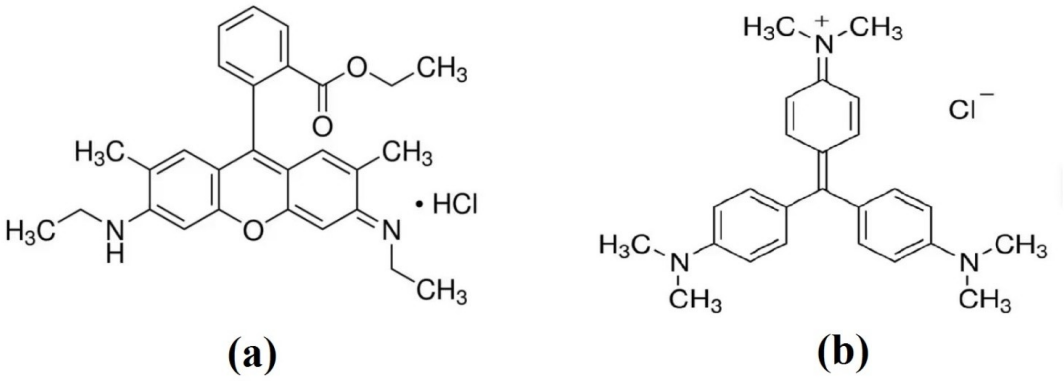


**Figure 2.28:** Chemical structures of (a) R6G (Sigma Aldrich) and (b) CV (Sigma Aldrich).

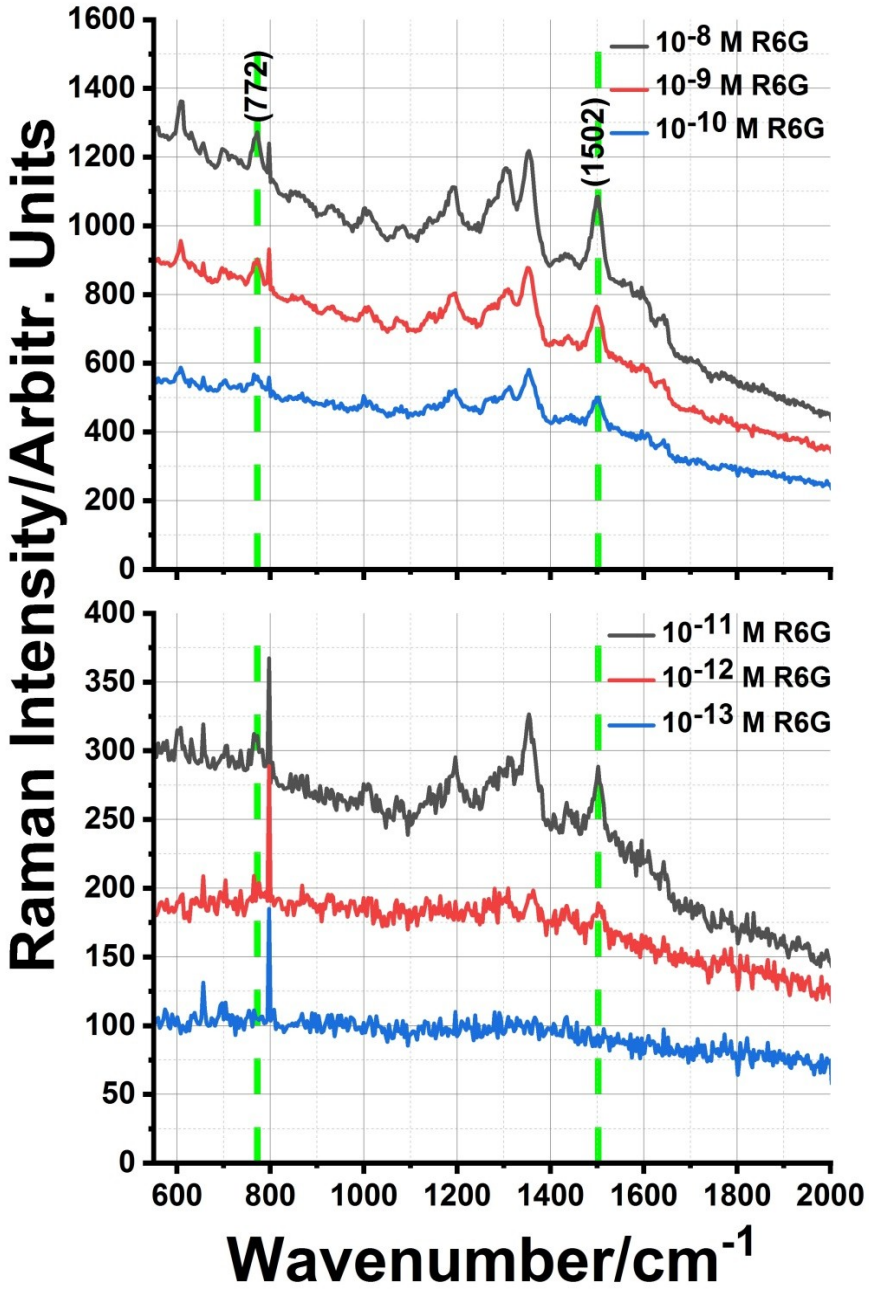
Raman Intensity/Arbitr. Units
Wavenumber/cm-1
(772)
(1502)
10-8 M R6G
10-9 M R6G
10-10 M R6G
10-11 M R6G
10-12 M R6G
10-13 M R6G
0
200
400
600
800
1000
1200
1400
1600
0
50
100
150
200
250
300
350
400
600
800
1000
1200
1400
1600
1800
2000

(a)

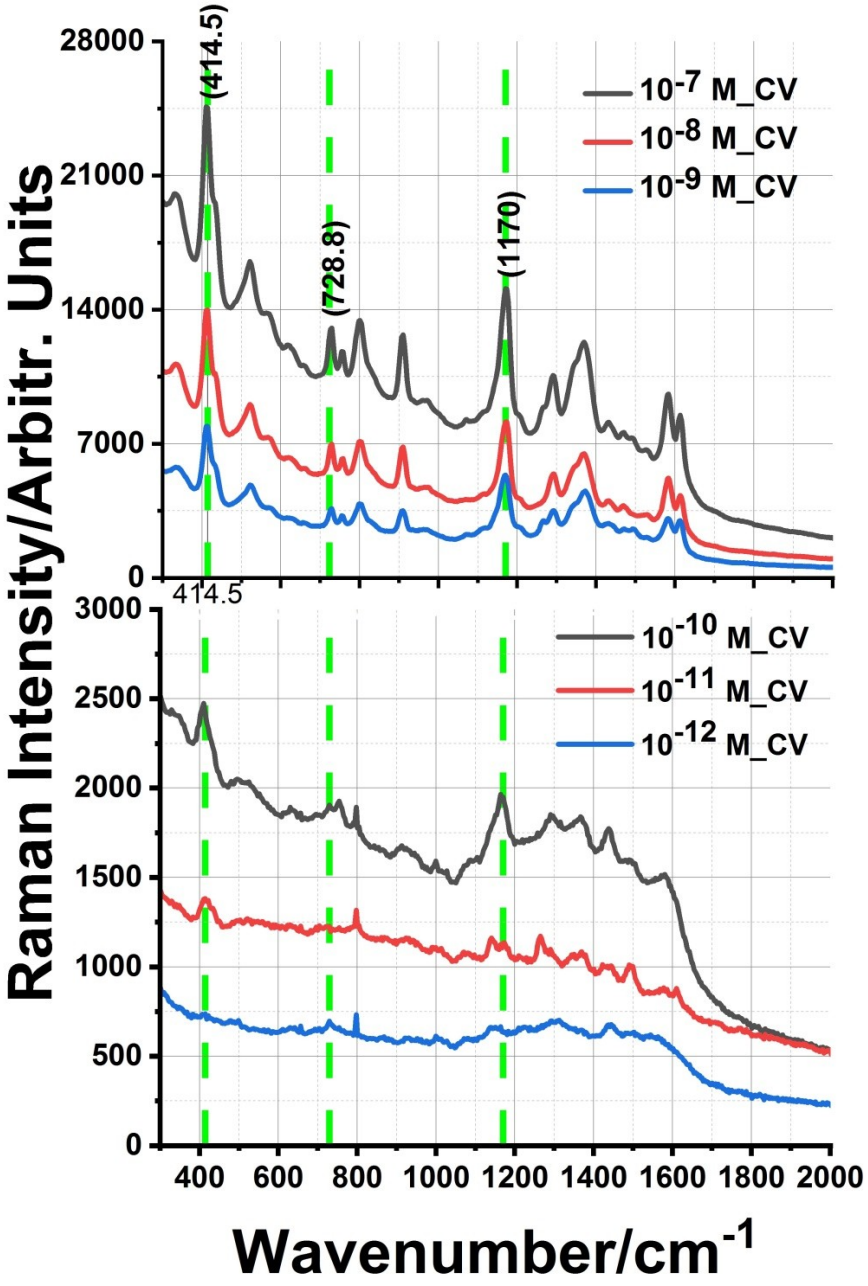


(b)

**Figure 2.29:** SERS spectra comparing different concentrations of (a) R6G ($10^{-8}$ M to $10^{-13}$ M) and (b) CV (Sigma Aldrich) [93].

The experiments were repeated after a few days with the same probe to test the stability of the tapered fiber probe. The obtained results were similar, showing the same characteristic peaks, which shows the substrate's stability. It is to be noted that the prepared probe is intended for one-time use only. Another important feature of the SERS substrate is reproducibility, which was tested by repeating the SERS experiment multiple times with the same chemical and concentration. Again, consistent results were obtained.

## 2.7 Conclusion

In conclusion, the fabrication of a plasmonic structure and its application was demonstrated here for the first time using gold nanorods along the tapered optical fiber length. A simple technique known as optical tweezing was used to obtain the plasmonic structure. With modifications in the adsorption method of the analyte and the set-up of SERS data collection, it was successfully established that the developed plasmonic structure can be used as a three-dimensional SERS substrate for the trace detection of chemicals. It showed a superior detection sensitivity of $10^{-12}$ M for R6G and CV, making the probe a potential candidate for environmental monitoring and food safety. This method has excellent research significance in agriculture, such as detecting chemicals in hops plants, which have applications in the brewery industry, and harmful herbicides used in fields for weed removal, adversely affecting humans and soil nutrients. Further investigation was done to see the advantage of the manufactured 3D substrate in real-time by developing an adequate experimental set-up for the detection of trace chemicals discussed in **Chapter 6.**

# Chapter 3

## Plasmonic structure of zinc (Zn) and zinc oxide (ZnO) on a tapered optical fiber

***This chapter*** *introduces optical tweezing to deposit Zinc (Zn) and Zinc Oxide (ZnO) along with gold nanorods on a tapered fiber surface. The manufactured structure will find applications as a SERS substrate. Also, the effect of tweezing conditions on the distribution of the Zn and ZnO distribution on the plasmonic structure was investigated.*

### 3.1 Introduction

The interest in using SERS in clinical practice is a current research topic due to its advantages, such as simple design, non-invasive, fast detection, reliability, affordability, etc. Recently, research based on semiconductor biosensors, particularly Zinc Oxide (ZnO) based SERS substrates, has gained interest in biosensing because of their excellent biocompatibility, non-toxicity, and economic nature [96]. The unique optical, electronic, and chemical properties of ZnO-based nanomaterials have attracted worldwide attention in biomedical and industrial applications [97-101]. The distinctive features of nanoscale

ZnO materials, such as their biocompatibility, biodegradability, and low toxicity, make them a good candidate for the treatment of various types of cancer, such as breast cancer, colon cancer, lung cancer, ovarian cancer, and cervical cancer. ZnO also exhibits luminescent properties, making it well-suited for bioimaging [97]. Also, the lasing in ZnO thin films at room temperature was demonstrated, which were grown on (0001) sapphire substrates using plasma-enhanced molecular beam epitaxy. By cleaving the films, laser cavities were formed, which exhibited lasing behavior when optically pumped at a threshold excitation intensity of 240 kW/cm$^2$ and thus showed the potential of ZnO-based materials for light-emitting devices [98]. Various ZnO nanomaterials such as nanorods, nanowires, nano-micro flowers, quantum dots, thin films, and nanosheets have been used to fabricate an efficient gas sensor to detect harmful gases such as $NO_2$ [100]. There are several techniques, such as in situ chemical etching, hydrothermal treatment, chemical reaction of zinc with water in 50-200°C temperature range, sol-gel methods, and microwave-assisted a chemical bath deposition method that have been used to develop different morphologies of ZnO nanostructures [102-107]. It was observed that one-dimensional ZnO nanostructures, such as nanorods, exhibit excellent chemical and thermal stability. Temperature has a detrimental effect on the morphology of ZnO nanostructures during the growing process as it can affect the sensitivity [103,108,109].

ZnO-based SERS substrates have been developed by different groups [110-112] and confirmed that they have enough potential for early clinical diagnosis of diseases from biological fluids such as blood, urine, and lymph. For the early diagnosis of refractory diseases (which do not respond to treatment), such as interstitial cystitis/bladder pain syndrome (IC/BPS), a ZnO-based SERS substrate was prepared, and the sample was

collected from rats' urine. Raman analysis distinguished between the standard and diseased/infected samples [111]. Also, neurodegenerative diseases (ND) such as Parkinson's disease (PD) and Alzheimer's disease (AD) can be detected in real-time using ZnO-based SERS substrates from saliva and blood serum samples, respectively [112]. One group reported that maximum enhancement was obtained when ZnO was coated with Au, and $10^{-8}$ M detection was achieved for CV [113]. Another group reported $10^{-9}$ M as the detection limit for R6G, where ZnO nanorods were grown on the glass substrate in the preferred (002) direction and coated with AuNPs [110]. Recently, a detection limit of $10^{-13}$ M for CV was achieved using a ZnO-based SERS substrate. Various techniques have been proposed and reported for the fabrication of semiconductor-based SERS substrates, such as the wet chemistry method [113], pulsed-laser-induced photolysis (PLIP) [110], a combination of pulsed laser deposition (PLD) and ion implantation technique [114], a combination of hydrothermal synthesis and magnetron sputtering method [115].

In literature, several techniques have been proposed and demonstrated to deposit ZnO nanostructures on an optical fiber surface, for example, the sol-gel method [116,117], an atomic layer deposition (ALD) method [118], and a dip coating method [119]. The major drawback of the above-mentioned techniques is that the deposition of ZnO and metallic nanostructures is done in two steps, which are complicated and time-consuming.

We proposed and demonstrated a new, simple, and efficient method to deposit Zn or ZnO together with GNRs on the tapered fiber surface via optical tweezing and its application as SERS substrate [120].

## 3.2 Methodology

In this technique, a mixture of ZnO and GNRs with a concentration of 0.5 µg/µl (300 µg of ZnO powder was mixed in 600 µl of GNRs) was used to develop the SERS substrate. GNRs with AR of 6.7 (Nanopartz, USA, A12-10-1064-CTAB-DIH-1, OD at 1064 nm > 1.0) was used to develop the substrate. Before tweezing, we prepared a ZnO solution with water and determined the structure of the ZnO using SEM. A drop of the prepared solution was placed on carbon tape, which was adhered to SEM sample holder and allowed to dry completely (∽ 2 hours) before characterization. Figure 3.1 (a) is the SEM image of the ZnO nanostructures along with GNRs, and the size of ZnO nanorods (Chemistry Store, Lakehead University) was ∽400 nm in length (Figure 3.1 (b)). Generally, the hexagonal Wurtzite crystal structure is the most stable in ZnO. Also, ZnO-NRs preferably grow along the c-axis (0001), which is the favorable growth direction [100].

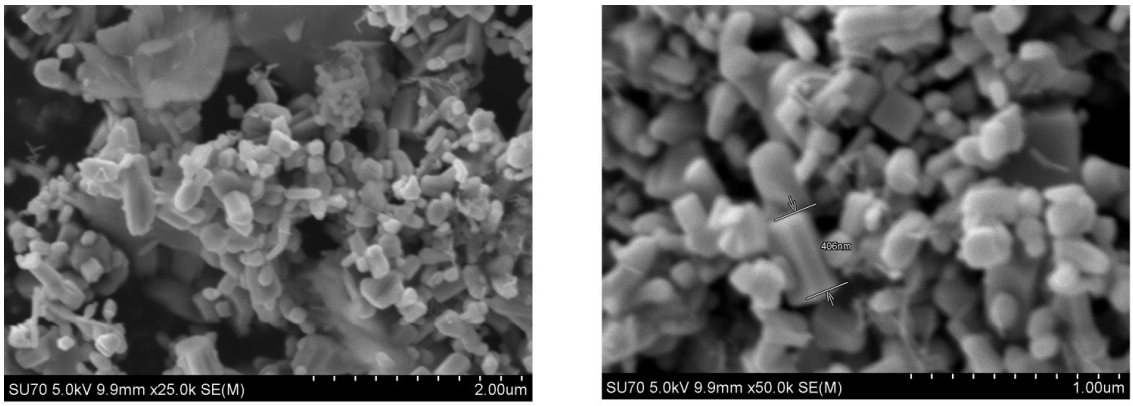


**(a)** **(b)**

**Figure 3.1:** SEM image of GNRs and ZnO nanostructure on a carbon tape, (a) ZnO (10's of nm in length and Hexagonal in shape) with GNRs (Length: 67 nm, diameter: 10 nm, AR: 6.7), and (b) magnified image showing the ZnO-NR.

Figure 3.2 summarizes the manufacturing process of the plasmonic structure, which was used as the SERS substrate: (1) shows the etching process of MMF, (2) represents the ZnO and GNRs solution preparation, (3) shows the tweezing process, where light from 1064 nm laser is coupled at the untapered end of the optical fiber. Also, we used a 632 nm laser for tweezing, and finally, characterization of the plasmonic structure using SEM, TEM, and an optical image using a standard optical microscope [121].

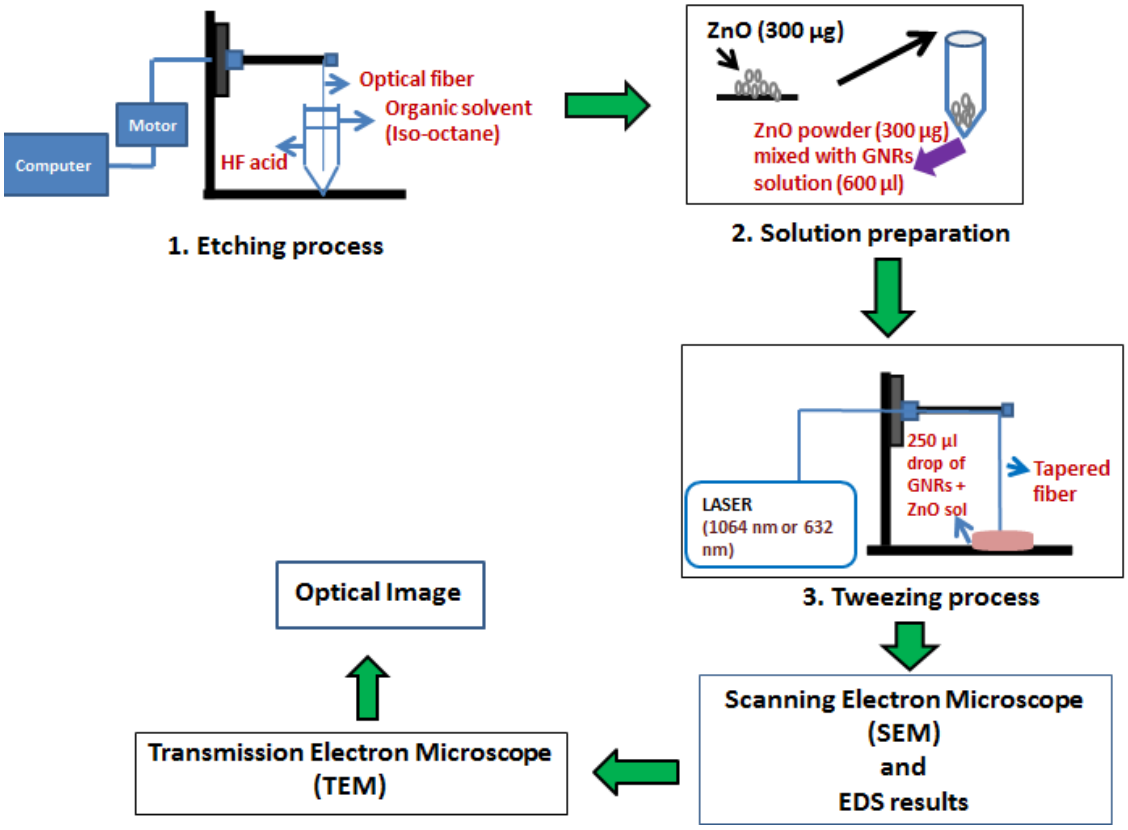


**Figure 3.2:** Schematic showing the manufacturing process of the ZnO-NRs and GNRs-based SERS substrate.

## 3.3 Effect of tweezing conditions on the distribution of Zn, ZnO, and GNRs

A double tweezing technique (tapered fiber was tweezed with two different laser wavelengths, 1064 nm with 8.5 mW and 632 nm, with 10 mW, consecutively) was used to determine the effect of the ZnO and GNRs distribution along the tapered length of the fiber. We obtained a ring-like plasmonic structure consisting of combined GNRs and

ZnO nanostructures along the fiber length (Figure 3.3). The average width and separation of the ring were ∽ 5.0 μm (Figure 3.4 (a)) and ∽ 7.5 μm (Figure 3.4 (b)), respectively.

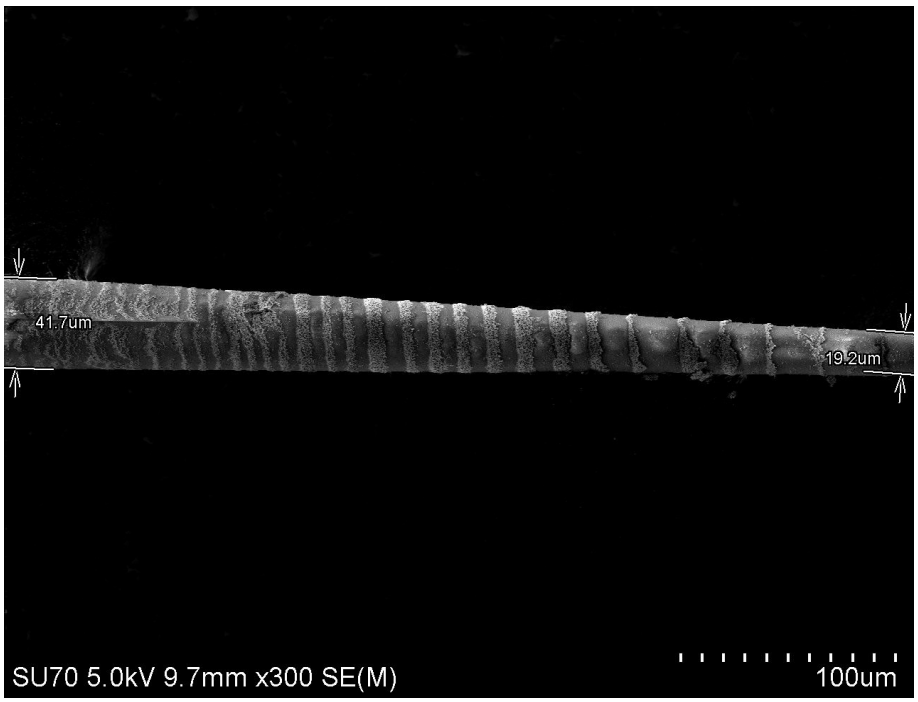


**Figure 3.3:** SEM image showing the distribution of GNRs and ZnO nanostructures along the tapered fiber length on middle and end regions of the tapered fiber using double tweezing.

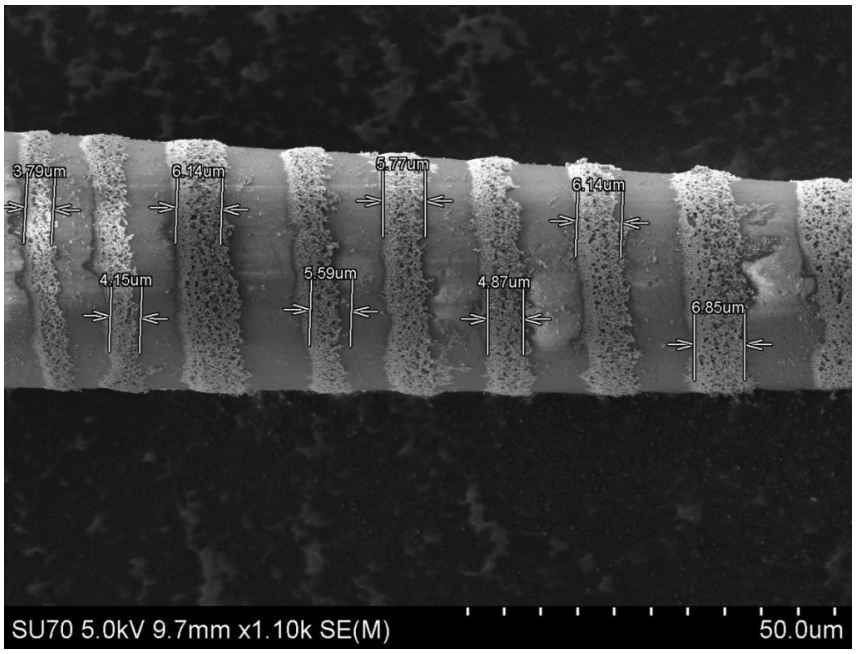


(a)

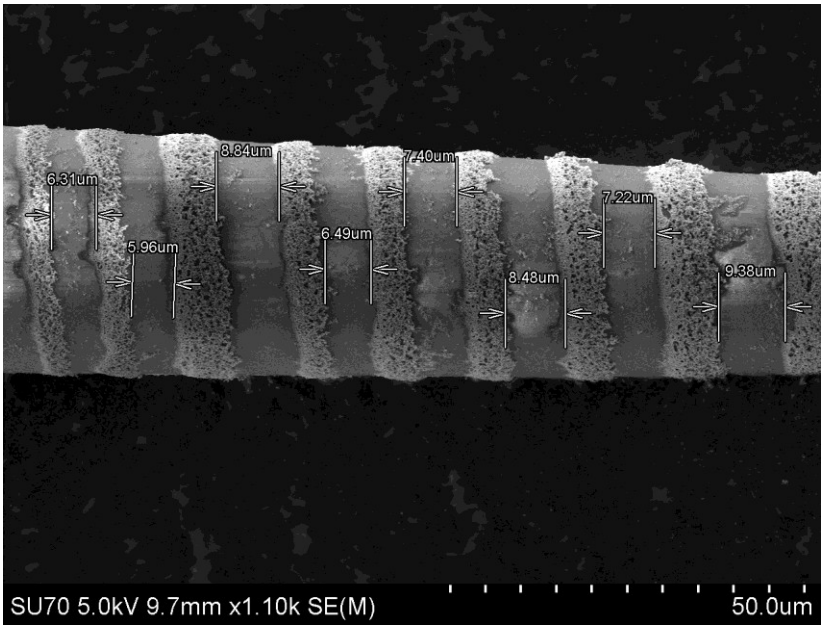


(b)

**Figure 3.4:** SEM image showing the (a) width of the rings and (b) separation between the rings along the tapered fiber length obtained using double tweezing.

Figure 3.5 is the zoomed image of one of the rings from Figure 3.3. On comparing the images from Figure 3.1 with Figure 3.5, it can be concluded that the shape of the ZnO nanostructures and GNRs was intact before and after tweezing. The experiments were performed with various concentrations of ZnO, but the ring structure did not form when the concentration was high (e.g., 1.0 μg/μl) because the gradient force becomes insufficient to overcome the scattering force beyond a specific concentration [121].

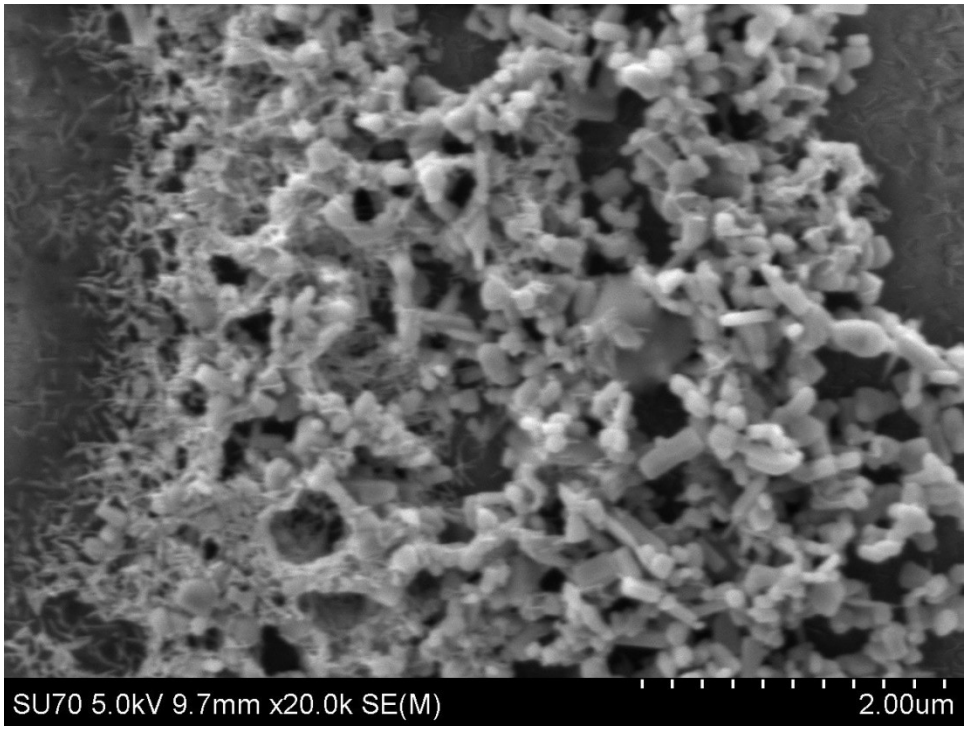


**Figure 3.5:** An enlarged image of the ring is used to show the ZnO nanostructure and GNRs.

The following experiment was performed to develop the plasmonic structure using single tweezing (As described in **Chapter 2** when GNRs were tweezed) and

keeping the rest of the conditions the same as before. Figure 3.6 illustrates the formation of the ring structure when single tweezing was used (1064 nm). The average width of the ring was ∽ 9.0 μm, and separation between rings was ∽ 7.22 μm. There is a variation in the width and separation of rings compared to the double tweezing due to the number of modes supported by the fiber at different diameters along the tapered fiber at 632 nm laser wavelength compared to 1064 nm. Another critical factor is the coupling efficiency of the laser at the untapered end, which can change the amount of gradient and scattering forces. The optical image of the fiber using double tweezing was obtained using a camera [120]. To obtain the picture of the rings, a He-Ne laser (632 nm) was coupled at the untapered end of the fiber, as shown in Figure 3.7.

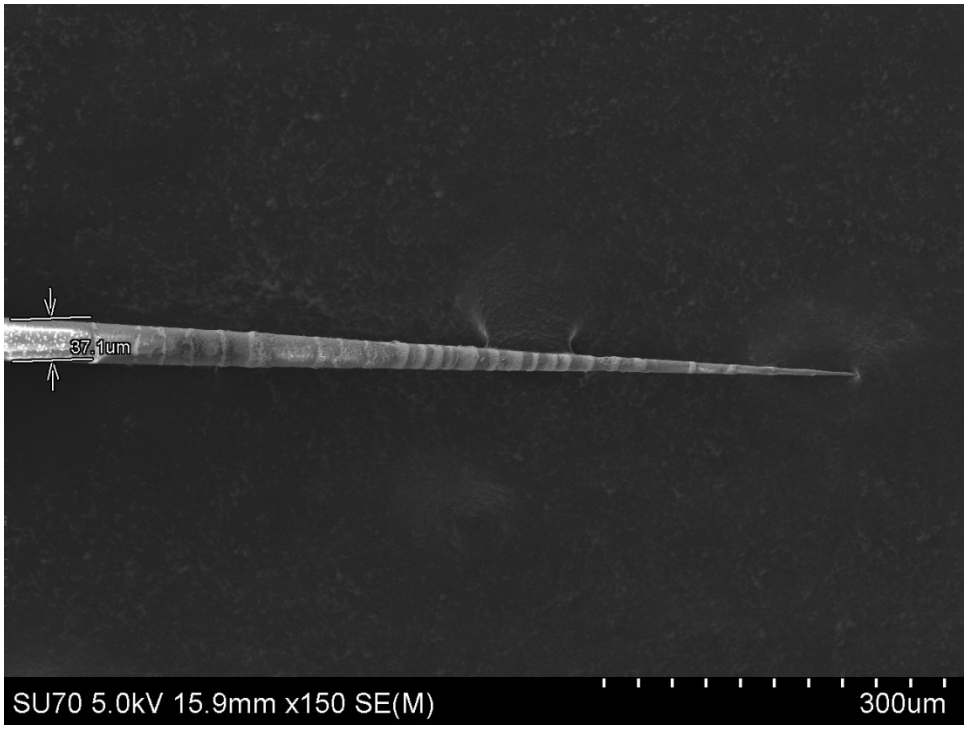


**Figure 3.6**: SEM image showing the ring-like structure along the fiber length obtained using single tweezing (1064 nm).

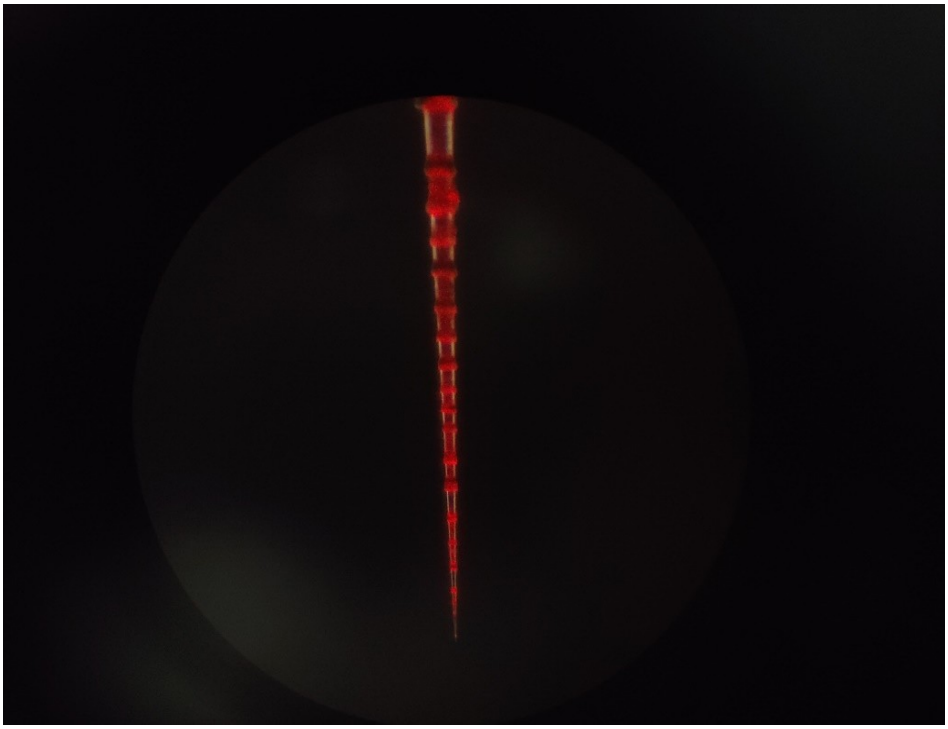

**Figure 3.7:** Optical image showing the ring structure along the tapered fiber after double tweezing.

To study the effect of laser on the distribution of ZnO and GNRs on the tapered fiber, we dipped the tapered fiber in the ZnO and GNRs solution for 2 hours, and no laser was coupled at the untapered end of the fiber. After scanning the dried tapered fiber under SEM, patches of ZnO nanostructures + GNRs were observed, but no rings were present (Figure 3.8 (a)). Figure 3.8 (b) shows an enlarged image of one of the patches showing their distribution. Figure 3.8 (c) shows the energy dispersive spectroscopy (EDS), which confirmed the presence of Zn and O. Further, ZnO's surface charge can be negative or positive in an aqueous solution, depending on the pH of the solution. The

measured value for the pH of the solution was 7.0, which makes the ZnO surface positively charged [122]. Therefore, it can be concluded that tweezing is essential to achieve a consistent ring-like plasmonic nanostructure with ZnO along the fiber length. We also characterized ZnO using UV-visible spectrometry. Figure 3.9 shows a peak at 379 nm, which occurs due to the electronic transition from valance to conduction band [123]. ZnO nanostructure powder was also characterized using X-ray diffraction (XRD). Figure 3.10 is the X-ray diffraction (XRD) pattern of the ZnO obtained using Cu Kα-radiation with a wavelength of 1.5 Å. The values of the diffraction angles, 2Θ ( 2 theta) 31.77º, 34.39º, 36.23º, 47.52º, 56.58º, 62.83º, 66.38º, 67.92º, and 69.06º corresponds to the (100), (002), (101), (102), (110), (103), (200), (112), (201), (004), (202) diffraction planes, respectively, which indicates the hexagonal nanostructure of the ZnO. This data is similar to the reported data in the literature [124].

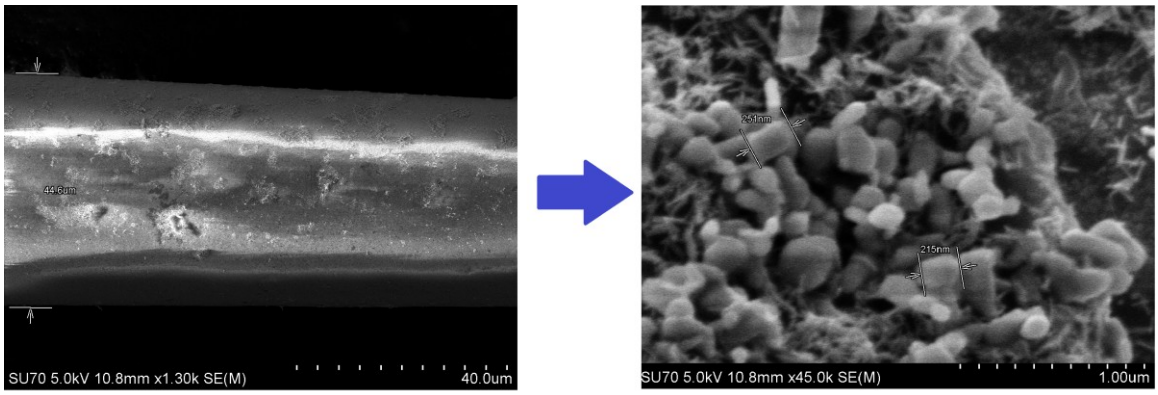


(a) (b)

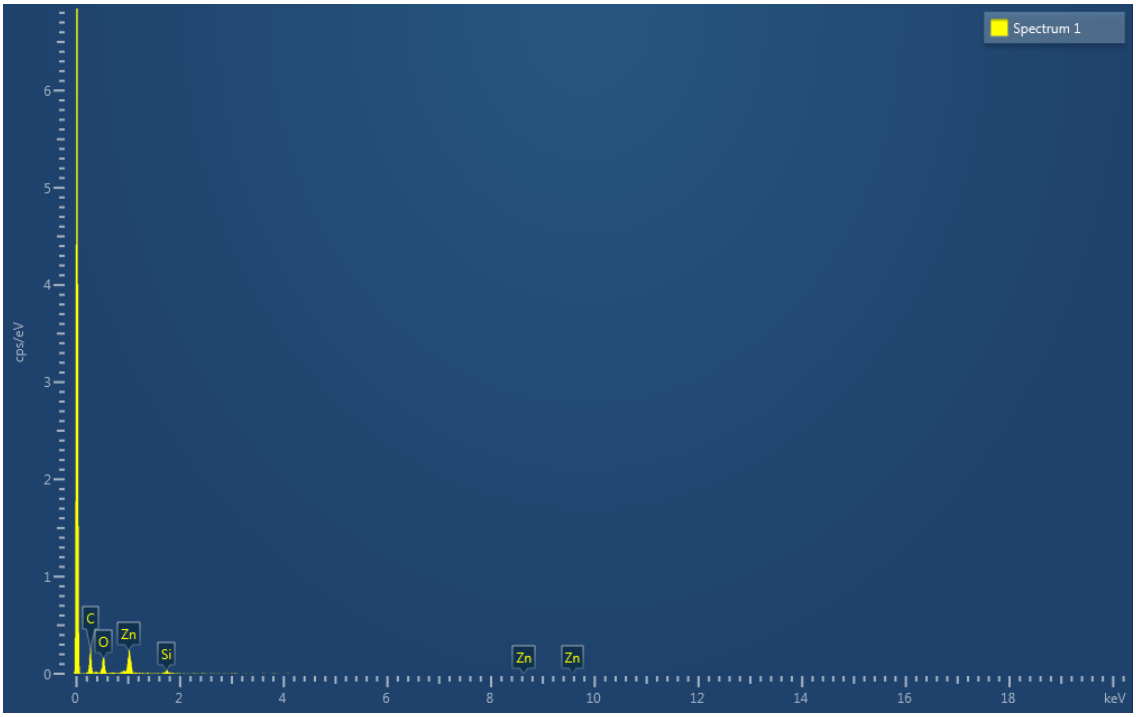


(c)

**Figure 3.8:** (a) SEM image showing the patches of ZnO+GNRs along the fiber length, (b) magnified image of the patch to show ZnO and GNRs distribution, and (c) EDS results confirming the presence of Zn and O.

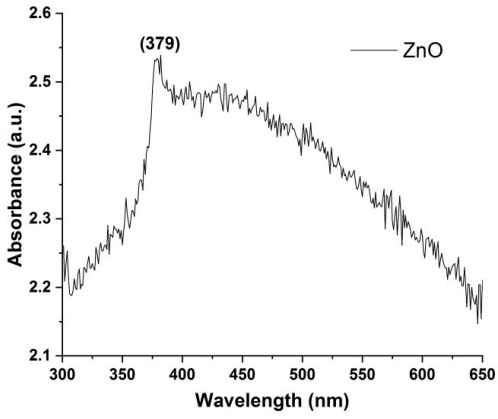


**Figure 3.9:** UV-visible spectrum of ZnO.

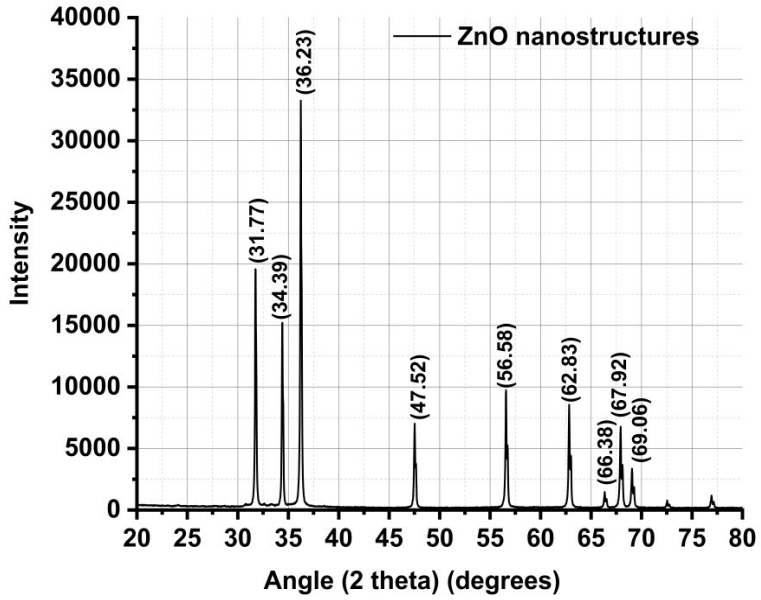


**Figure 3.10:** XRD spectrum of ZnO nanostructure.

The same experiment was repeated as above but without GNRs. In this experiment, ZnO was mixed in a CTAB solution and prepared a solution of ZnO with a concentration of 0.5 µg/µl. A random distribution of ZnO was observed on the fiber surface (no rings), which was confirmed through SEM. It has been reported that the morphology of the ZnO nanostructures depends on the amount of CTAB present at a specific temperature [108]. The higher concentration of CTAB increases the degree of crystallinity of ZnO nanoparticles, which results in larger-sized ZnO nanoparticles [125]. An experiment was performed to compare the effect of CTAB on ZnO nanostructures using UV-visible spectrometry. Two samples were prepared: (1) ZnO mixed in CTAB + D.I. (de-ionized water), and (2) ZnO mixed only in D.I. water. Figure 3.11 shows that the intensity of the peak at 379 nm increases in the presence of CTAB, and the peak is more

distinguished. Therefore, these results confirm the higher crystallinity of the ZnO-NRs in the CTAB solution.

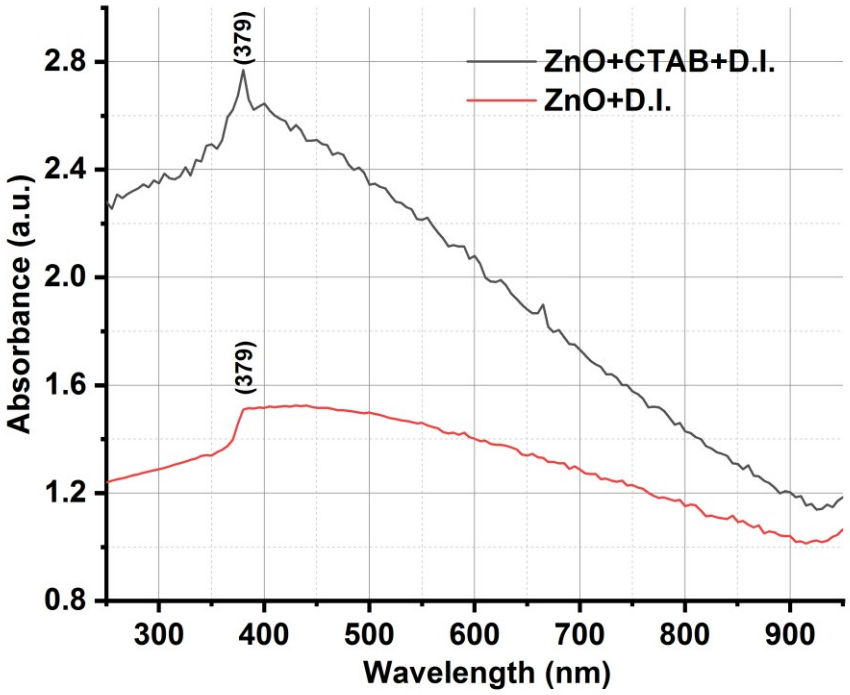


**Figure 3.11:** Comparing absorption spectra of ZnO with or without CTAB.

The ZnO powder used for the experiments contained non-uniform-sized ZnO nanostructures. Figure 3.12 shows the transmission electron microscope (TEM) image of the ZnO used for tweezing.

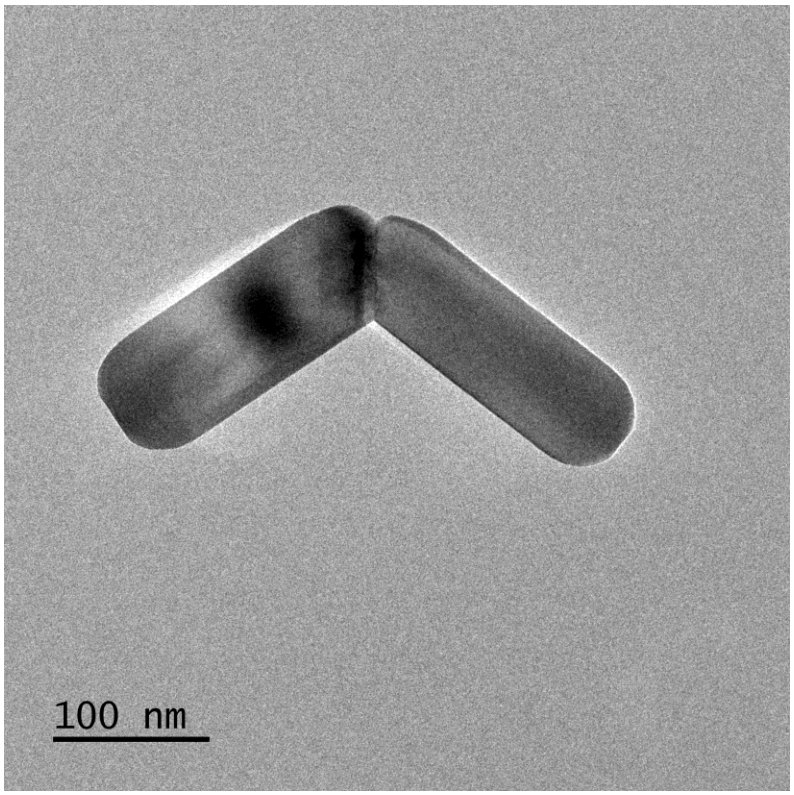


**Figure 3.12:** TEM image of the ZnO nanostructure.

Also, the Zinc (Zn) interaction with GNRs was investigated. A solution of Zn dust mixed with GNRs solution with 0.5 μg/μl concentration was prepared. Figure 3.13 is the SEM image of the Zinc dust on the carbon tape where non-uniform spherical particles are present. A tapered fiber was tweezed using a 1064 nm laser (8.5 mW power) with the prepared solution. SEM image shows the ring-like distribution of Zn and GNRs along the fiber length (Figure 3.14). The inset image is a zoomed view of one ring with spherical Zn particles.

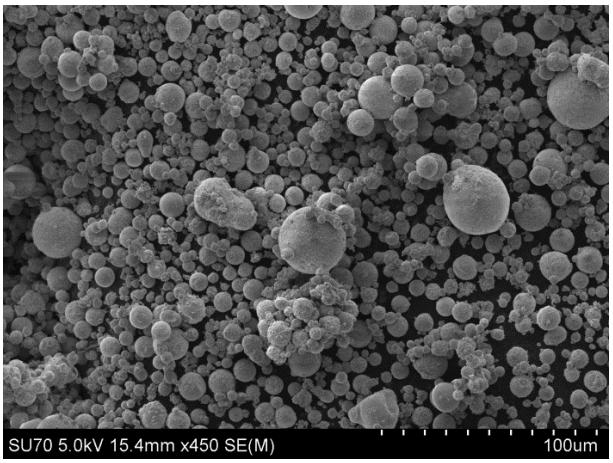


**Figure 3.13:** SEM image of Zn dust on a carbon tape.

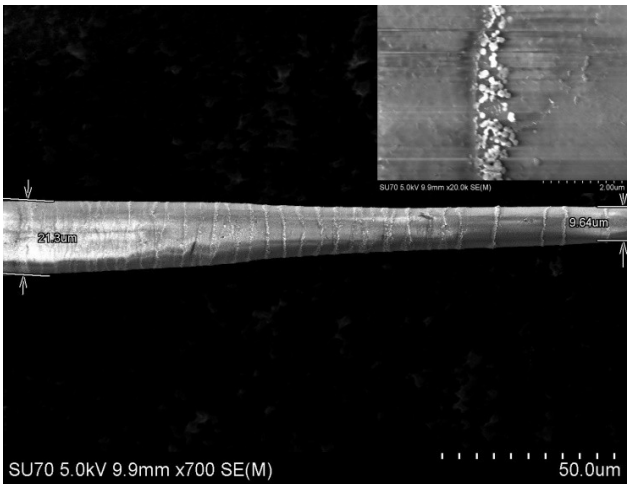


**Figure 3.14:** An SEM image showing the plasmonic structure of Zn and GNRs was obtained using single tweezing. Inset is the magnified image of one of the rings.

## 3.4 Conclusion

The procedure of preparing the plasmonic structure of Zn and ZnO nanostructures with GNRs using optical tweezing was demonstrated. The effect of tweezing conditions, such

as single and double tweezing, on the distribution of Zn and ZnO was presented. The average width and separation between rings for single tweezing was ∽ 9.0 μm and ∽ 7.22 μm. And for double tweezing, the average width and separation between rings was ∽ 5.0 μm and ∽ 7.5 μm. However, double tweezing helped to cover the tip region of the tapered fiber and regions between two rings more comapared to single tweezing. Also, the distribution of ZnO along the fiber without using a laser was explored. This work is a preliminary step towards fabricating a ZnO-based SERS substrate, which will have applications in developing biosensors.

# Chapter 4

## Gold Nanorods (GNRs) preparation and their applications in SERS

*In **this chapter**, gold nanorods (GNRs) using a seedless synthesis method were synthesized, which have LSPR ~ 785 nm wavelength. Prepared GNRs were characterized using a UV-visible spectrophotometer and TEM. They were successfully tweezed on the tapered fiber, and LoD for CV was determined.*

### 4.1 Introduction

Noble metals are the elements that fall in the d-block category on the periodic table and have complete d-filled orbitals. Such elements are Gold (Au), Silver (Ag), and Copper (Cu). These elements are also known as coinage metals and have a historical association with royalty and nobility. The electronic configurations for Au, Ag, and Cu are [Xe] $4f^{14}$ $5d^{10}$ $6s^1$ (or [Xe] $4f^{14}$ $5d^9$ $6s^2$), [Kr] $4d^{10}$ $5s^1$ (or [Kr] $4d^9$ $5s^2$), and [Ar] $3d^{10}$ $4s^1$ (or [Ar] $3d^9$ $4s^2$), respectively, obtained from Aufbau *principle* [126]. These metals exhibit a unique optical property known as surface plasmon resonance (SPR) because of the one free electron in the s-shell (outer shell). SPR can be understood from Otto and Kretschmann

configurations, which describe the interaction of incident light and thin metal (Au or Ag) films (nm range). At a particular angle of incidence, incident photons couple with the free electrons in a partially filled conduction band in a metal film, creating a resonant oscillation known as surface plasmon [127]. Drude's model, also known as the Drude-Lorentz model, is a classical theory that describes the behavior of electrons in a metal. It was first proposed by a German physicist, Paul Drude, in 1900 and later modified by a Dutch physicist, Hendrick Lorentz, in 1905. The Fermi energy level in gold, also known as the Fermi level, can be defined as the highest energy level at absolute zero temperature (0 Kelvin). For pure gold, at 0 Kelvin, the Fermi energy level is estimated to be around 5.53 electron volts (eV) above the valence band maximum. The Fermi energy level determines metals' electronic and optical properties [128].

Gold (Au) and Silver (Ag) have many applications as their SPR is in the visible spectrum (∽400 nm - ∽800 nm). Nanoscience explores the materials on nanometer (nm) lengths. In ancient times, the application of Au and Ag nanoparticles (NPs) can be seen in one of the famous artifacts from the Roman Empire (AD400), "The Lycurgus cup," which is now exhibited in the British Museum. It is made up of a glass embedded with slight Au + Ag nanoparticles, which show red and green colors under transmitted and reflected light, respectively [129].

In 1908, Gustav Mie developed and described the mathematical explanation of how light scatters by gold colloids under plane-wave illumination using Maxwell's electromagnetic equations. This was later known as Mie's theory or Mie scattering and proved to be an accurate formalism that describes the surface plasmon resonance (SPR) of nanomaterials [130]. Mie scattering is when an isolated spherical metal particle interacts

with the light, and the particle size is small, comparable to the wavelength of illuminating light. By solving Maxwell's equations with specific boundary conditions, the expressions for the extinction, scattering, and absorption cross-sections ($C_{ext}$, $C_{scat}$, and $C_{abs}$) are obtained, which are the first step to understanding the optical properties of the nano-metallic particles and the nature of the surrounding medium [131]:

$$C_{ext} = 2\pi/k^2 \, \mathrm{Re} \sum_{n=1}^{\infty} (2n+1) \quad (1)$$

$$C_{scat} = 2\pi/k^2 \sum_{n=1}^{\infty} (2n+1) \, (|a_n|^2 + |b_n|^2\} \quad (2)$$

$$C_{abs} = C_{ext} - C_{scat} \quad (3)$$

where $a_n$ and $b_n$ are the scattering coefficients that can be obtained solving maxwell's equations in spherical coordinates [131], also known as Mie coefficients, and k is the wave vector, $k = \omega^2\sqrt{\varepsilon_m \mu}$, resultant of the 1-dimensional light wave equation, in the surrounding medium with permittivity, $\varepsilon_m$, magnetic permeability, $\mu$, and angular frequency, $\omega$, of the exciting light [131]. The Stratton approach was later developed by Julius Adams Stratton in 1941 [132] to derive expressions for the scattering coefficients.

## 4.2 Gold nanorods synthesis methods

This section discusses different gold nanorod (GNRs) synthesis methods, chemicals used during the reaction, and their respective roles. We also discussed the structure of GNRs and their stability.

The tunable plasmonic properties of gold nanorods in the near visible (TSPR – Transverse Surface Plasmon Resonance) and near-infrared regions (LSPR – Longitudinal Surface Plasmon Resonance) make them more advantageous for various applications, including biomedical imaging, sensing, environmental monitoring, food safety, and security. Since gold (Au) is a noble metal (corrosion resistant) that is chemically stable in air and has high compatibility (e.g., low toxicity, non-reactive in biological or chemical environments) with most molecules, it is desirable for biosensing [133]. For synthesized GNRs, a uniformity of nanorods' size and shape and chemical and thermal stability are highly desired. Several methods have been used to prepare gold nanorods with their advantages and disadvantages, such as (1) the template method [134], (2) electrochemical method [134], (3) seeded growth (seed-mediated) method [134], and (4) seedless method [135]. A detailed description of these methods is elaborated below:

***4.2.1 Template method:*** In 1992, Martin et al. proposed a technique known as the "template method" for the synthesis of metallic and polymeric particles, which ensured the precise control of the size, shape, and orientation of the GNRs. The method is based on the gold's electrochemical deposition within an alumina templates membranes' nanoporous pores (diameter = 50 nm). Also, they have shown agreement between their results and the predictions of the Maxwell-Garnett (M-G) theory [136]. In 1994, Martin again used the template method where desired material could be used within the pores of a nanoporous membrane instead of alumina, where GNR dimensions were controlled carefully. Martin not only prepared GNRs but also polymers, semiconductors, and nanoscopic particles using the template method [137]. Also, he discussed thoroughly the possibility of preparing composite nanomaterials utilizing this technique and proved its

applications in biosensors, bioencapsulation, energy production, etc., with industrial partners' support [138]. To explain the template method schematically, the following steps need to be considered: (i) the alumna template membranes were prepared electrochemically from aluminum (Al) metal-containing cylindrical pores of a uniform diameter, (ii) a small amount of gold (Au) or copper (Cu) was required to provide electro-conductive film for electro-deposition, (iii) the film works as a foundation onto which Au nanoparticles can be grown electrochemically, (iv) finally, synthesized GNRs were dispersed in water via sonication. More detailed information was given in these two references [136],[139]. It was concluded that the GNRs diameter can be controlled by controlling the pore diameter of the template membranes, but it was not straightforward to control the length of the GNRs. In 2000, van der Zande, B.M.I., et al. showed that the nanorod's length could be controlled by the amount of Au deposited within the membrane's pores [139]. The fundamental challenge of this method is that it is a low-yield, time-consuming process requiring the involvement of specific lab equipment. Despite the disadvantages, nanomaterials' basic optical properties and effects were studied and verified using the template method.

***4.2.2 Electrochemical method:*** In 1997 and 1999, Wang's group used an electrochemical approach to synthesize a high-yield aqueous gold nanorods solution [140],[141]. Their work was an extension of the work of Reetz et al. in 1994 [139], who showed the synthesis of nanostructure metal clusters within reverse micelles in organic solvent systems. The method involves a synthetic route for preparing high-yield gold nanorods, and an appropriate surfactant called Cetyl trimethylammonium bromide (CTAB) was employed to control the cylindrical shape of the nanorods. The experiment was conducted using a

simple two-electrode-type cell, and a schematic of the system is given in the references [141,142]. A gold metal plate of dimensions 3 x 1 x 0.05 cm was used as an anode, and a platinum plate with the exact dimensions was used as a cathode. Both electrodes with a 0.25 cm distance apart were placed in an electrolyte aqueous solution in the presence of a cationic surfactant called CTAB and a rod-inducing co-surfactant. The function of CTAB in this reaction is not only to work as an analyte but also as a stabilizer for the GNRs, which prevents their growth along a particular face. Further, in the synthesis process, bulk gold metal from the anode was converted into gold nanoparticles at the interfacial region of the cathodic surface and within the electrolyte solution. During the process, a controlled temperature (38º C) and the typical current of 3 mA for 30 minutes were maintained, and the reaction happened under ultrasonication.

Acetone is added to the electrolyte solution, and its function is to loosen the CTAB micellar framework and to induce the rod's growth while allowing CTAB to prevent it from aggregating or clumping together. At this stage of experiments, the reaction mechanism is unclear. However, the primary factor controlling the AR was the presence of a silver plate (the exact dimensions of the gold and platinum plate used in the experiment) in the electrolyte solution. The silver (Ag) ions were formed when a redox reaction happened between Au ions from the anode and silver metal. Therefore, Wang and the group concluded that the concentration of Ag ions and their release speed would influence the length of the prepared nanorods. However, the complete mechanism was unknown at that time.

Although it is a successful method to prepare GNRs, one cannot achieve precise control over the shape, size, and AR. This method produces GNRs with a broader size

distribution which lack monodispersity, which can impact their potential applications. Another drawback is that this method requires sophisticated experimental set-up, including precise control of electrical parameters, electrode configuration, electrolyte composition, etc., and this complexity can cause difficulty in replicating the results.

***4.2.3 Seeded growth (seed-mediated) method:*** The most conventional and widely used method for GNRs synthesis is the seed-mediated method, and the pioneering work to develop this approach was done by two research groups: N. R. Jana and co-workers [143] and B. Nikoobakht and co-workers [144]. In 2001, N. R. Jana et al. studied the role of CTAB solution in the synthesis process to control the rod yield, its assistance in rod formation, stabilization of nanorods, and their preparation with AR= 4.6±1.2 and 18±2.5. It was established that the seed-mediated method could prepare uniform-size nanorods with high AR [145]. In 2003, B. Nikoobakht et al. [144] replicated the recipe to prepare GNRs with high AR from reference [145]. From the experiment, it was confirmed that the results were reproducible with AR in the range of 1.5 to 4.5, but to grow nanorods with higher AR, i.e., 4.6 to 10, a binary surfactant mixture of benzyldimethylhexadecylammoniumchloride (BDAC) and CTAB was used; this method is known as a co-surfactant method. The AR of GNRs can be altered by varying the ratio of CTAB and BDAC so that localized surface plasmon resonance (LSPR) is from 900 nm to 1300 nm. The growth mechanism and role of chemicals were discussed. In 2004, T. K. Sau and C. J. Murphy [146] proposed a. recipe to prepare GNRs using the seeded growth method of AR from approximately 2 to 4, corresponding to the GNRs length of 20 to 100nm. The yield of short GNRs was approximately 97 %. They also explained how crucial the role of silver (Ag) ions was in achieving the maximum yield of short GNRs,

which was also reported by El-Sayed's group [144]. The primary concern of GNRs synthesis was to control the yield, shape, size, tuning, reproducibility, etc. In 2005, L. Gou and C. J. Murphy [147] turned to a widely used GNRs synthesis method: seed-mediated. Further, they studied the role and effect of ascorbic acid (AA) used in the reaction as a reducing agent to control the shape of the GNRs. It was observed that the presence of unreduced Au ions in the solution occurred when the ratio of AA to chloroauric acid or gold salt ($HAuCl_4$) was not adequately balanced. The authors conducted different approaches to reducing Au ions, such as heating the solution to 100 ° C for various intervals and adding more AA. It was determined that to reduce the gold salt completely, the AA-to-gold salt ratio should be at least 3:2. The heating effect caused a blue shift in the longitudinal peak and a red shift in the transverse peak. Further, the optical properties of the original and modified GNRs were studied. In 2008, D. K. Smith and B. A Korgel [148] extended the research by using CTAB obtained from 10 different suppliers for GNRs synthesis using a silver-assisted seed-mediated method. Additional modifications have been made to improve the yield by up to 100%. It was concluded that the yield of GNRs highly depends on the CTAB used while keeping the recipe and all other experimental conditions similar. Thus, impurities in the CTAB can strongly affect the colloidal growth rate of GNRs formation. Therefore, it was established that the purity of chemicals plays a crucial role in high-yield, monodispersed GNRs synthesis.

The basic steps involved in the seed-mediated methods are as follows [145]:

1. Preparation of seed solution (growth solution 1): First, a CTAB solution of the required molar concentration was prepared, which acts as a capping agent for the GNRs, followed by a chloroauric acid (HAuCl4) solution with the needed

concentration, also called the “gold precursor solution.” For seed formation, an aliquot from the $HAuCl_4$ solution was taken and mixed with a CTAB solution while placed on a magnetic stirrer. Then, ice-cold sodium borohydride (NaBH4) was added, which acts as a reducing agent while stirring.

2. Preparation of growth solution (growth solution 2): In a clean beaker, prepare a growth solution containing appropriate molar concentrations of HAuCl4 and CTAB, and ascorbic acid, another freshly prepared weak reducing agent, was added while stirring.
3. Gold nanorod growth reaction: Now, add an aliquot of growth solution one into growth solution two where no stirring was done and kept in the dark for the reaction to occur.

Using this 3-step seed-mediated method, the GNRs prepared were uniform in size, had a well-controlled AR, and had strong absorption for wavelengths up to 1800 nm. The stability of the GNRs was more than a month.

The major limitation of this method was that gold seeds need to be freshly prepared for the reaction and cannot be preserved for a long time.

**4.2.4** ***Seedless method:*** The previously mentioned methods are time-consuming, and the experimental parameters' requirements are significantly more strict than the seedless method (also known as the one-pot synthesis method) [135]. In 2005, N.R. Jana [149] proposed the seedless method and discussed the major drawback of the seed-mediated method, which states that only if seed size (gold nanoparticles) is < 3nm is it possible to make GNRs with a yield greater than 90% but to produce seeds of this dimension is a

challenge. Therefore, it was required to develop a non-seeding or seedless method. N.R. Jana proposed a silver-assisted seedless method where seeds were prepared in situ by adding a strong reducing agent, sodium borohydride ($NaBH_4$). AR was controlled by controlling the concentration of $NaBH_4$ in the reaction. GNRs with AR from 1 to 5 can be synthesized using this method up to the gram scale, and the crystal structure of GNRs remained the same as the seed-mediated method. Hence, these results show a positive and successful approach to synthesize GNRs. The rough control of the size and shape was achieved by changing the molar ratio of strong (Sodium Borohydride ($NaBH_4$)) and weak (Ascorbic Acid (AA)) reducing agents. In 2009, [150] K. Okitsu and co-workers used a seedless (or one-pot synthesis) method to prepare GNRs using a sonochemical method, which allows a unique route to develop metallic nanorods by reducing Au ions in an aqueous solution. Experimentally, it was discovered that the shape and AR of GNRs strongly depended on the solution's pH. Although the detailed mechanism of the reaction is unknown, increasing pH caused the AR of GNRs to decrease. The characterization of the GNRs was done using TEM and UV-vis spectrums. In 2011, C. Bullen and co-workers [151] adopted a different approach to synthesizing GNRs using the seedless method. In this method, authors have developed a continuous flow method where two stock solutions were sent to a rotating tube processor (RTP) connected in series with a narrow channel processor (NCP) for intense and uniform mixing and to control the nucleation, which controls the growth of GNRs. Nanorods prepared using this method were stable for days, and the recipe was reproducible, confirmed by TEM and UV-Vis results. Because of the growing demand for nanomaterials and their potential applications in various fields, researchers were developing more efficient and straightforward methods

to prepare GNRs. In 2012, M. R. K. Ali et al. [135] used a one-pot seedless synthetic technique to synthesize small monodispersed GNRs of AR of approximately 4, 5, and 3.3 with average dimensions of 18 x 4.5 nm, 25 x 5 nm, and 15 x 4.5 nm, respectively. This group again studied the role of the pH, and it was discovered that at optimized pH (< 2), it is possible to produce small monodispersed GNRs solution when CTAB concentration was appropriate in growth solution, which was a limitation in Jana's work [149]. In this method, the authors showed that by changing the amount of $AgNO_3$ but keeping the concentration the same in the reaction, the AR of NRs was altered, which thus gives an opportunity in the seedless method to tune the AR of nanorods.

Compared with the seed-mediated method, the seedless method is more convenient and has attracted much more attention because of its simpler reaction process, where the reaction happens in one vessel [152]. Also, the synthesis of a high yield of high-quality gold nanocrystals of different shapes, such as rods, cubic, concave cubic, quasi-spherical, and trioctahedral, was possible using the seedless synthesis method [153].

## 4.3 GNRs synthesis recipe

In this chapter, a reproducible seedless method or one-pot method used for GNRs synthesis is described. However, slight modifications have been made in the recipe from M. R. K. Ali et al. article to prepare high-quality GNRs that have absorption in the wavelength range 700-800 nm [152].

### 4.3.1 Materials used

Hexadecyltrimethylammonium bromide (CTAB), Ascorbic Acid (AA), Sodium borohydride ($NaBH_4$), and a Gold (III) Chloride solution (30 wt. % in dilute HCl) ($HAuCl_4$) were purchased from Sigma-Aldrich. Silver nitrate ($AgNO_3$) was obtained from Thermo Fisher Scientific. All the chemicals were used as received. The glass containers used in this reaction were cleaned before using aqua regia and nanopure water. Aqua regia is a mixture of concentrated nitric acid and hydrochloric acid in a ratio of 1:3 by volume.

| **Chemicals used** | **Molar concentration** | **Amount used** |
|---|---|---|
| CTAB | 0.2 M | 5 ml |
| Silver nitrate ($AgNO_3$) | 4 mM | 265 µl |
| Ascorbic Acid (AA) | 70 mM | 80 µl |
| Sodium borohydride ($NaBH_4$) | 0.01 M | 15 µl |
| Gold (III) Chloride solution (30 wt. % in dilute HCl) ($HAuCl_4$) | 1 mM | 13 µl |

**Table 1:** Table showing the concentration and volume of each chemical used in the seedless method to prepare GNRs.

Table 1 describes the chemicals used along with the molar concentrations. The chemicals were measured using a Sartorius Microbalance (CASES, Lakehead University).

### 4.3.2 Mixing of CTAB in nanopure water

The utmost challenge faced during synthesizing GNRs was mixing CTAB in water. Several methods have been tried; for example, a magnetic stirrer alone was used, but a significant amount of foam was observed on the surface, which is not desirable for performing the reaction. Secondly, sonication at room temperature did not work well, as shininess (indicating the precipitation of CTAB) in the solution returned after 1 to 4 hours of sonication, depending on how long the solution was sonicated. Finally, a stirring hot plate[2] was used at approximately 60°C (shown in Figure 4.1), which can mix CTAB powder in nanopure water within 10-20 minutes.

[2] Model 2 10T from Fisher Scientific

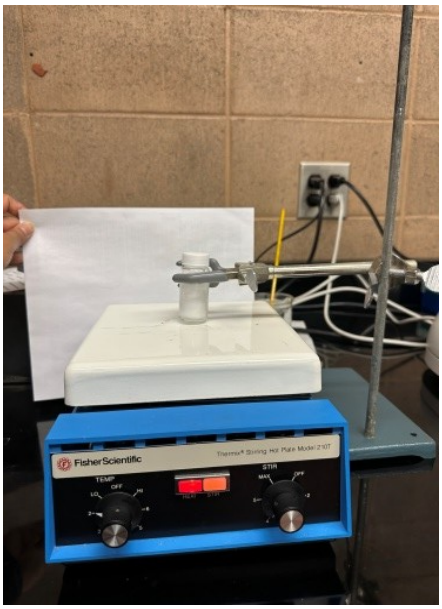


**Figure 4.1:** An experimental set-up shows the mixing of CTAB in water using a stirring hot plate.

### 4.3.3 Procedure

After mixing CTAB in water, the CTAB solution was brought to room temperature (25 - 30°C) by taking it off the hot plate for about an hour. Then, all the chemicals of the required concentrations were prepared before the reaction, and a fresh ice-cold solution of sodium borohydride was used in all the experiments. The $AgNO_3$ solution was stored in an amber glass vial and kept carefully away from the light. First, 13 µl of 1 mM $HAuCl_4$ solution was added to 5 ml of 0.2 M CTAB solution, and after 2 minutes of vigorous stirring, the solution turned yellowish in color. At this stage, precipitation should not occur. Then, 265 µl of 4 mM $AgNO_3$ was added to the solution, which turned the solution opaque yellowish. A further 80 µl of 70 mM conc. Ascorbic acid (AA) was

added to the solution and stirred vigorously until it turned completely transparent (colorless). The last ingredient added was 15 µl of 0.01 M $NaBH_4$, gradually turning the solution light brown (Figure 4.2(a)). It was observed that after 10 minutes of adding $NaBH_4$, the solution turned dark brownish from the original light brownish color. Then, the reaction was left for about 5 hours and 30 minutes in the dark, where the solution was kept undisturbed for this time interval at room temperature. The color of the solution turned deep brown (Figure 4.2(b)). The temperature was maintained between 25 - 30º C during the reaction.

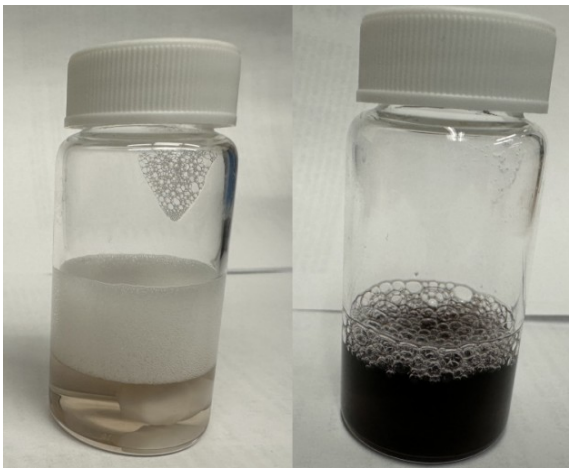

(a) (b)

**Figure 4.2:** Color of the solution (a) right after the reaction and (b) after five and half hours of reaction (or before centrifugation).

### 4.3.4 Centrifugation process

It is essential to centrifuge the solution after the reaction, as concentrated and monodispersed GNRs can be obtained using this process. Centrifugation also leads to the

shape separation of the gold nanoparticles. After five and a half hours in a dark and undisturbed environment, the solution was first sonicated for about ∽ 4 minutes. The solution (4800 µl) was taken in 3 centrifuge vials (1600 µl in each vial), which was then centrifuged for 10 minutes at 14,500 rpm (Figure 4.3 (a)). Figure 4.3 (b) shows the precipitation at the bottom of the centrifuge vial after centrifugation and the supernatant was removed. The supernatant (blue color in Figure 4.3 (a)) can be defined as a liquid that remains above the precipitate after the centrifugation process, which can be carefully removed using a pipette without disturbing the precipitation.

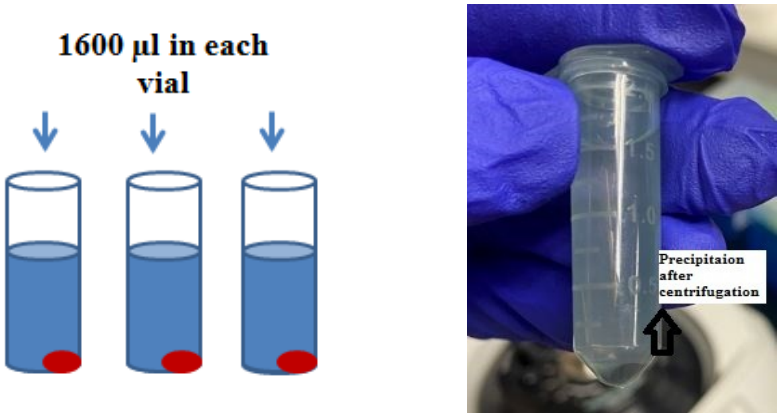


(a) (b)

**Figure 4.3:** (a) sketch showing centrifuge vials (red color shows sedimentation (also known as an original solution after re-dispersing in water) after centrifuging the solution for 10 minutes at 14,500 rpm, (b) the original picture of the vial showing precipitation at the bottom after centrifugation (supernatant was removed).

The supernatant (S) (1600 µl in each vial) was then transferred to 3 different vials. The sedimentation from the original (O) solution was re-dispersed in 1600 µl of water. Both solutions were again centrifuged for 15 minutes at 14,500 rpm (Figure 4.4).

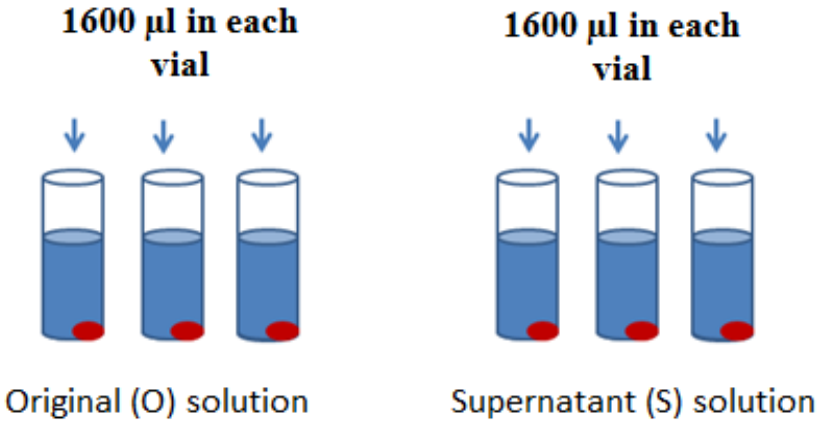


**Figure 4.4:** Original (O) and supernatant (S) solutions were .5 minutes at 14,500 rpm.

The supernatant from the original solution was thrown away, but the supernatant (S1) from the supernatant (S) solution was transferred to 3 different vials. The original (O) and supernatant (S) solutions were again re-dispersed in 1200 µl of water.

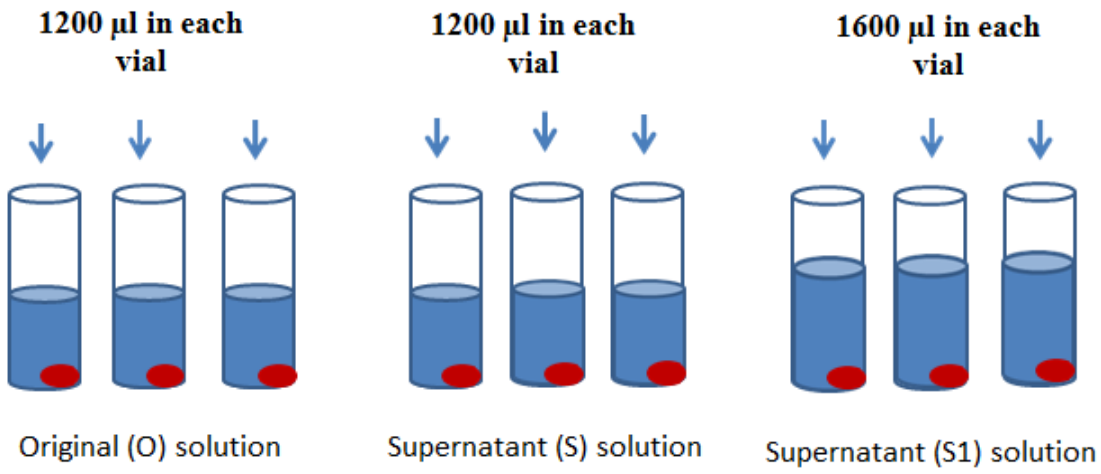


**Figure 4.5:** Centrifuged (O), (S), and (S1) solutions for 18 minutes at 14.500 rpm.

Figure 4.5 shows the final stage of centrifugation; all three solutions (O), (S), and (S1) were centrifuged for 18 minutes at 14,500 rpm and re-dispersed in 1200 µl of water. The centrifuge helps reduce excess CTAB from the solution. In previous attempts, taking clear pictures of GNRs using TEM was challenging as a lot of CTAB was present. Figure 4.6 (a), (b), and (c) shows the original and supernatant solutions (S and S1) images after the centrifugation process. In terms of color, the Original (O) solution looks pink in color, although supernatant solutions (S and S1) look light brownish with a slight change of shade in color.

## 4.4 Instrumentation

The prepared GNRs were characterized using a UV-visible spectrometer[3] and Transmission Electron Microscope (TEM)[4]. Using the above-mentioned instruments, the

[3] Carry-50 spectrophotometer (200 - 1100 nm range)

size, shape, crystal purity, and LSPR properties of GNRs were determined. Figure 4.7 shows the UV-Vis absorption spectra for O, S, and S1 solutions. The Original solution shows only one peak at 525 nm (Transverse Surface Plasmon Resonance (TSPR)), indicating the presence of gold nanoparticles in the solution. The supernatant solutions (S and S1) show the same TSPR peak at 510 nm, indicating the same diameters of GNRs in both solutions and different LSPR peaks at 797 nm and 785 nm, respectively, indicative of different GNRs lengths. The UV-Vis spectrum from solutions S and S1 shows well-defined high-quality GNRs; the higher ratio between LSPR and TSPR absorption means a higher rod-shape percentage is present than that of other shapes. In conclusion, UV-visible spectroscopy and TEM are complementary, and both techniques should be used for GNRs characterization.

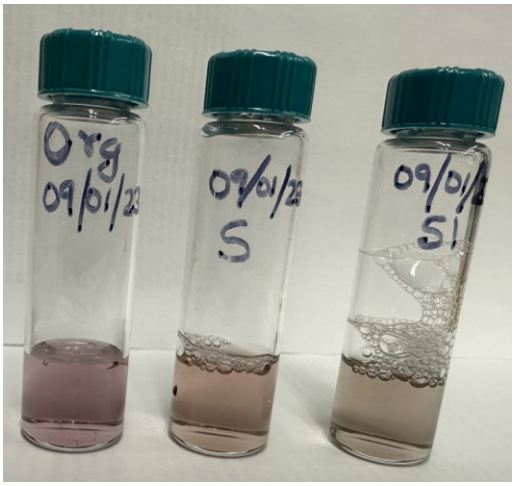


(a) (b) (c)

**Figure 4.6:** (a) Original (O), (b) supernatant (S), and supernatant (S1) solution color appearance after centrifugation.

---

[4] JEOL Model- JEM 2100PLUS

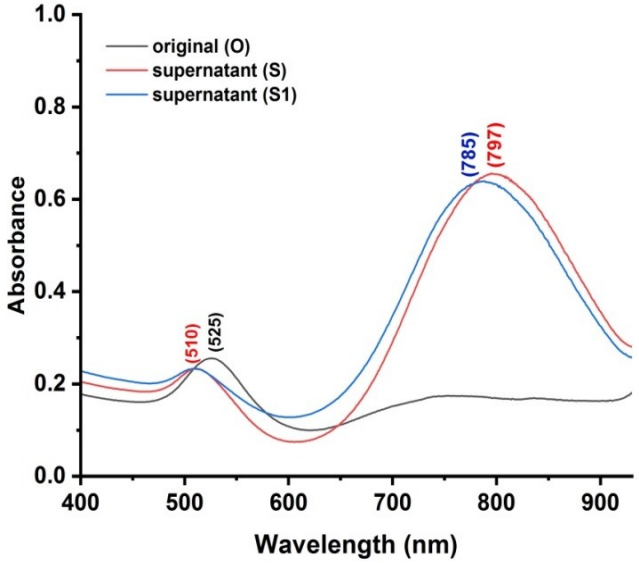


**Figure 4.7:** UV-visible absorption spectra comparing (O), (S), and (S1) solutions.

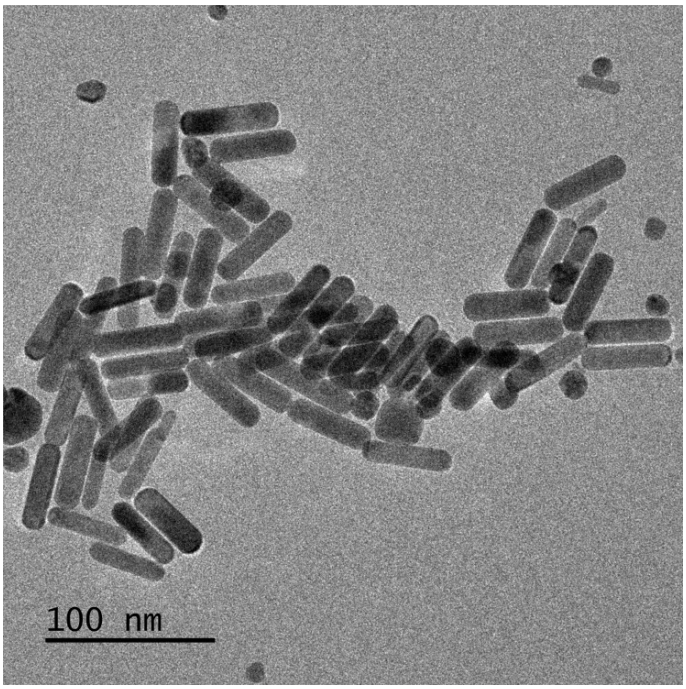


**Figure 4.8:** TEM image of the lab-prepared GNRs (mean AR = 3.6 ± 0.6).

The TEM samples were prepared by placing a 5 µl drop of GNRs solution on a carbon-coated copper grid (TEM sample holder). The sample-coated grid was dried overnight before the characterization. Figure 4.8 shows the TEM image of the prepared GNRs of mean AR 3.6±0.6. The uniformity in the sizes of GNRs shows that the recipe worked well. A series of experiments established that the recipe is reproducible and GNRs were stable for a few days (the fact that GNRs were tweezed after 1 week of preparation and Raman was performed successfully). Figure 4.9 indicates the high crystallinity of the synthesized GNRs because the inter-planar spacing, d, represented by the miller indices, is 0.20 nm, which corresponds to the lattice plane of gold [152].

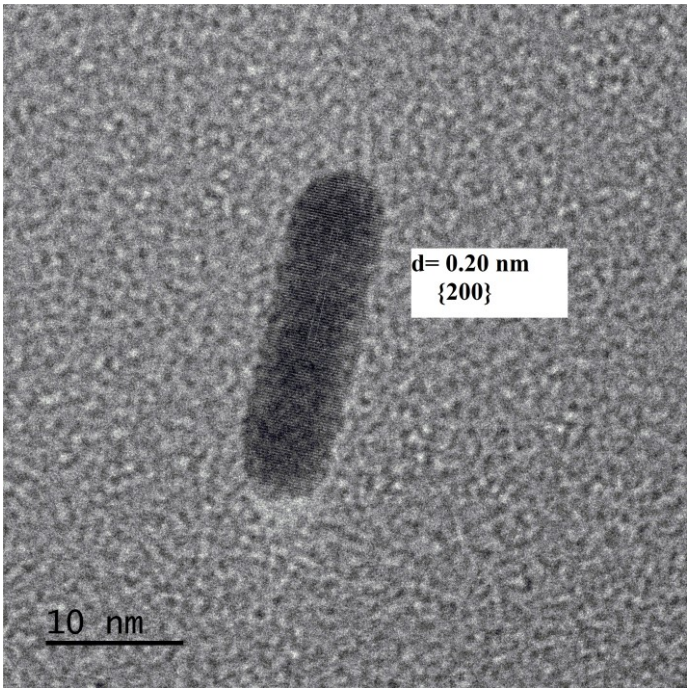


(a)

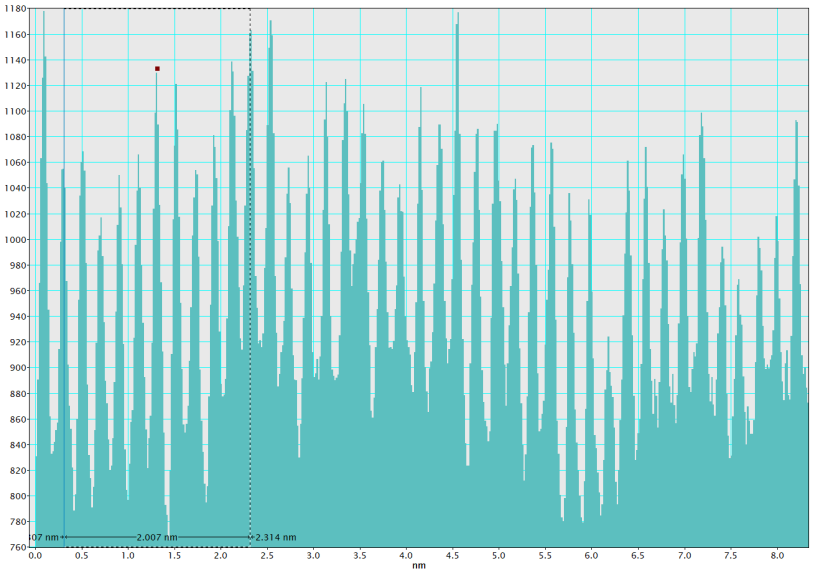


(b)

**Figure 4.9:** TEM image of GNRs showing the inter-planar spacing, d= 0.20 nm, (b) profile confirming the value of interplanar spacing, d.

## 4.5 CTAB and cytotoxicity of CTAB molecules

The most crucial ingredient choice in GNRs synthesis is the surfactant. The literature shows that the suitable surfactant choice influences the anisotropic crystal growth. In the above-described method, CTAB was used as a surfactant. Although several articles have reported the synthesis of GNRs without using CTAB [154,155] resulting in a less monodispersed sample and low reproducibility, which can typically be achieved with CTAB.

The bilayer of positively charged CTAB molecules covers the GNRs and is known to form rod-shaped micelles responsible for spherical seeds' anisotropic growth [156-158]. Both experimental [159] and molecular dynamics (MD) [158] simulation results established the fact that CTAB forms a bilayer onto the gold surface. GNRs in aqueous solution are surrounded by a capping agent (surfactant). Therefore, to see the thickness of the surfactant (CTAB), S. Gomez-Grana et al. studied the structure of the CTAB bilayer. They determined the bilayer thickness ($\backsim$ 3.2 nm) using a small angle X-ray (SAXS) and neutron (SANS) scattering [160]. Also, the bilayer can be easily disrupted if the CTAB concentration is lower than its critical micelle concentration (CMC), resulting in the aggregations of GNRs, which is not desirable. Another essential feature is that CTAB bilayer molecules are unevenly distributed on the GNRs surface because of the variation of surface curvature between the longitudinal and transverse surfaces. J. A. da Silva et al. studied the effect of the curvature of the GNR surface on the CTAB adsorption. They verified the inhomogeneity in the packing density of the adsorbed CTAB layer, where the

highly curved tips have a lower density of CTAB than the longitudinal facets, making the tip functionalization more favorable than the sides [158,161].

GNRs have numerous applications in the intensive studies of nanomedicine, including drug delivery, cellular imaging, therapeutics, biomedical diagnostics, etc. [162,163]. So why is functionalization important? Despite the advantages of CTAB as a surfactant, it is essential to consider its toxicity, limiting the use of GNRs in biological applications, J. Wan and co-workers studied the effect of CTAB-GNRs on different cells, and the cell viability results confirmed the toxic effect on the cultured cells, as CTAB can disrupt the lipid bilayer of the cell membrane [164]. It is possible to use various methods to functionalize CTAB-coated GNRs using peptides, polymers, lipids, and surfactants to make GNRs biocompatible [165,166]. The ligand exchange method is the most widely used method to remove CTAB from the surface of GNRs and replace them with ligands or biomolecules. Out of many surface ligands, polyethylene glycol thiols (PEG-SH) show some explicit advantages such as (1) they have a hydrophilic nature, which enhances the suspension stability of GNRs (highly colloidal stability), (2) good biocompatibility, (3) long plasma circulation time, and (4) low cytotoxicity [167-169]. Many researchers have reported various functionalization methods to conjugate GNRs with PEG to remove the cytotoxic effect arising from CTAB used in GNRs synthesis [166,169-174]. The stability of PEGylated GNRs was determined to be at least one month at room temperature. Also, it was established that it is essential to functionalize GNRs as soon as they are synthesized to make them stable for a more extended period, as CTAB-coated GNRs undergo morphological changes over time [175].

## 4.6 Role of each chemical used in the reaction

The reaction mechanism of the seedless method is not clear yet; however, the role of each chemical in the reaction is understood. In the seedless method, often to produce small GNRs, seeds and rods are formed consecutively without having two separate stages, and it is very sensitive to synthesis parameters. In the first step, the mixing of $HAuCl_4$ in CTAB (molecular formula of CTAB: $CH_3(CH_2)_{15}(CH_3)_3N^+Br^-$) solution results in strong interactions between $AuCl_4^-$ and CTAB. The positively charged ammonium head group from CTAB binds tightly to the gold surface through electrostatic interactions [176,177]. The mechanism of the ion-pair formation between $HAuCl_4$ and CTAB is as follows [178]:

$$HAuCl_4 \rightarrow AuCl_4^- + H^+ \quad (1)$$

Equation (1) shows that gold (III) chloride ($HAuCl_4$) completely dissociates into $AuCl_4^-$ and $H^+$ Ions in aqueous solution. The next step is the ionization of CTAB, as shown in Equation (2).

$$CH_3(CH_2)_{15}(CH_3)_3N^+Br^- \rightarrow CH_3(CH_2)_{15}(CH_3)_3N^+ + Br^- \quad (2)$$

Now, the ionized $CH_3(CH_2)_{15}(CH_3)_3N^+$ (or CTA) and $AuCl_4^-$ forms an ion-pair complex (Equation (3)), resulting in the yellow-orange colored solution.

$$CH_3(CH_2)_{15}(CH_3)_3N^+ + AuCl_4^- \xrightarrow{Fast} CH_3(CH_2)_{15}(CH_3)_3N - AuCl_4 \quad (3)$$

(color: orange-yellow)

The same color was observed while performing the experiments for GNR synthesis using the seedless method. The above theory was supported by J. Perez-Juste and co-workers in 2005 [134] showing the adsorption of $AuCl_4^-$ onto the head group of CTAB.

Upon vigorous stirring of CTAB and $HAuCl_4$, the four chloride ligands from $AuCl_4^-$ will be replaced by bromide ions present in CTAB and then tightly bind to $CH_3(CH_2)_{15}(CH_3)_3N^+$ ($CTA^+$) micelles.

$$[AuCl_4]^- \leftrightarrow [AuCl_3Br]^- \leftrightarrow [AuCl_2Br_2]^- \leftrightarrow [AuClBr_3]^- \leftrightarrow [AuBr_4]^- \quad (4)$$

Equation (4) supports the color change when $HAuCl_4$ was mixed in CTAB from pale yellow to dark orange yellow. Out of the three oxidation states of the gold, Au (I) is the most stable for forming GNRs. In the synthesis process, not only the dissolution of gold salt is important, but also the completion of ligand exchange, which also plays an important role [179].

In 1999, S. S. Chang and co-workers [180] used an electrochemical method to synthesize an aqueous GNRs solution and experimentally established that the amount of silver ions and their release speed controls the length of the GNRs. Until this time, the role of silver ions was unclear. Later, it was confirmed by many researchers that $Ag^+$ ions have proven to be a significant breakthrough that is responsible for controlling the AR of the GNRs with high yield and is said to be acting as a co-surfactant [135,145,150]. The other alternative for silver nitrate is any other hydrophobic co-surfactant, such as tetraoctylammonium bromide ($TC_8AB$), used to synthesize GNRs of AR from 2.6 to 7.6 [140]. The presence of silver ions is crucial to forming high-quality single-crystalline

GNRs of smaller AR with high yield [175,181]. From the literature, it was understood that Ag ions are adsorbed onto the gold nanoparticles' surface as a silver(I) bromide complex (either AgBr2- or CTA-Br-Ag+), which acts as a facet-specific capping agent and forms a monolayer over Au, thereby restricting the growth of GNRs and stabilizes their surface [135,146,181,182]. B. Nikoobakht and co-workers supported the concept of AgBr adsorbing onto the GNRs surface, which may decrease the charge density on bromide ions, leading to less repulsion between the neighboring headgroups, resulting in CTAB elongation [144]. Experimentally, it was observed that different amounts of AgNO3 yield different dimensions of GNRs [183]; for example, when silver ion amount was changed from 270 µl to 290 µl, the AR changed from ∽ 5 to ∽ 5.3, respectively, all other quantities were kept same [135]. Hence, an increase in the amount and concentration of AgNO3 results in the increased AR, which causes a red shift in the longitudinal plasmon band observed using UV-Vis spectra [135,151,184]. However, this is not always the case; B. Nikoobakht and co-workers showed that when the AgNO3 concentration was increased up to a certain number (> 0.00012 M), the GNRs AR decreased [144]. Jana et al. reported that the GNRs synthesized without Ag ions were converted into Nanoparticles (NPs) [143]. However, C. J. Murphy and co-workers reported that the highest AR (or longer GNRs) obtained without Ag ions was ∽ 25 but with a lower yield [181]. Many researchers have established that a binary surfactant mixture of CTAB and benzyldimethylhexadecylammoniumchloride (BDAC) can synthesize GNRs with longer AR. GNRs with plasmon bands from 900 to 1300 nm can be prepared by changing the BDAC/CTAB ratio from 16 to 2 [144].

The structure of CTAB and its arrangement, along with the non-precise location of Ag atoms on the gold nanorod surface, was described [185]. Overall, the growth kinetics of the dimensions (length and width) of GNRs can be controlled by changing the CTAB and silver ion concentrations. It was also determined that to control the AR of GNRs and to maintain the width < 5 nm using the seedless method, it is essential to increase the CTAB concentration in the solution [135]. Ascorbic acid (AA) (molecular formula: $C_6H_8O_6$) is a weak reducing agent, and sodium borohydride ($NaBH_4$) is a potent reducing agent, and both play an essential role in the formation of GNRs in the micellar template [149]. The suitable amount of ascorbic acid reduces Au (III) to Au (I) (known as first reduction), which turns the solution from yellow to colorless (observed during the experiment) and can be expressed in the form of equation (5) [144,175,186,187]. The reduction rate depends on the concentration and amount of AA used in the reaction.

$$Au^{3+} + 2^{e-} \rightarrow Au^{1+} \qquad (5)$$

Another essential feature of AA is that it only reduces Au ions if the pH of the solution is basic in nature [144]. To ultimately reduce gold salt from Au (III) to Au (0) and to form GNRs, the ratio of AA to gold salt should be 3:2 [147,186]. Also, to obtain the specific LSPR band for GNRs, the molar ratio of AA to metal salt should be chosen carefully. Experimentally, it was found that if the ratio of molar concentrations of AA to metal salt is between 1:1 and 3:2, then the AR and yield are increased, and no GNRs were observed below 1:1. Larger but dog-bone-shaped GNRs were formed when concentration was above 3:2 [186].

The second reduction was done by a strong reducing agent, sodium borohydride ($NaBH_4$), to enhance further the reduction from Au (I) to Au (0) (equation (6)) [186].

$$Au^{1+} + 1^{e-} \rightarrow Au^{0} \qquad (6)$$

In the seedless method, one strong reducing agent, sodium borohydride ($NaBH_4$), and one mild reducing agent, ascorbic acid (AA), were introduced in the micellar solution of metal salt. The strong reducing agent starts nucleation, and the mild reducing agent helps the nanoparticles to grow; by controlling the ratio of AA and $NaBH_4$, the nucleation rate can be controlled, which allows forming GNRs of different AR along with differently shaped nanoparticles [149].

Overall, there is strong experimental evidence that the uniformity, purity, and high yield of synthesized GNRs of the desired LSPR band depends upon parameters such as - molar concentrations, volumes (or amount of chemicals), pH, temperature, mixing, etc., of the chemicals used in the reaction.

## 4.7 Surface-Enhanced Raman Scattering (SERS) applications

The synthesized gold nanorods (GNRs) were tweezed on the tapered fiber surface using a 1064 nm laser wavelength. We obtained the ring-like distribution (Figure 4.10) described in **Chapter 2** along the tapered length, which suggests the successful tweezing of the prepared GNRs. The SEM images confirmed that the GNRs were intact after tweezing (Figure 4.11).

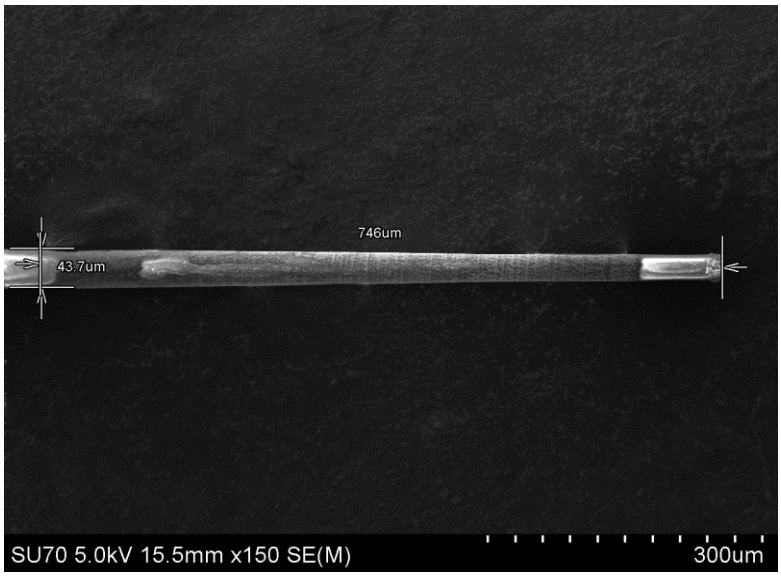


**Figure 4.10:** SEM image showing the GNRs distribution on the tapered fiber.

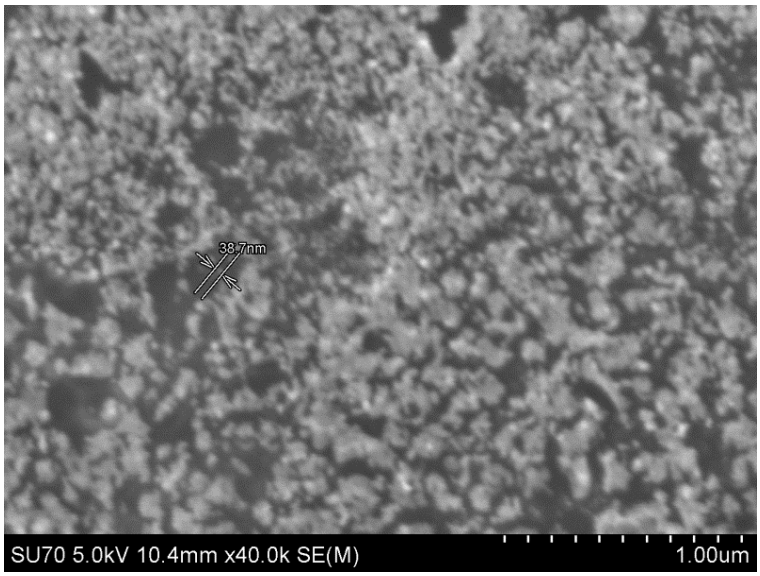


**Figure 4.11:** Magnified SEM image showing the intact GNRs on the fiber surface.

The presence of Au on the tapered fiber surface was confirmed using Scanning Electron Microscopy – Energy Dispersive X-ray Spectroscopy (SEM-EDS) results. SEM allows the visual representation of the area of interest, but EDS, also called EDX, can confirm the element in a precise location on the fiber surface (Figure 4.12).

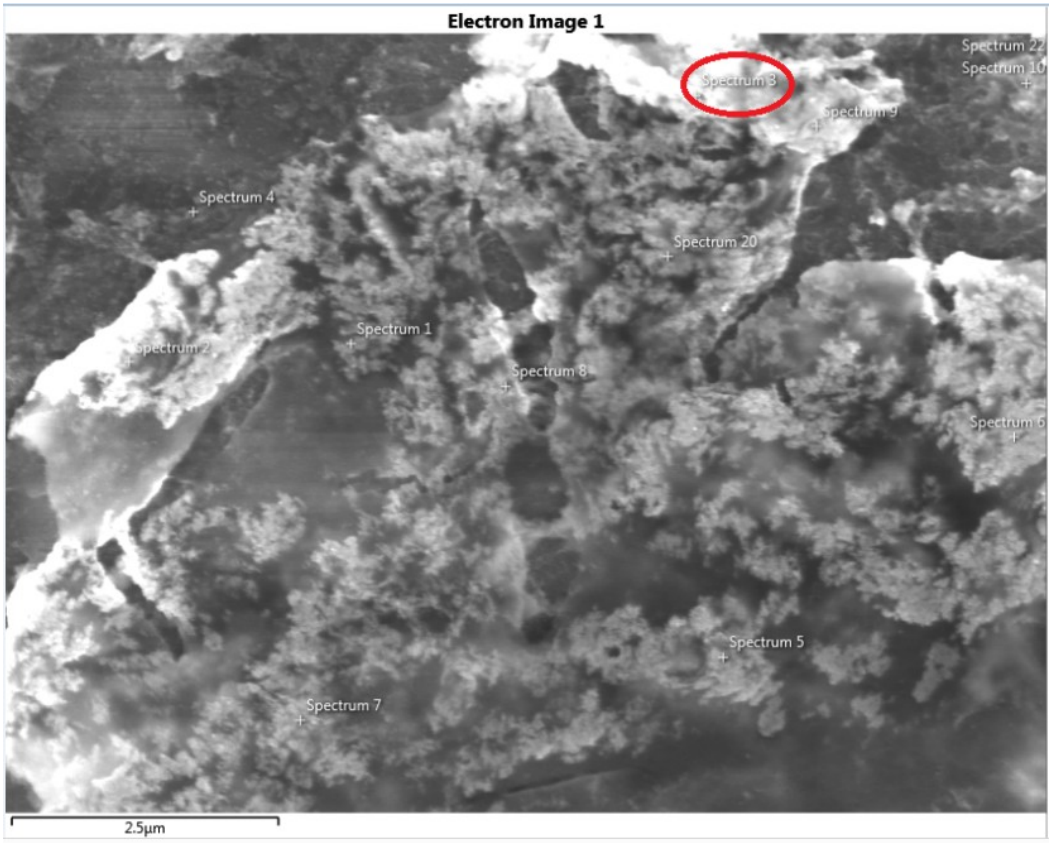

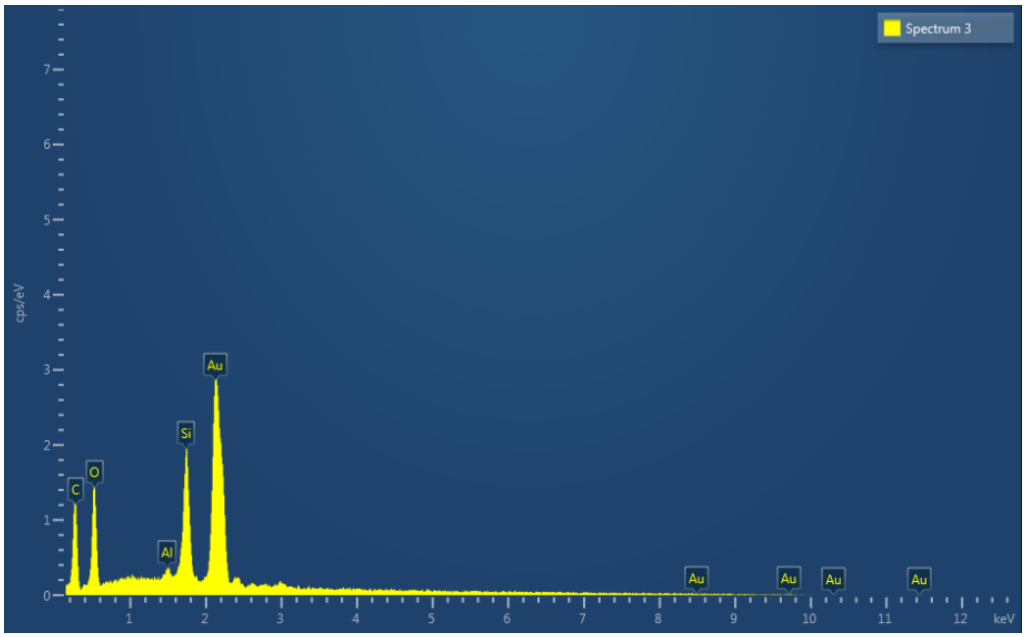


**Figure 4.12:** SEM-EDS analysis confirming the presence of gold on the specific segment (red circle) of a tapered fiber tweezed with synthesized GNRs.

In Figure 4.12, the carbon (C) is from the carbon tape, which was placed on an aluminum (Al) holder/stand used to hold the tapered fiber ($SiO_2$), and gold (Au) was present on the tapered fiber surface.

Figure 4.13 is an optical image taken using a cell phone camera to estimate the GNRs distribution over the tapered fiber surface. No expensive instrumentation, such as SEM, is needed to see the GNR rings along the tapered fiber as they are visible through the microscope (Figure 4.14).

Once the SERS substrate was fabricated, the next step was to adsorb a chemical on the prepared GNRs surface. We used Crystal violet (CV) as a probe molecule. A $10^{-3}$ M CV concentration stock solution was prepared and adsorbed on a tweezed fiber using

the “dip and dry” method described in **Chapter 2**. In this method, the tweezed fiber was perpendicularly dipped in the analyte drop (∽ 230 µl) placed on a coverslip. Ten more tweezed fibers were prepared, and CV from $10^{-4}$ M to $10^{-13}$ M concentrations were adsorbed on them. It was found that the minimum detectable limit for CV was $10^{-11}$ M (Figure 4.15). The three characteristic peaks of CV (highlighted in Figure 4.15) at 721.5 $cm^{-1}$, 1173 $cm^{-1}$, and 1613 $cm^{-1}$ correspond to the out-of-plane vibrations of ring C-H, in-plane vibrations of ring C-C stretching, respectively [6].

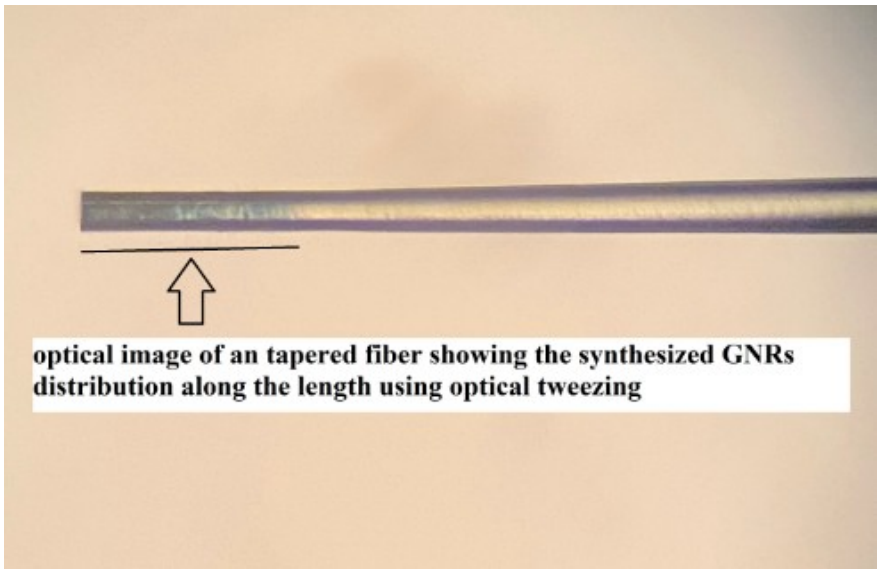


**Figure 4.13:** Optical image of a tapered fiber, which shows the distribution of synthesized GNRs along the length when tweezed using 1064 nm laser wavelength (taken using a phone camera).


**Figure 4.14:** Microscope set-up.

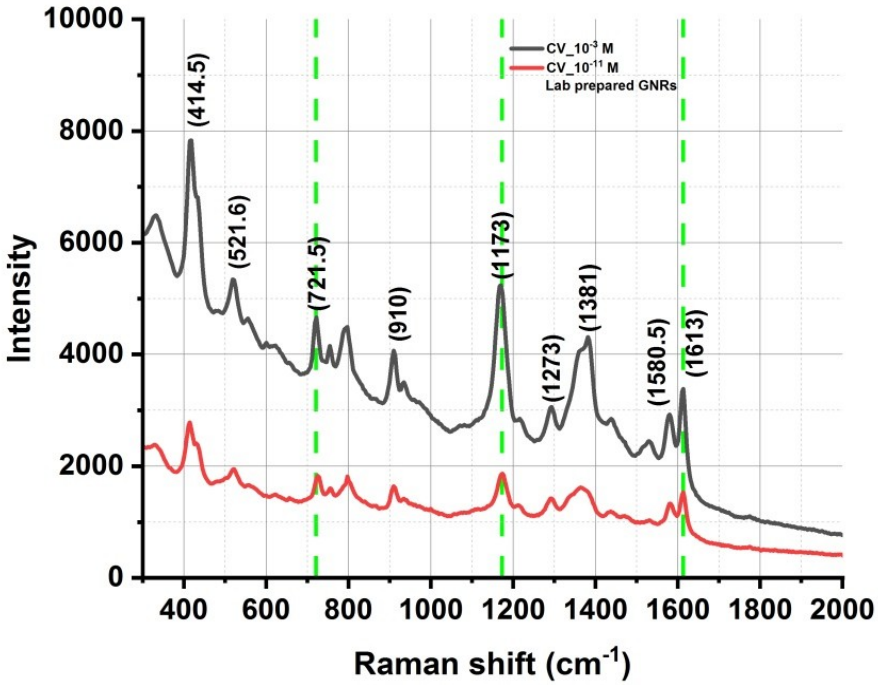


**Figure 4.15:** SERS spectra of CV comparing two concentrations ($10^{-3}$ M and $10^{-11}$ M).

Figure 4.16 compares lab-prepared GNRs and commercially available GNRs (Nanopartz). Compared to the others, Raman intensity was high with lab-synthesized GNRs, making this recipe desirable for preparing SERS substrates. The Raman spectrum was obtained for CV at $10^{-3}$ M concentration adsorbed on the tweezed fiber surface. The Raman analysis used a 785 nm excitation laser wavelength (10.5 mW). The integration time was 2000 ms with an average scan of 5. The spectrum was saved after three completed scans, resulting in a total exposure time of 30 seconds. All other experimental conditions were maintained unchanged.

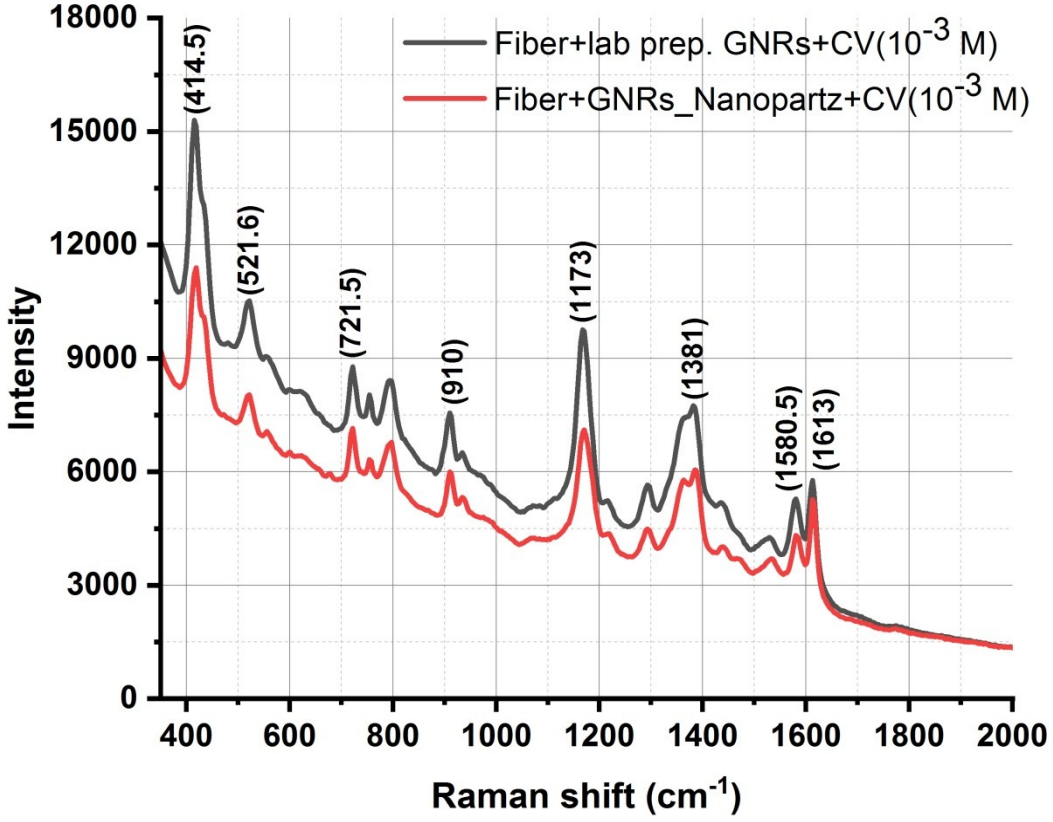


**Figure 4.16:** Raman spectra comparing lab-prepared and Nanopartz GNRs for CV at $10^{-3}$ M concentration.

Figure 4.17 presents the Raman data at two different locations (or diameters) named location 1 and location 2 along the tapered fiber length. Both spectrums were obtained from the same fiber. Location 1 is near the tip, where the diameter is small, and location 2 is higher. An important point is that the larger diameter has more GNRs and analyte distribution, resulting in a higher intensity count than the smaller diameter.

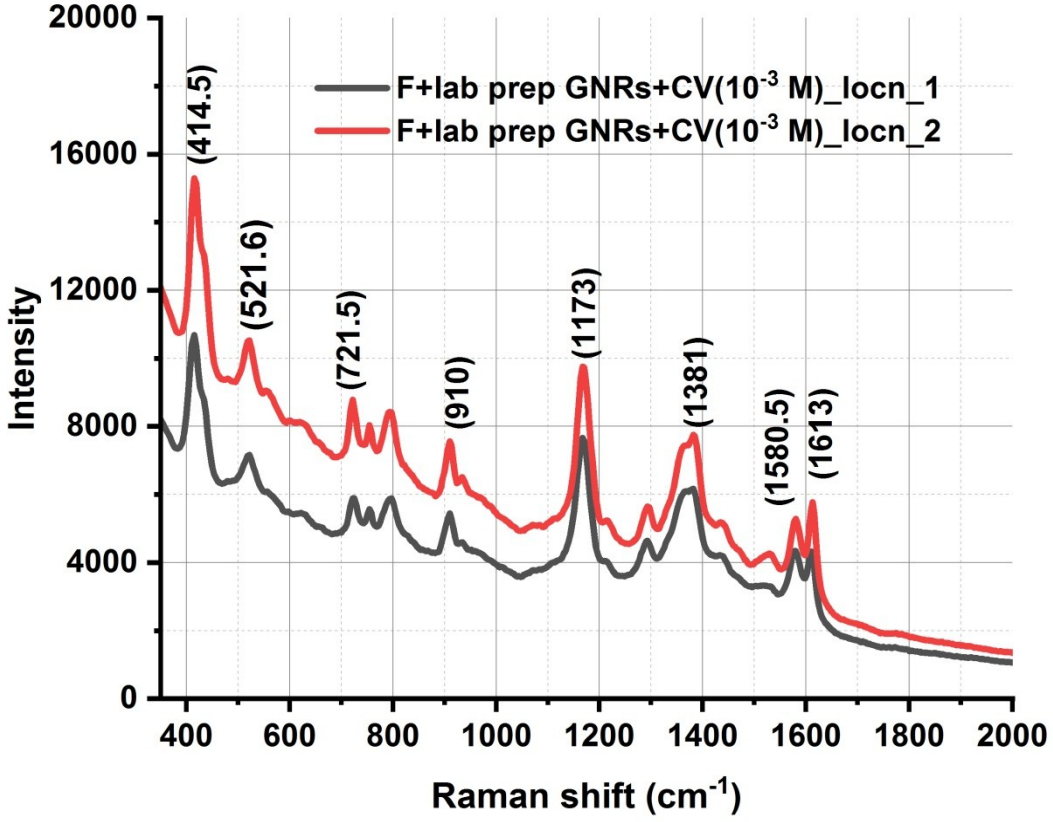


**Figure 4.17:** Comparing Raman spectra of two locations (locn_1 and locn_2) for the same fiber with $10^{-3}$ M concentration of CV.

## 4.8 Conclusion

In conclusion, the synthesis or one-pot method was used to prepare GNRs of smaller AR (3.6±0.6) with an LSPR wavelength of ∽ 785 nm. The role of each chemical was discussed in this chapter. The characterization of synthesized GNRs was done using a TEM and UV-visible spectrophotometer. The manufactured GNRs were used to develop the SERS substrate and obtain the Raman spectra of CV. The minimum detectable limit

for CV was determined to be $10^{-11}$ M, which shows a good sensitivity. Experimentally, the prepared GNRs showed a high-intensity count compared to the commercial GNRs. Overall, it can be said that more experimentation can be done to improve the uniformity of the GNRs in aqueous solution and to find out their stability or shelf life.

# Chapter 5

## Real-time detection

***This chapter*** *demonstrates the application of the developed SERS substrate (discussed in* ***Chapter 2****) in real-time detection. The detection limit (LoD) of the substrate was determined in two cases:* ***(a)*** *when bare tapered fiber was dipped in the GNRs + analyte solution and* ***(b)*** *when tweezed fiber was dipped in only the analyte solution. In both cases, scattered light was collected from the untapered end of the fiber. The advantages of real-time detection are - no pre-sample preparation is required where tweezing and detection can occur simultaneously in case (a), the opportunity for on-site detection, development of a hand-held system for remote sensing, immediate adjustments, and optimization is possible, leading to better control.*

## 5.1 Introduction

It is a well-known fact that the enhancement via both electromagnetic (EM) and chemical mechanisms needs the molecules to be in close proximity to the SERS substrate, which was reported to be approximately 1 – 10 nm [188]. Therefore, detecting trace quantities of molecules directly in a liquid is challenging. In recent decades, many optical fiber-based SERS sensors have been reported and investigated for trace detection in aqueous

solutions. In 1990, Vo-Dinh, T., and co-workers prepared an optical fiber-based SERS substrate. Two optical fibers were used - one for excitation and another for collection of the scattered light for in-situ detection. The limit of detection (LoD) for various compounds has been reported, such as terephthalic acid ($2.05*10^{-7}$ M) and benzoic acid ($1.80*10^{-6}$ M). This group showed the feasibility of an optical fiber-based SERS sensor for real-time detection in liquids [189]. Later, the same group reported a SERS fiber probe design in which a single fiber was used for the excitation and to collect the Raman signal. A thin silver layer was coated on a 1 cm length of the exposed core of the fiber [190]. The same research group reported the development of a SERS substrate where a fiber probe (single fiber for excitation and emission named SFEE) was developed by incorporating alumina nanoparticles and silver coatings on the optical fiber end. Two detection methods were followed: (i) dip and dry and (ii) in-situ detection using the prepared substrate. The LoD for Cresyl fast violet (CFV) in groundwater was determined to be 50 ppb ($1.5*10^{-10}$) [191]. To improve the sensitivity of the SERS substrate, a Ag nanoparticle film was deposited on an optical fiber tip using a photochemical modification process. The LoD for BPENB (1,4-bis[2-(4-pyridyl)ethenyl]-benzene was 1 nM [192]. Guo et al. demonstrated a photonic crystal fiber (PCF) based SERS sensor using silver nanoparticle colloids to detect and enhance the signal for the 4-mercaptobenzoic acid (4-MBA) molecules. AgNPs and analyte solution were injected into the air holes of the PCF using a syringe by the simple pressure set-up [193]. Similarly, in 2022, a solid-core PCF-based SERS sensor was reported where AgNPs were grown on the fiber walls using the silver mirror reaction, reducing silver ammonia solution with glucose [194].

Tapered fiber is advantageous for real-time detection as this structure allows the evanescent field to interact with the surrounding medium efficiently. In 2023, a tapered fiber sensor was reported to have a sensitivity of $10^{-6}$ M for detecting an aqueous solution of R6G. Silver nanoparticles were coated on the fiber to enhance the Raman signal using the magnetron sputtering coating method [195]. The heat and pulling method was used to obtain the tapered shape, and gold nanoparticles were deposited on the tapered surface using electrostatic self-assembly technology. The detection limit for R6G in an aqueous solution was determined to be $10^{-8}$ M [87]. A nonplanar repeated dewetting (npRDW) method was implemented to distribute gold nanoislands with < 10 nm nanogaps on the tapered fiber surface obtained using the heat and pull method. The developed sensor achieved the detection limit for aqueous R6G as low as $10^{-7}$ M. Sensitivity for both serotonin and dopamine in aqueous solutions was $10^{-5}$ M [196]. The same group, in 2024, reported a tunable solid-state dewetting process using a monolayer of Au nanoislands with different geometric structures that can be deposited on the tapered fiber surface. The LoD for R6G was as low as $10^{-7}$ M in an aqueous solution when the same optical fiber was used for excitation and collection of scattered light [197]. Also, a tapered fiber coated with silver nanoparticles using the immobilization process was designed. Two methods were used to detect CV: one was dip and dry, and another was real-time (named dip). In both cases, LoD was reported to be $10^{-9}$ M (0.018 ppb) [198]. Another SERS probe was reported where silver nanoplates were coated on the tapered surface of fiber using the hydrothermal process. The sensitivity of the prepared probe for 4-aminothiophenol (4-ATP) was $10^{-7}$ M [199]. The same group, after a year, reported an improved LoD of $10^{-9}$ M for 4-ATP, but the tapered fiber, in this case, was coated with silver nanopolyhedra

through an autoclave reaction process [200]. Another optical fiber probe was designed to detect levofloxacin lactate (an antibiotic widely used for bacterial infection treatment such as respiratory tract infections, bone and joint infections, etc.) in blood. The reported LoD for levofloxacin lactate was $10^{-4}$ M. Electrostatic self-assembly technology was used to deposit gold nanoparticles on the tapered surface [201]. In one study, the tapered fiber was obtained using the dipping and etching method. The reversed charged electrostatic attraction was used to attach different morphologies of nanostructures onto the fiber surface to make it functional for SERS. Gold nanospheres, silver nanocubes, gold nanorods, and gold and silver core-shell nanorods were used for this experiment. Regarding sensitivity, $10^{-8}$ M was achieved for methyl parathion (MP) in real-time detection [202]. Fabrication of a SERS probe based on tapered optical fiber, where its surface was modified using thiol groups so that in-situ nucleation and growth of silver nanoparticles could happen on the silica tapered surface, was reported. The $\backsim 10^{-11}$ M detection limit for 4-ATP was achieved using the prepared probe [203]. In 2021, a biosensor based on tapered optical fiber covered with AuNPs and zinc oxide nanoparticles has been proposed and explored for the detection of ascorbic acid (AA). AA is an essential compound in the human body, and its deficiency is closely related to the symptoms of diseases such as Alzheimer's, cardiovascular diseases, etc. The detection of AA in solution was obtained in the micromolar (μM) range. A plasma tapering technique was used for tapered fiber preparation, and salinization was used to adhere AuNPs to the OH group present on the fiber surface, which was hydrolyzed by keeping them in piranha solution (3:7v/v of H2O2:H2SO4) [204]. In 2023, Zheng, D., and co-workers fabricated a tapered fiber probe covered with gold nanoislands (NIs), which can

be used to detect neurotransmitters in the micromolar (μM) range. Zhengkun, W., and group proposed a tapered fiber-based SERS sensor enclosed in a capillary where AgNPs were coated using a chemical deposition method on the fiber surface. The lowest reported value for CV in aqueous solution was $10^{-7}$ M [205]. Other group reported the detection of 2 * $10^{-10}$ M for CV based on a tapered fiber probe. The developed SERS probe has ring patterned formed, which was achieved using stick-slip-motion assisted self assembly technique [206]. All the above-mentioned techniques are either expensive or need trained personnel for the fabrication of SERS substrates and to adsorb the analyte onto them.

These limitations led to us developing an efficient SERS probe in this work, where optical tweezing was used to deposit metallic nanostructure (gold nanorods) along the tapered fiber length using a laser. No other sophisticated instrumentation was required. The developed probe can work in two methods/schemes: (a) dip and dry (discussed earlier in this thesis) and (b) real-time detection (current chapter). The advantage of this probe in real-time detection is that one can perform tweezing and detection simultaneously using the excitation laser (785 nm laser wavelength), saving much time in depositing metallic nanostructures onto the fiber surface.

## 5.2 Methodology

The most crucial part of using the developed SERS substrate for real-time detection is the alignment in which the laser beam is focused on the fiber core. The same fiber was used for the excitation and collection of Raman scattered light. Figure 5.1 shows a schematic of the experimental set-up used for real-time detection using the fabricated probe. The

785 nm laser wavelength was focused on the multi-mode fiber (MMF) core's diameter of 110 µm. The light was focused on the prepared flat end of the fiber, whereas the tapered end was dipped in the analyte solution where the evanescent field would interact with the surroundings. A fiber chuck held the fiber straight and connected with an x-y axis stage, and a translational stage was used for the precise movement of the fiber in the z-direction. A cylindrical holder held the analyte solution with capacity of ∽ 65 µl.

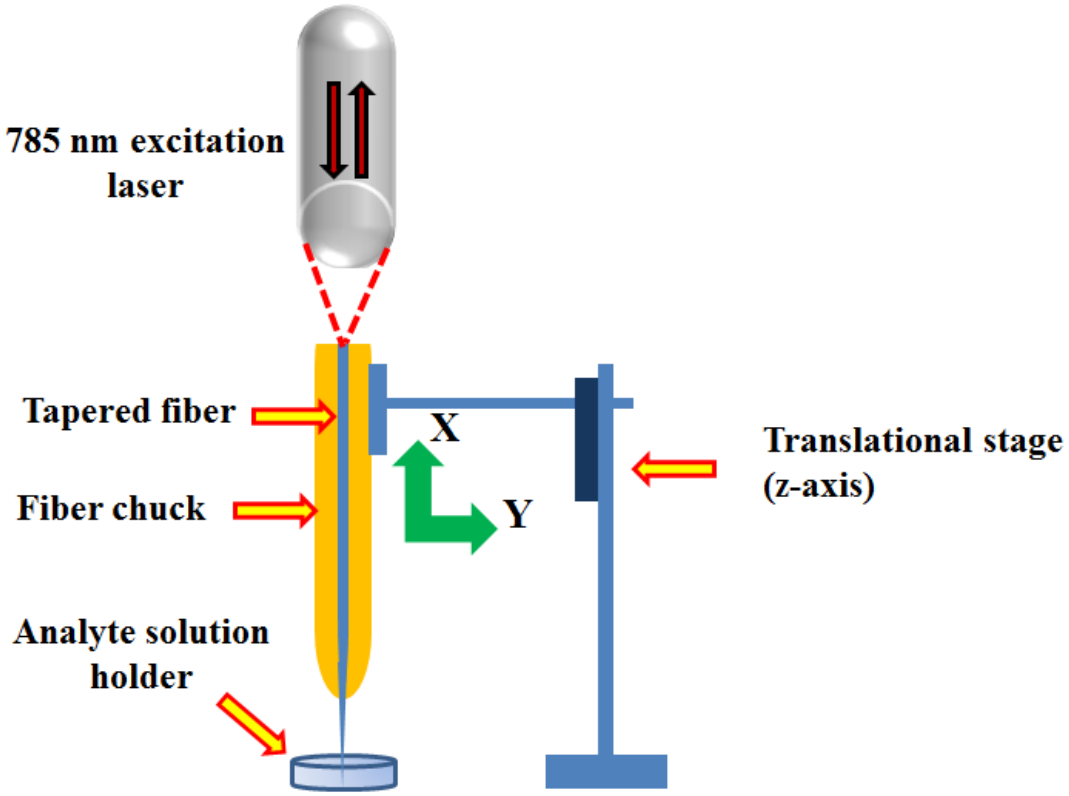


**Figure 5.1:** Experimental set-up for real-time detection.

## 5.3 Results and Discussion

As was mentioned earlier, alignment is of the utmost importance in this set-up. To verify the alignment, an experiment in which the Raman spectrum was obtained when the flat end of the fiber was dipped in R6G powder (a chunk of R6G) was performed. All the distinguished peaks were observed for R6G at threshold current (0.38 mA), and the intensity count increased on increasing the current to 0.4 mA, as shown in Figure 5.2. This shows the successful alignment of the laser beam to the fiber core.

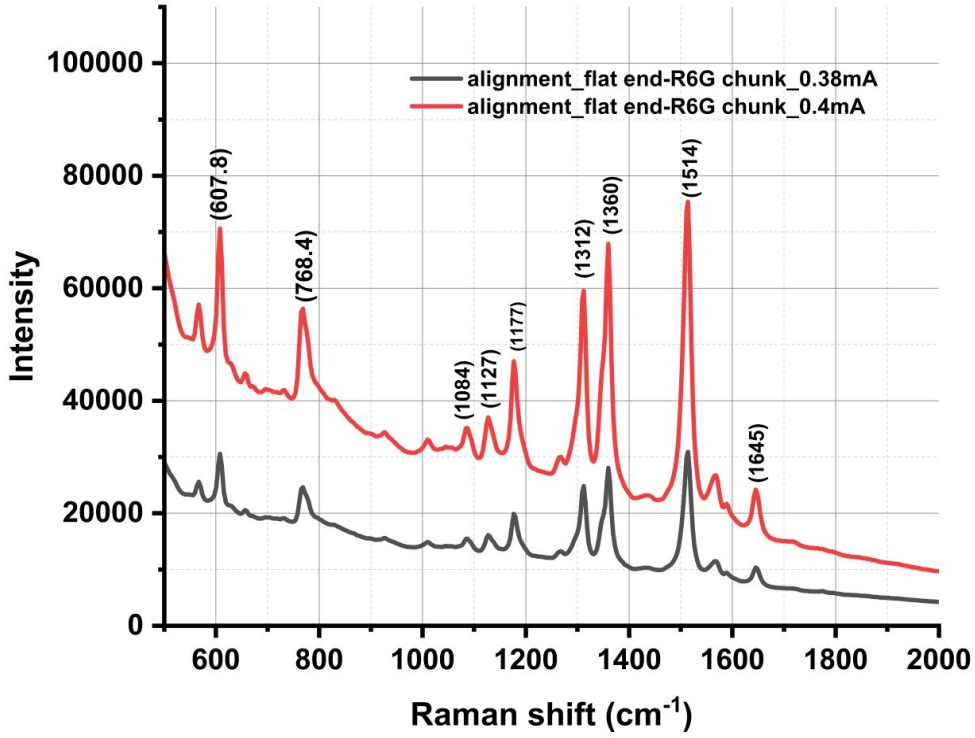


**Figure 5.2:** Raman spectra from R6G powder using flat-end fiber for alignment check.

Two cases were studied for detection using real-time analysis: (a) when bare tapered fiber was dipped in the GNRs + analyte solution, and (b) when tweezed fiber was

dipped in the analyte solution. The drop size for the analyte solution in both cases was 65 µl. In case (a), an etched tapered fiber was dipped in gold nanorods and an analyte solution of a particular concentration (e.g., $1*10^{-1}$ M). During the measurements, laser light is focused on the flat end of the optical fiber. Laser transmitted through the fiber core along the tapered length interacts with the GNRs and analyte molecules. Due to the LSPR property of the GNRs, the SERS signal was enhanced and transmitted back to the Raman spectrometer using the same fiber. Figure 5.3 compares Raman spectra from $10^{-3}$ M to $10^{-7}$ M of R6G and GNRs solution showing Raman peaks for R6G. The intensity count decreased with decreasing concentration. The sensitivity of this novel substrate was determined to be $10^{-7}$ M for R6G via the above-described method.

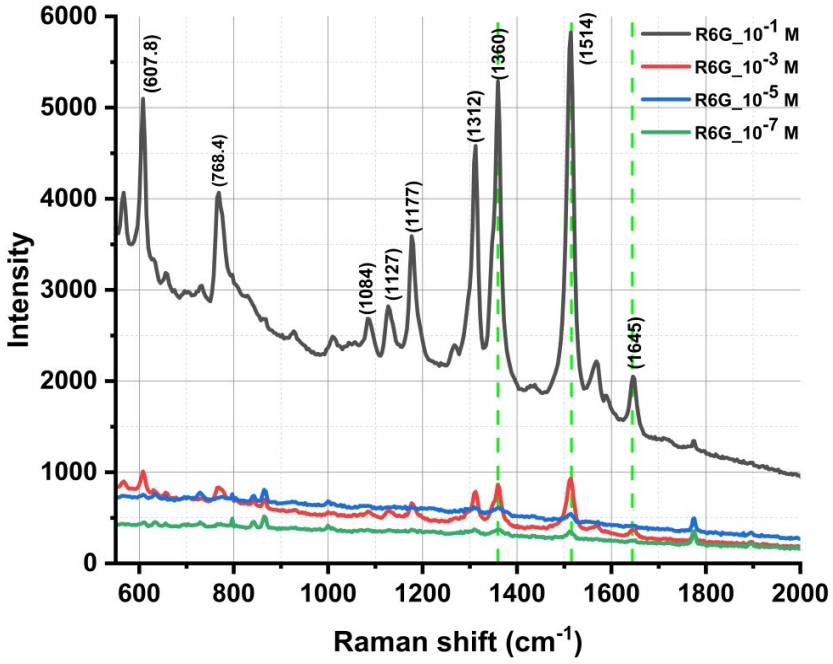


**Figure 5.3:** Comparing Raman spectra of different concentrations ($10^{-1}$ M to $10^{-7}$ M) of R6G in GNRs solution using bare fiber for real-time detection.

In case (b), a tapered fiber was first tweezed with GNRs using the optical tweezing method described previously and then dipped in the analyte + water (nanopure water) solution of a specific concentration. The SERS performance was analyzed using this method, and a minimum detectable limit of $10^{-7}$ M was observed for R6G (Figure 5.4). The three characteristic peaks for R6G were compared in both cases: 1360 $cm^{-1}$, 1514 $cm^{-1}$, and 1645 $cm^{-1}$.

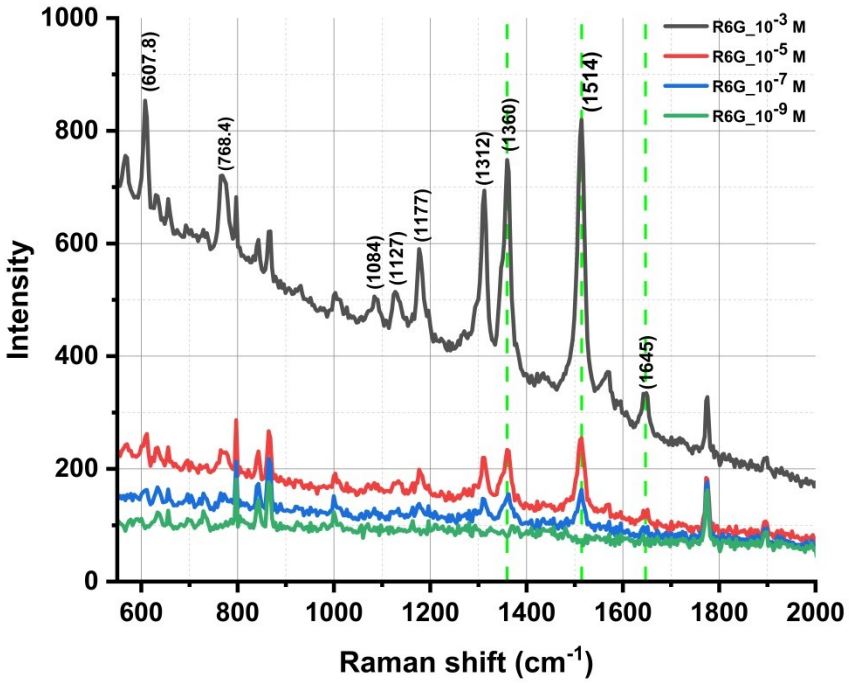


**Figure 5.4:** Comparing Raman spectra of different concentrations ($10^{-3}$ M to $10^{-9}$ M) of R6G in water solution using tweezed fiber for real-time detection.

The same experiment was repeated with CV to determine the LoD in real time. Figures 5.5 and 5.6 show the Raman spectra for two cases: bare fiber dipped in GNRs, and CV solution and tapered fiber dipped in CV solution, respectively. In both cases, the lowest concentration of CV detected was $10^{-8}$ M.

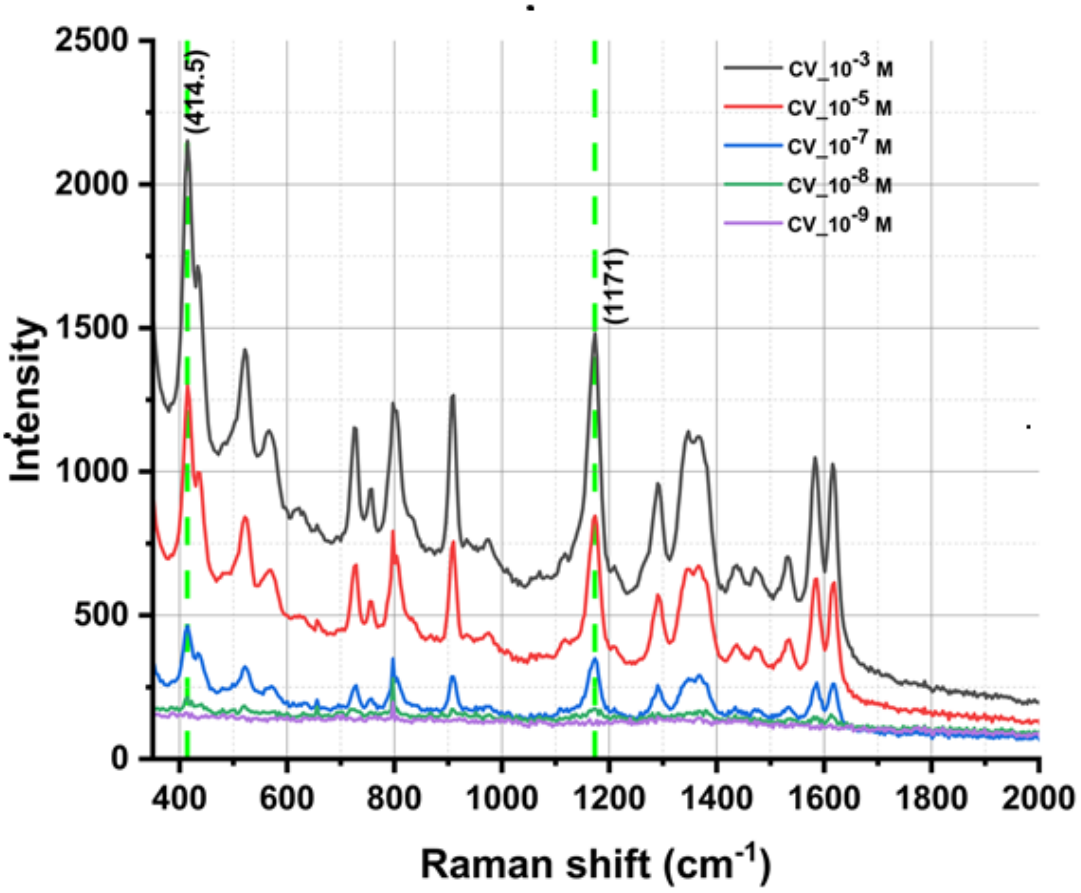


**Figure 5.5:** Comparing Raman spectra of different concentrations ($10^{-3}$ M to $10^{-9}$ M) of CV in GNRs solution using bare fiber for real-time detection.

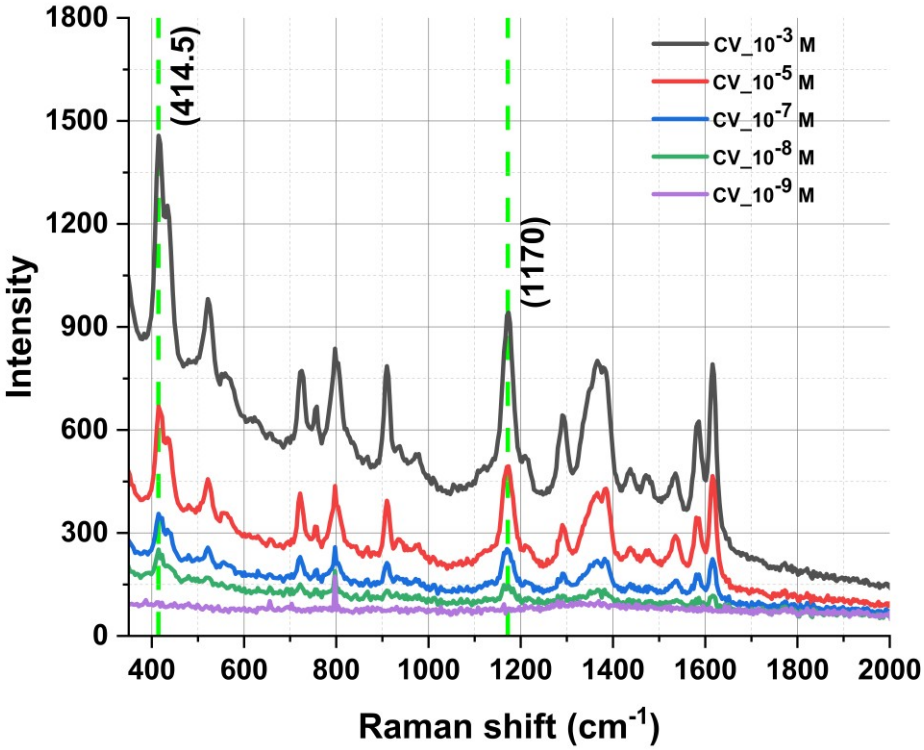


**Figure 5.6:** Comparing Raman spectra of different concentrations ($10^{-3}$ M to $10^{-9}$ M) of CV in water solution using tweezed fiber for real-time detection.

## 5.4 Conclusion

A novel SERS substrate has been developed for real-time detection of chemicals at low concentrations. This study focused on two cases of in-situ detection. One is when the etched fiber is dipped in the analyte + GNRs solution, where the detection and deposition of GNRs occur simultaneously. Another was when already tweezed fiber was dipped in analyte and water solution. In both cases, $10^{-7}$ M LoD was determined for rhodamine 6G and $10^{-8}$ M for CV, which represents a reasonably good detection limit measured directly

in liquid using the through-fiber detection method, as many researchers have not achieved this value of sensitivity until this date for in-situ optical-fiber based sensors. This real-time detection is advantageous using the developed substrate as no instrument other than a laser is required for the deposition and detection of metallic nanoparticles. Also, the rapid detection using the developed set-up eliminates the time-consuming procedures necessary to collect Raman signals.

# Chapter 6

# Potential Applications of the developed SERS substrate

*The development of rapid, non-destructive chemical analysis methods is of great interest in the scientific world. An optical fiber-based sensor to detect chemicals either in dry or liquid state using surface-enhanced Raman spectroscopy has been developed. The fabrication process of the SERS substrate is quick, does not require significant sample preparation, can be used in both a liquid and dry state of the analyte, and is cost-effective.* ***This chapter demonstrates*** *the detection of chemicals using the developed probe, which has enormous significance in agriculture, such as Glyphosate and Xanthohumol. The results presented are based on the dip and dry method.*

## 6.1 Introduction

Glyphosate (N-(phosphonomethyl) glycine) – a herbicide widely used for weed control worldwide. If Glyphosate is not managed adequately in fields, the residues can stay in plants, soil, and groundwater. It was reported that residues remain in the soil for over a year. Van Bruggen and co-workers have discussed the harmful effect of Glyphosate on plants, micro-organisms, and human health [207]. Glyphosate harms female fertility [208]

and the growth of breast cancer in women [209]. Therefore, monitoring and detection are critical from an environmental and health point of view. In 2022, Mikac, L. et al. reported $10^{-4}$ M sensitivity for Glyphosate using SERS substrate based on AuNPs when 785 nm laser excitation wavelength was used [210]. In 2024, the SERS technique reported a LoD of 2 ppb for Glyphosate [211]. In literature, many optical fiber-based sensors have been reported for Glyphosate detection with detection limits of 3.2 mg/L [212], 0.11 mg/L [213], 0.04 μg/L [214], 0.54 mg/L [215].

Xanthohumol (XN) is a natural flavonoid in female hops flowers, also called cones from hops plants, which are extensively used in the brewery industry. Xanthohumol is responsible for the taste and bitterness of beer. The pharmacological properties and their effect on humans have been studied in detail [216]. In literature, data on hops based on Raman spectroscopy or SERS is rare. As compared to expensive and lengthy analysis methods such as HPLC, GC, and mass spectroscopy (MS), SERS is an alternate method that provides fast detection, no pre-sample treatment is required, is portable, and cost-effective [217].

## 6.2 Methodology

Both Glyphosate and Xanthohumol are insoluble in water. Raman peaks were not shown by these two chemicals when they were mixed in water, which confirmed that no analyte was present on the fiber probe. Glyphosate precipitates in addition to water, and Xanthohumol is a sticky substance that does not dissolve in water. When mixed in ethanol, the chemicals were adsorbed onto the fiber surface using the dip and dry. For

each concentration, twelve locations on the tapered fiber were explored, and it was confirmed through Raman intensity that the analyte is adsorbed uniformly around a particular diameter. The experimental method was described in **Chapter 2,** where a schematic of the fiber is shown. For Raman results, the spectra shown in Figures 1 and 2 are from location 7 (210 μm away from the tip), where the maximum intensity of the Raman signal was achieved. A spectrometer from Ocean Optics[5] and excitation wavelength 785 nm (10.5 mW) collected Raman data from the analyte adsorbed on SERS substrate. The integration time was 2000 ms with five average scans, and each spectrum was saved after the completion of three scans. The total exposure time for detection was 30 seconds.

## 6.3 Raman spectroscopy results and discussion

Figures 6.1 (a) and 6.2 (a) show the chemical structures of Glyphosate and Xanthohumol. Both chemicals were purchased from Sigma Aldrich, Canada. Figures 6.1 (b) and 6.2 (b) compare the Raman spectra at different concentrations of Glyphosate and Xanthohumol. The obtained Raman peaks match the theoretical data [217-220]. Studies have found that Glyphosate degrades into Aminomethylphosphonic Acid (AMPA) when it comes in contact with metals [218]. The minimum detectable limit for Glyphosate was $10^{-3}$ M (Figure 6.1 (b)). The Raman bands for Glyphosate at 1265 $cm^{-1}$ and 1450 $cm^{-1}$

[5] Ocean Insight, QE Pro Raman Series

correspond to the bending of CH + bending of OH bonds [219], and stretching of CC + bending of CNH + twisting of $NH_2$ bonds, respectively [218].

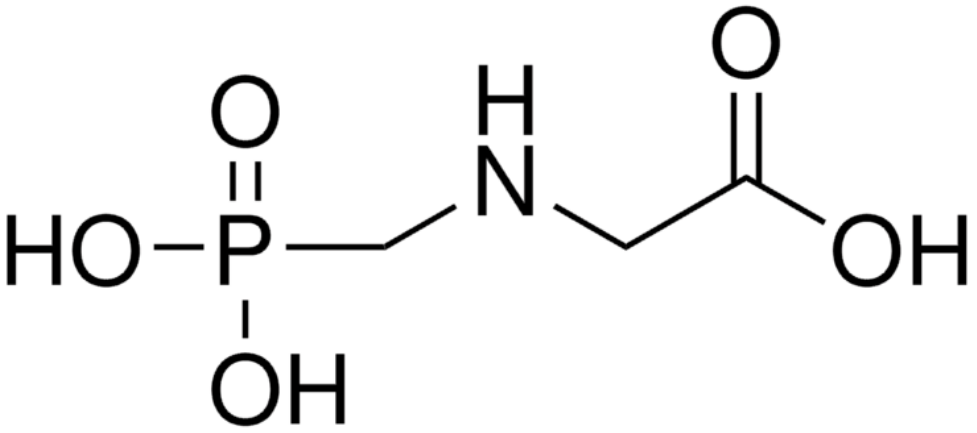


(a)

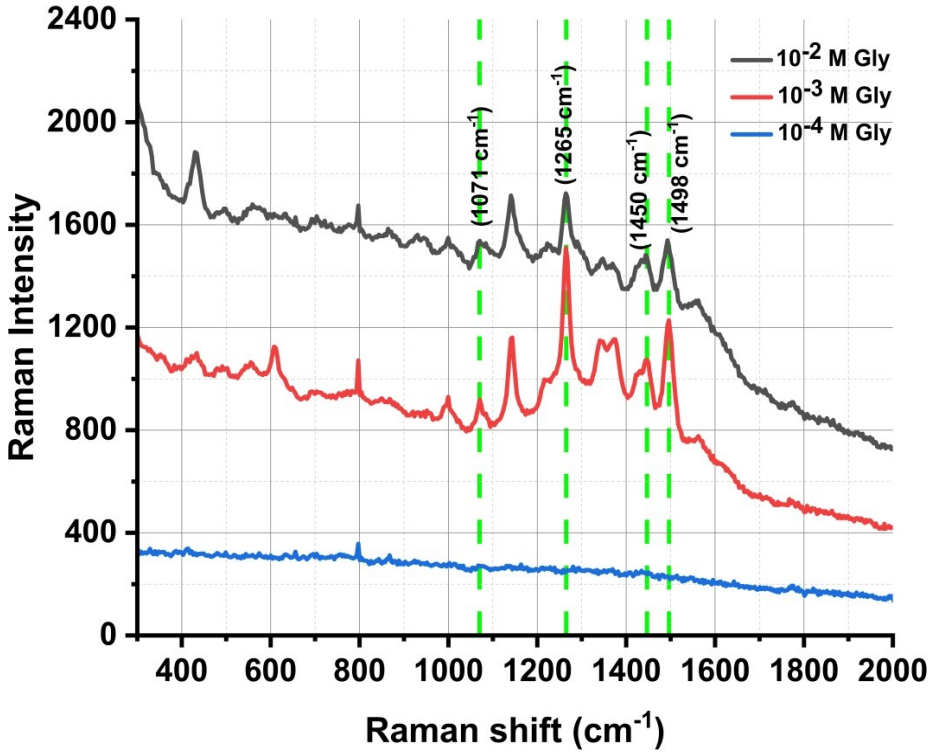


(b)

**Figure 6.1:** (a) Molecular structure of Glyphosate (Sigma Aldrich, Canada), and (b) Raman spectra comparing different concentrations ($10^{-2}$ M to $10^{-4}$ M) of Glyphosate mixed in ethanol.

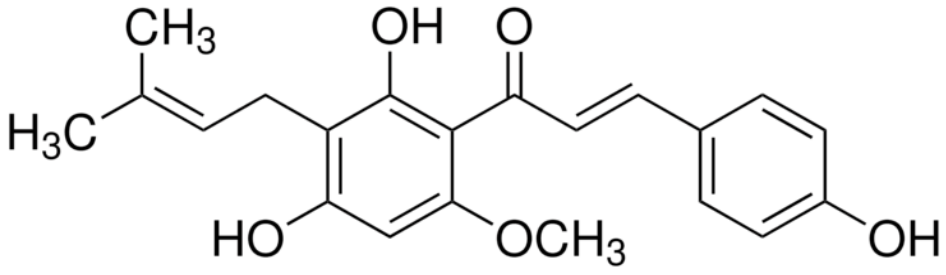


(a)

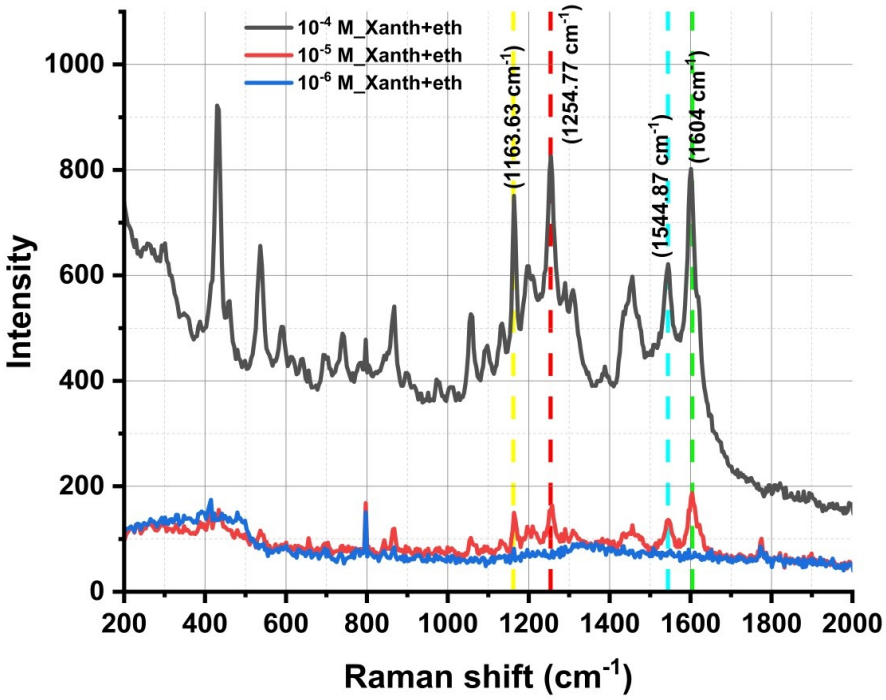


(b)

**Figure 6.2:** (a) Molecular structure of Xanthohumol (Sigma Aldrich, Canada), and (b) Raman spectra comparing different concentrations ($10^{-4}$ M to $10^{-6}$ M) of Xanthohumol mixed in ethanol.

Figure 6.3 represents the uniform distribution of an analyte (Xanthohumol: $10^{-4}$ M conc.) at five different angular positions at a particular diameter (location 7) on the tapered fiber probe. Until today, not much Raman data is available for Xanthohumol, which allows for the exploration and development of a database for the chemicals present in hops plants using the prepared SERS substrate.

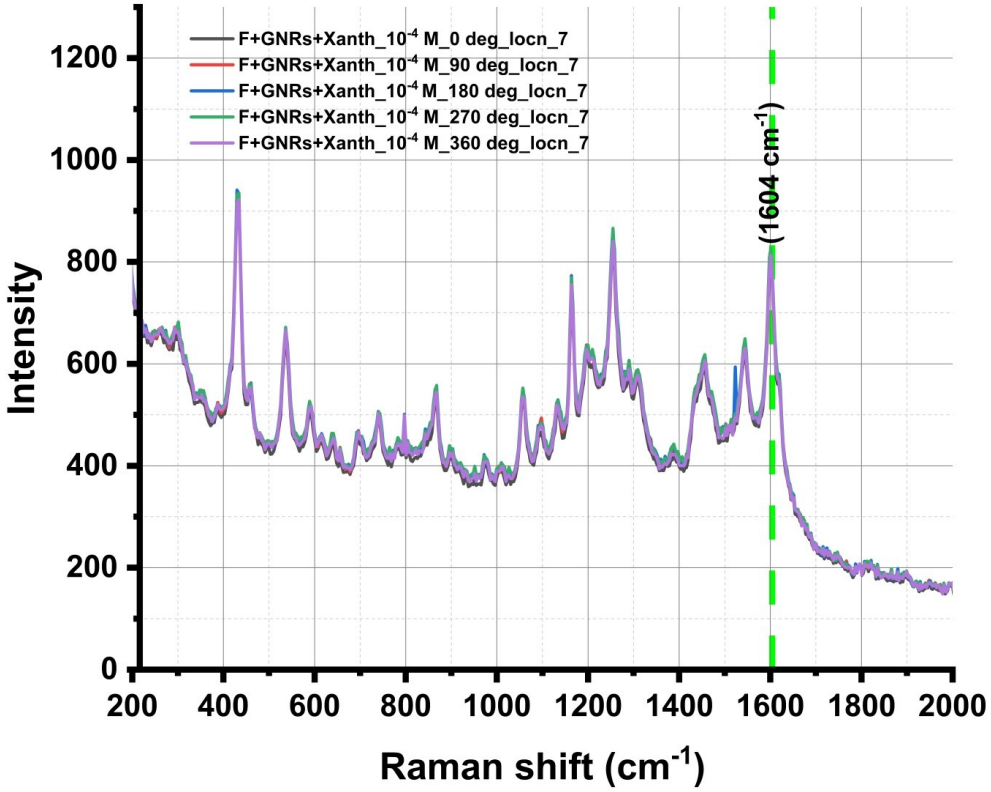


**Figure 6.3:** Raman spectra represent the uniformity in intensity at five angular positions of location 7.

To proceed with the real-time detection of chemicals from hops plants, three types of hops plants, Cascade, Brewer's gold, and Willamette hops, were cultivated and grown at Lakehead University Agricultural Research Station (LUARS). Figure 6.4 shows a picture of the hops plants grown at LUARS. A leaf from the flower was taken carefully using a pair of tweezers. Most of the raisins were accumulated at one end of the leaf. Figures 6.5 (a), (b), and (c) show the enlarged image of the hop flower, a leaf from the flower, and an optical image of the raisins, which contain essential chemicals, taken using the camera.

To begin with the analysis, a leaf was placed directly under the laser, and the raisins were focused upon (Figure 6.5 (c) to obtain the Raman spectrum. Figure 6.6 are the Raman spectra for Cascade, Brewer's gold, and Willamette hops flowers. The 785 nm (0.48 mA) laser excitation wavelength was used with five average scans and 5 second integration time. Each scan was saved after three completed scans, giving a total exposure time of 75 seconds.

This experiment was performed to check whether the peaks for Xanthohumol from a pure sample bought from Sigma Aldrich using SERS substrate would match the peaks from the homegrown hops plants directly placed underneath the laser beam. The Raman bands obtained from the leaf are 1443 $cm^{-1}$, 1553 $cm^{-1}$, 1604 $cm^{-1}$, and 1624 $cm^{-1}$, which are the peaks for Xanthohumol, Cohumulone, and Colupulone. The strong Raman band at 1604 $cm^{-1}$ for Xanthohumol is present in commercially available standard samples and from hops leaves. In the future, chemicals can be extracted from homegrown hops plants using different techniques [221]. The extracted chemicals can either be adsorbed onto the tweezed optical fiber, or real-time experiments using this sensor can be

performed to achieve high sensitivity. A database can be developed as barely any work has been done in this field.

**Figure 6.4:** Image of the hops plant at LUARS.

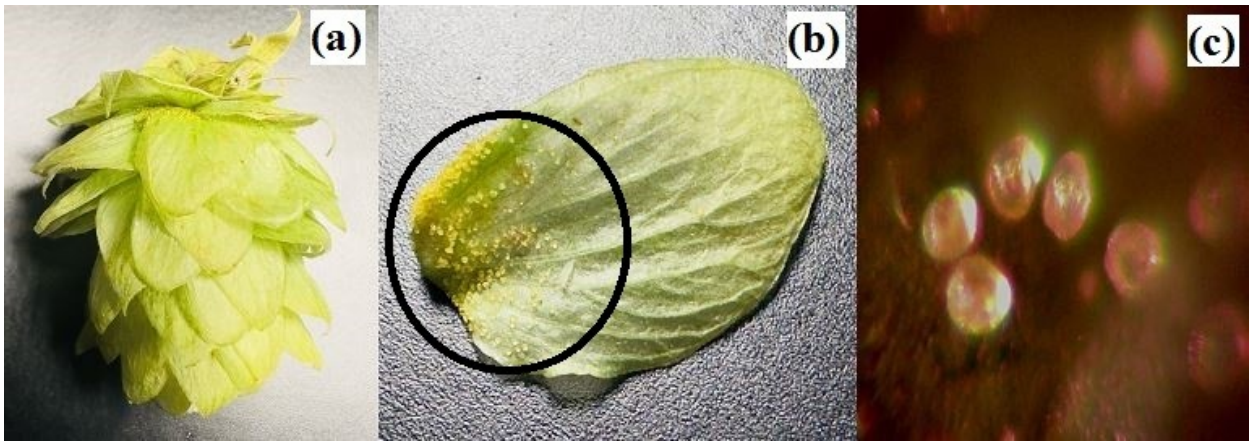


**Figure 6.5:** Image of (a) hops flower, (b) leaf, and (c) raisins present on the leaf.

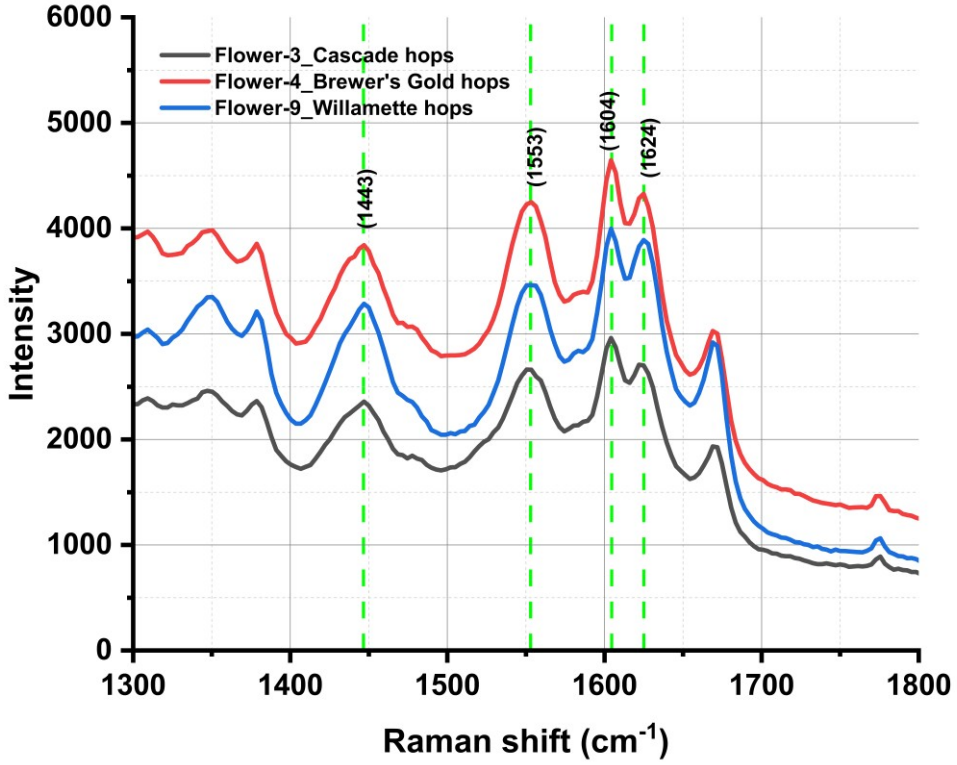


**Figure 6.6:** Raman spectra showing peaks for three different types of hops plants.

## 6.4 Conclusion

In conclusion, the developed SERS probe was tested for two critical chemicals in the agriculture and brewery industry: Glyphosate and Xanthohumol. Mixing these chemicals with ethanol and adsorbing them on the fiber substrate using dip and dry method, the minimum detectable limit for Glyphosate and Xanthohumol was determined to be $10^{-3}$ M and $10^{-5}$ M, respectively.

Also, a reference spectrum was obtained directly from the leaves of the cultivated hops plants, which can be utilized in further experiments.

# Chapter 7

## Conclusion and Future Work

In the thesis, a highly sensitive and versatile optical fiber-based SERS substrate, which we call the SERS probe for detecting trace chemicals using surface-enhanced Raman spectroscopy (SERS) has been developed.

The tapered shape of the fiber was achieved using a chemical etching method. The details on the deposition of gold nanorods (GNRs, Nanopartz, USA) along the fiber length are discussed thoroughly using an optical tweezing (OT) method. The Raman spectra based on the nanometer (nm) sized tips were presented where the tapered surface was divided into three regions based on GNR s distribution: tip (~100 nm – 16 μm) region, middle (16 μm – 30 μm) region, and end (30 μm – 45 μm) region. The reported sensitivity of the probe was $10^{-7}$ M for rhodamine 6G (R6G). The nm size of the tip is breakable; therefore, to make the fiber probe more robust, a ∽ 35 μm tip was designed. Also, step-to-step details on developing a mechanical system were presented, which was used to collect the Raman scattered light more efficiently. All the improved results are described in **Chapter 2** (section 2.8), where sensitivity was significantly enhanced to Pico molar (pM) level for both R6G and another dye, crystal violet (CV). Due to their

properties, R6G and CV are dyes used in food and aqua farming but are not approved by the Food and Drug Administration (FDA).

Two more essential chemicals: Glyphosate, a herbicide that is widely used for weed control in agriculture fields all over the globe, and Xanthohumol (XN), a flavonoid present in hops plants that are commonly used in the brewery industry as it is responsible for bitterness and aroma in beers were detected using the SERS substrate. The unique features of the substrate were discussed, which shows that the prepared SERS substrate is reproducible, stable, cost-effective, versatile, and can act as a three-dimensional tool in various fields such as food safety, agriculture, environmental monitoring, etc. A "dip and dry" method was used to adsorb the analyte molecules on the tapered fiber surface, which has applications in terms of uniform distribution of analyte around a specific diameter of the tapered fiber to make it a 3D sensor. The optimum laser wavelength, power for optical tweezing, excitation laser wavelength, and power to enhance the device's sensitivity were achieved. To characterize the probe before and after tweezing, a scanning electron microscope (SEM) and a traditional microscope have been used extensively to observe each minute detail.

The gold nanorods of AR 3.6±0.6 using the seedless synthesis method were prepared in the lab. The synthesized GNRs have LSPR ∽ 785 nm, closer to the excitation laser wavelength. These GNRs were tweezed successfully on the tapered fiber surface, keeping the shape of the GNRs intact, which was examined using SEM. A transmission electron microscope (TEM) and UV-visible spectrophotometer were used to characterize the GNRs. The SERS substrate developed using these GNRs showed a good sensitivity of $10^{-11}$ M for CV (**Chapter 4**).

A SERS substrate based on zinc (Zn) and zinc oxide (ZnO) was developed using OT. GNRs and Zn and ZnO nanostructures were deposited along the tapered fiber surface, forming rings to prepare this. **Chapter 3** describes the step-to-step demonstration of the preparation process, characterizations, and the effect of single and double tweezing conditions on the distribution of the rings. The fabricated ZnO-based SERS substrate will have applications in the development of biosensors.

Besides the dip and dry scheme, the developed probe can detect chemicals in real time (**Chapter 5**). A set-up was designed to control the experiment precisely during detection to achieve maximum sensitivity. Two cases were studied: (a) when bare fiber was dipped in GNRs and analyte solution, and (b) when tweezed fiber was immersed in analyte solution. In both cases, the detection limit was determined to be $10^{-7}$ M for R6G and $10^{-8}$ M for CV, respectively, which is a significant number when detecting an analyte directly in liquid. The experimental set-up was designed to focus the laser beam on the fiber's core, and the same fiber was used for the excitation and collection of the scattered Raman signal. This method is rapid, saves time for the deposition of metallic particles, and allows adjustments while experimenting to achieve optimum sensitivity. These contributions will lead to commercial applications as the developed sensor has high sensitivity, can work in both dry and liquid states of the analyte, and is reproducible, stable, and cost-effective.

In the future, comparable ZnO nanostructures and GNRs can be synthesized to fabricate a SERS substrate, which will have potential applications in biosensing as ZnO is biocompatible. Functionalization of prepared GNRs can be used with living cells, making this probe more suitable in biomedicine. Also, there is an urgent need to develop a

Raman database to know and understand the chemicals present in hops flowers, which can be achieved using the developed fiber-based SERS substrate.

# References


**[1]** **K. C. Kao and G. A. Hockman, "Dielectric-fibre surface waveguides for optical frequencies," 113 ed 1966, pp. 1151-1158.**

**[2]** **G. Keiser, "Optical Fiber Communications," 3 ed. Boston, MA: McGraw Hill, 2000.**

**[3]** **R. P. Khare, "Fiber Optics and Optoelectronics," 2004.**

**[4]** **X. D. Wang and O. S. Wolfbeis, "Fiber-Optic Chemical Sensors and Biosensors (2015-2019)," *Analytical Chemistry*, Vol. 92, no. 1, pp. 397-430, 2020.**

**[5]** **S. Ben-Jaber, W. J. Peveler, R. Quesada-Cabrera, C. W. O. Sol, I. Papakonstaninou, and I. P. Parkin, "Sensitive and specific detection of explosives in solution and vapour by surface-enhanced Raman spectroscopy on silver nanocubes," *Royal Society of Chemistry*, Vol. 9, no. 42, pp. 16459-16466, 2017.**

**[6]** **X. Chen, T. H. D. Nguyen, L. Gu, M. Lin, "Use of Standing Gold Nanorods for Detection of Malachite Green and Crystal Violet in Fish by SERS," *Journal of Food Science*, Vol. 82, no. 7, pp. 1640-1646, 2017.**

**[7]** **Y. Tian, W. Wang, N. Wu, X. Zou, and X. Wang, "Tapered Optical Fiber Sensor for Label-Free Detection of Biomolecules," *Sensors*, Vol 11, no. 4, pp. 3780-3790, 2011.**

**[8]** **R. K. Gangwar, A.K. Pathak, F. Chiavaioli, M. H. Abu Bakar, Y. M. Kamil, M. A. Mahdi, and V. K. Singh, "Optical fiber SERS sensors: Unveiling advances, challenges, and applications in a miniaturized technology," *Coordination Chemistry Reviews*, Vol. 510, no. 16459, pp. 1-31, 2024.**

**[9]** **Z. Liu, C. Guo, J. Yang, and L. Yuan, "Tapered fiber optical tweezers for microscopic particle trapping: fabrication and application," *Optics Express*, Vol. 14, no. 25, pp. 12510-12516, 2006.**

**[10]** **Z. Rosenzweig and R. Kopelman, "Analytical Properties and Sensor Size Effects of a Micrometer-Sized Optical Fiber Glucose Biosensors," *Analytical Chemistry*, Vol. 68, no. 8, pp. 1408-1413, 1996.**

**[11]** **A. J. Haes and R. P. Van Duyne, "A Highly Sensitive and Selective Surface-Enhanced Nanobiosensor," *MRS Online Proceedings*, Vol. 723, 2002.**

**[12]** **A. Lazarev, N. Fang, Q. Luo, and X. Zhang, "Formation of fine near-field scanning optical microscopy tips. Part I. By static and dynamic chemical etching," *Review of Scientific Instruments*, Vol. 74, pp. 3679-3683, 2003.**

**[13]** **A. Leung, P. M. Shankar, and R. Mutharasan, "A review of fiber-optic biosensors," *Sensors and Actuators B: Chemical*, Vol. 125, no. 2, pp. 688-703, 2007.**

**[14]** **H. Nikbakht, H. Latifi, M. Oraie, and T. Amini, "Fabrication of Tapered Tip Fibers With a Controllable Cone Angle Using Dynamical Etching," *Journal of Lightwave Technology*, Vol. 33, no. 23, pp. 4707-4711, 2015.**

**[15]** **J. O. Trevisanutto, A. Linhananta, and G. Das, "Plasmonic structure: fiber grating formed by gold nanorods on a tapered fiber," *Optics Express*, Vol. 41, no. 24, pp. 5789-5792, 2006.**

**[16]** **N. Kaur, "Tweezing and Manipulating Nanomaterials on Tapered Optical Fiber to Develop SurfaceEnhanced Raman Spectroscopy (SERS) Substrate," *Master's Thesis, Lakehead University,* pp. 1-88, 2020.**

**[17]** **B. R. Puri, L. R. Sharma, and M. S. Pathania, "Principles of Physical Chemistry," 37 ed. 1998.**

**[18]** **S. A. Ogundare and W. E. van Zyl, "A review of cellulose-based substrates for SERS: fundamentals, design principles, applications," *Cellulose*, Vol. 26, no. 11, pp. 6489-6528, 2019.**

**[19]** **D.N. Sathyanarayana, "Vibrational Spectroscopy: Theory and Applications," 1st ed 2004.**

**[20]** **D. W. Hahn, "Report: Raman Scattering Theory," 2007.**

**[21]** **M. Fleischmann, P. J. Hendra, and A. J. McQuillan, "Raman spectra of pyridine adsorbed at a silver electrode," *Chemical Physics Letters*, Vol. 26, no. 2, pp. 163-166, 1974.**

**[22]** **D. L. Jeanmaire, and R.P. Van Duyne, "Surface Raman Spectroelectrochemistry: Part I. Heterocyclic, Aromatic, and Aliphatic Amines Adsorbed on the Anodized Silver Electrode," *Journal of Electroanalytical Chemistry and Interfacial Electrochemistry*, Vol. 84, no. 1, pp. 1-20, 1977.**

**[23]** **M. G. Albrecht and J. A. Creighton, "Anomalously intense Raman spectra of pyridine at a silver electrode," *Journal of the American Chemical Society*, Vol. 99, no. 15, pp. 5215-5217, 1977.**

**[24]** **M. Moskovits, "Surface roughness and the enhanced intensity of Raman scattering by molecules adsorbed on metals," *Journal of Chemical Physics*, Vol. 69, no. 9, pp. 4159-4161, 1978.**

**[25]** **M. Moskovits, "Surface-Enhanced Spectroscopy," *Review of Modern Physics*, Vol. 57, no. 3, pp. 783-826, 1985.**

**[26]** **K. Kneipp, H. Kneipp, I. Itzkan, R. R. Dasari, and M. S. Feld, "Surface-enhanced Raman scattering and biophysics," *Journal of Physics: Condensed Matter*, Vol. 14, no. 18, pp. R597-R624, 2002.**

**[27]** **C. A. Murray and D. L. Allara, "Measurement of the molecule–silver separation dependence of surface enhanced Raman scattering in multilayered structures," *Journal of Chemical Physics*, Vol. 76, no. 3, pp. 1290-1303, 1982.**

**[28]** **F. J. Gracia-Vidal and J. B. Pendry, "Collective Theory for Surface Enhanced Raman Scattering," *Physical Review Letters*, Vol. 77, no. 3, pp. 1163-1166, 1996.**

**[29]** **K. Kneipp, H. Kneipp, I. Itzkan, R. R. Dasari, and M. S. Feld, "Ultrasensitive chemical analysis by Raman Spectrsocopy," *Chemical Reviews*, Vol. 99, no. 10, pp. 2957-2975, 1999.**

**[30]** **A. Otto, "The 'chemical' (electronic) contribution to surface-enhanced Raman scattering," *Journal of Raman Spectroscopy*, Vol. 36, pp. 497-509, 2005.**

**[31]** **L. Jensen, C. M. Aikens, and G. C. Schatz, "Electronic structure methods for studying surface-enhanced Raman scattering," *Chemical Society Reviews*, Vol. 37, no. 5, pp. 1061-1073, 2008.**

**[32]** **J. R. Lombardi, and R. L. Birke, "A Unified Approach to Surface-Enhanced Raman Spectroscopy," *Journal of Physical Chemistry C*, Vol. 112, no. 14, pp.5605-5617, 2008.**

**[33]** **J. I. Gersten, R. L. Birke, and J. R. Lombardi, "Theory of Enhance l Light Scattering from Molecules Adsorbed at the Metal-Solution Interface," *Physical Review Letters*, Vol. 43, no. 2, pp. 147-150, 1979.**

**[34]** **D. K. Chatterjee 1, P. Diagaradjane, S. Krishnan, "Nanoparticle-mediated hyperthermia in cancer therapy," *Therapeutic Delivery*, Vol. 2, no. 8, pp. 1001–1014, 2011.**

**[35]** **K. M. Kosuda, J. M. Bingham, K.L. Wustholz, and R. P. Van Duyne, "Nanostructures and Surface-Enhanced Raman Spectroscopy," *Comprehensive Nanoscience and Technology*, Vol. 3, pp. 263-301, 2011.**

**[36]** **K. L. Kelly, E. Coronado, L. L. Zhao, and G. C. Schatz, "The Optical Properties of Metal Nanoparticles: The Influence of Size, Shape, and Dielectric Environment," *Journal of Physical Chemistry B*, Vol. 107, no. 3, pp. 668-677, 2003.**

**[37]** **U. Kreibig, and C. V. Fragstein, "The limitation of electron mean free path in small silver particles," *Zeitschrift für Physik*, Vol. 224, pp. 307-323, 1969.**

**[38]** **C. L. Haynes, A. J. Haes, A. D. McFarland, and, R. P. Van Duyne, "Nanoparticles with Tunable Localized Surface Plasmon Resonances," *Topics in Fluorescence Spectroscopy*, Vol. 8, pp. 47-99, 2005.**

**[39]** **T. A. El-Brolossy, T. Abdallah, M. B. Mohamed, S. Abdallah, K. Easawi, S. Negm, and H. Talaat, "Shape and size dependence of the surface plasmon resonance of gold nanoparticles studied by Photoacoustic technique," *The European Physical Journal Special Topics*, Vol. 153, pp. 361-364, 2008.**

**[40]** **J. Cao, T. Sun, and K. T. V. Grattan, "Gold nanorod-based localized surface plasmon resonance biosensors: A review," *Sensors and Actuators B: Chemical,* Vol. 195, pp. 332-351, 2014.**

**[41]** **J. Cheng, X. Su, S. Wang, and Y. Zhao, "Highly Sensitive Detection of Clenbuterol in Animal Urine Using Immunomagnetic Bead Treatment and Surface-Enhanced Raman Spectroscopy," *Scientific Reports*, Vol. 6, no. 32637, pp. 1-10, 2016.**

**[42]** **L. M. Liz-Marzan, "Tailoring Surface Plasmons through the Morphology and Assembly ofMetal Nanoparticles," *Langmuir*, Vol. 22, no. 1, pp. 32-41, 2006.**

**[43]** **W. E. Doering, M. E. Piotti, M. J. Nattan, and R. G. Freeman, "SERS as a Foundation for Nanoscale, Optically Detected Biological Labels," *Advanced Materials*, Vol. 19. no. 20, pp. 3100-3108, 2007.**

**[44]** **K. Hering, D. Cialla, K. Ackermann, T. Dorfer, R. Moller, H. Schneidewind, R. Mattheis, W. Fritzsche, P. Rosch, and J. Popp, "SERS: a versatile tool in chemical and biochemical diagnostics," *Analytical and Bioanalytical Chemistry*, Vol. 390, pp. 113-124, 2008.**

**[45]** **J. B. Jackson and N. J. Halas, "Surface-enhanced Raman scattering on tunable plasmonic nanoparticle substrates," *Proceedings of the National Academy of Sciences of the United States of America*, Vol. 101, no. 52, pp. 17930-17935, 2004.**

**[46]** **J. A. Dieringer, K. L. Wustholz, D. J. Masiello, J. P. Camden, S. L. Kleinman, G. C. Schatz and R. P. Van Duyne, "Surface-Enhanced Raman Excitation Spectroscopy of a Single Rhodamine 6G Molecule," *Journal of the American Chemical Society*, Vol. 131, no. 2, 849-854, 2009.**

**[47]** **E. C. Le Ru, E. Blackie, M. Meyer and P. G. Etchegoin, "Surface Enhanced Raman Scattering Enhancement Factors: A Comprehensive Study," *Journal of the Physical Chemistry C*, Vol. 111, no. 37, pp. 13794-13803, 2007.**

**[48]** **P. L. Stiles, J. A. Dieringer, N. C. Shah, and R. P. Van Duyne, "Surface-Enhanced Raman Spectroscopy," *Annual Review of Analytical Chemistry*, Vol. 1, pp. 601-626, 2008.**

**[49]** **N. A. Cinel, S.Cakmakyapan, S. Butun, G. Ertas, and E. Ozbay, "E-Beam lithography designed substrates for surface enhanced Raman spectroscopy," *Photonics and Nanostructures - Fundamentals and Applications*, Vol. 15, pp. 109-115, 2015.**

**[50]** **A. Kudelski, "Raman studies of rhodamine 6G and crystal violet sub-monolayers on electrochemically roughened silver substrates: Do dye molecules adsorb preferentially on highly SERS-active sites?," *Chemical Physics Letters*, Vol. 414, no. 4-6, pp. 271-275, 2005.**

**[51]** **C. Ji, J. Lu, B. Shan, F. Li, X. Zhao, J. Yu, S. Xu, B. Man, C. Zhang, and Z. Li, "The Origin of Mo2C Films for Surface-Enhanced Raman Scattering Analysis: Electromagnetic or Chemical Enhancement?," *The Journal of Physical Chemistry Letters*, Vol. 13, no. 38, pp. 8864-8871, 2022.**

**[52]** **S. Bai, X. Ren, K. Obata, Y. Ito, and K. Sugioka, "Label-free trace detection of bio-molecules by liquid-interface assisted surface-enhanced Raman scattering using a microfluidic chip," *Opto-Electronic Advances*, Vol. 5, no. 10, pp. 210121-1- 210121-10, 2022.**

**[53]** **Z. Pei, J. Li, C. Ji, J. Tan, Z. Shao, X. Zhao, Z. Li, B. Man, J. Yu, and C. Zhang, "Flexible Cascaded Wire-in-Cavity-in-Bowl Structure for High-Performance and Polydirectional Sensing of Contaminants in Microdroplets," *The Journal of Physical Chemistry Letters*, Vol. 14, no. 25, pp. 5932-5939, 2023.**

**[54]** **M. S. S. Bharati and V. R. Soma, "Flexible SERS Substrates for Hazardous Materials Detection: Recent Advances," *Opto-Electronic Advances*, Vol. 4, no. 11, pp. 210048-1-210048-26, 2021.**

**[55]** **B. D. Gupta, A. Pathak, and A. M. Shrivastav, "Optical Biomedical Diagnostics Using Lab-on-Fiber Technology: A Review," *Photonics*, Vol. 9, no. 2, pp. 1-40, 2022.**

**[56]** **E. Verdon, and W. C. Andersen, "Certain Dyes as Pharmacologically Active Substances in Fish Farming and Other Aquaculture Products," *Food and Drug Administration Papers*, Vol. 13, pp. 497-548, 2017.**

**[57]** **J. Zhang, S. Chen, T. Gong, X. Zhang, and Y. Zhu, "Tapered Fiber Probe Modified by Ag Nanoparticles for SERS Detection," Vol. 11, pp. 743-751, 2016.**

**[58]** **Y. Ran, P. Strobbia, V. Cupil-Garcia, and T. Vo-Dinh, "Fiber-optrode SERS probes using plasmonic silver-coated gold nanostars," *Sensors and Actuators B: Chemical*, Vol 287, pp. 95-101, 2019.**

**[59]** **K. Milenko, S. S. Fuglerud, A. Aksnes, R. Ellingsen, and D. R. Hjelme, "Optimization of SERS Sensing With Micro-Lensed Optical Fibers and Au Nano-Film," *Journal of Lightwave Technology*, Vol. 38, no. 7, pp. 2081-2085, 2020.**

**[60]** **Z. Yu, Z. Wang, and J. Zhang, "Preparation optimization for a silver cavity coupled tapered fiber SERS probe with high sensitivity," *Optical Materials Express*, Vol. 12, no. 7, pp. 2835-2843, 2022.**

**[61]** **C. Liu, S.Wang, G. Chen, S. Xu, Q. Jia, J. Zhou, and W. Xu, "A surface-enhanced Raman scattering (SERS)-active optical fiber sensor based on a three-dimensional sensing layer," *Sensing and Bio-Sensing Research*, Vol. 1, pp. 8-14, 2014.**

**[62]** **Z. Xie, S. Feng, P. Wang, L. Zhang, X. Ren, L. Cui, T. Zhai, J. Chen, Y. Wang, X. Wang, W. Sun, J. Ye, P. Han, P. J. Klar, and Y. Zhang, "Demonstration of a 3D Radar-Like SERS Sensor Micro- and Nanofabricated on an Optical Fiber," *Advanced Optical Materials*, Vol. 3, no. 9. 1232-1239, 2015.**

**[63]** **F. Zhou, Y. Liu, H. Wang, Y. Wei, G. Zhang, H. Ye, M. Chen, and D. Ling, "Au-nanorod-clusters patterned optical fiber SERS probes fabricated by laser-induced evaporation self-assembly method," Vol. 28, no. 5, pp. 6648-6662, 2020.**

**[64]** **C. Gu, Z. Zhao, and P. Shi, "Development of monolayer AuNPs decorated on an optical fiber facet for SERS analysis," *Applied Optics*, Vol. 60, no. 3, pp. 792-798, 2021.**

**[65]** **A. Ashkin, J. M. Dziedzic, J. E. Bjorkholm, and Steven Chu, "Observation of a single-beam gradient force optical trap for dielectric particles," Vol. 11, no. 5, pp. 288-290, 1986.**

**[66]** **A. Ashkin, "Trapping of Atoms by Resonance Radiation Pressure," *Physical Review Letters*, Vol. 40, no. 12, pp. 729-733, 1978.**

**[67]** **A. Ashkin, "Optical trapping and manipulation of neutral particles using lasers," *Proceedings of the National Academy of Sciences of the United States of America*, Vol. 94, no. 10, pp. 4853-4860, 1997.**

**[68]** **A. Lehmuskero, P. Johansson, H. Rubinsztein-Dunlop, L. Tong, and M. Käll, "Laser trapping of colloidal metal nanoparticles," *ACS Nano*, Vol. 9, No. 4, pp. 3453-3469, 2015.**

**[69]** **K.C. Neuman and S.M. Block, "Optical Trapping," *Review Of Scientific Instruments*, Vol. 75, no. 9, pp. 2787-2809, 2004.**

**[70]** **K. Svoboda and S. M. Block, "Optical trapping of metallic Rayleigh particles," *Optics Letters*, Vol. 19, no. 13, pp. 930-932, 1994.**

**[71]** **E. Izake, B. Cletus, W. Olds, S. Sundarajoo, P. Fredericks, and E. Jaatinen, "Deep Raman spectroscopy for the non-invasive standoff detection of concealed chemical threat agents," *Talanta*, Vol. 94, pp. 342-347, 2012.**

**[72]** **S. Yang, X. Dai, B. B. Stogin, and T.S. Wong, "Ultrasensitive surface-enhanced Raman scattering detection in common fluids," *Proceedings of the National Academy of Sciences of the United States of America*, Vol. 113, no. 2, 268-273, 2015.**

**[73]** **C. Shi, Y. Zhang, C. Gu, B. Chen, L. Seballos, T. Olson, and J. Z. Zhang, "Molecular fiber sensors based on surface enhanced Raman scattering (SERS)," *Journal of Nanoscience and Nanotechnology*, Vol. 9, no. 4, pp. 2234-2246, 2009.**

**[74]** **H. Kneipp, J. Kneipp, and K. Kneipp, "Surface-Enhanced Raman Optical Activity on Adenine in Silver Colloidal Solution," *Analytical Chemistry*, Vol. 78, no. 4, pp. 1363-1366, 2006.**

**[75]** **R. S. Golightly, W. E. Doering, M. J. Natan, "Surface-Enhanced Raman Spectroscopy and Homeland Security: A Perfect Match?," *ACS Nano*, Vol. 3, no. 10, pp. 2859-2869, 2009.**

**[76]** **C. Zhao, N. Chen, S. Liu, Z. Chen, and T. Wang, "Gold nanoparticles modified double-tapered fiber for SERS detection," *Journal of Physics: Conference Series*, Vol. 844, pp. 1-5, 2017.**

**[77]** **I. Ros, T. Placido, V. Amendola, C. Marinzi, N. Manfredi, R. Comparelli, M. Striccoli, A. Agostiano, A. Abbotto, D. Pedron, R. Pilot, and R. Bozio, "SERS Properties of Gold**

**Nanorods at Resonance with Molecular, Transverse, and Longitudinal Plasmon Excitations," *Plasmonics*, Vol. 9, no. 3, pp. 581-593, 2014.**

**[78] B. Nikoobakht and M. A. El-Sayed, "Surface-Enhanced Raman Scattering Studies on Aggregated Gold Nanorods," *The Journal of Physical Chemistry A*, Vol 107, no. 18, pp. 3372-3378, 2003.**

**[79] C. J. Murphy, A. M. Gole, S. E. Hunyadi, J. W. Stone, P. N. Sisco, A. Alkilany, B. E. Kinarda, and P. Hankinsa, "Chemical sensing and imaging with metallic nanorods," *Chemical Communications*, Vol. 8, no. 5, pp. 544-557, 2008.**

**[80] G. Lu, T. Z. Forbes, and A. J. Haes, "SERS detection of uranyl using functionalized gold nanostars promoted by nanoparticle shape and size," *Analyst*, Vol. 141, no. 17, pp. 5137-5143, 2016.**

**[81] K. M. Kosuda, J. M. Bingham, K. L. Wustholz, R. P. Van Duyne, and R. J. Groarke, "Nanostructures and Surface-Enhanced Raman Spectroscopy," *Comprehensive Nanoscience, and Technology*, 2nd ed, Vol. 4, pp. 117-152, 2011.**

**[82] X. Lu, M. Rycenga, S. E. Skrabalak, B. Wiley, and Y. Xia, "Chemical synthesis of novel plasmonic nanoparticles," *Annual Review of Physical Chemistry*, Vol. 60, pp. 167-192, 2009.**

**[83] S. M. Nie and S. R. Emery, " Probing Single Molecules and Single Nanoparticles by Surface-Enhanced Raman Scattering," *Science*, Vol. no. 5303, pp. 1102-1106, 1997.**

**[84] K. Kneipp, Y. Wang, H. Kneipp, L. T. Perelman, I. Itzkan, R. R. Dasari, and M. S. Feld, "Single Molecule Detection Using Surface-Enhanced Raman Scattering (SERS)," *Physical Review Letters*, Vol. 78, no. 9, pp. 1667-1670, 1997.**

**[85] S. Al-Shahrani, "Phenomena of Removal of Crystal Violet from Wastewater Using Khulays Natural Bentonite," *Journal of Chemistry*, Vol. 4, pp. 1-8, 2020.**

**[86] A. J. Leong, N. Nyuk-Ting, N. S. Mohd. Nor, U. Baig, W. A.W. Ibrahim. M. M. Sanagi, A. S. A. Keyon, "Removal of rhodamine 6G and crystal violet dyes from water sample using cellulose acetate-(3-aminopropyl)-triethoxysilane sorbent," *AIP Conference Proceedings*, Vol. 2155, no. 1, pp. 1-7, 2019.**

**[87]** **Z.Chen, Z. Dai, N. Chen, S. Liu, F.Pang, and B. Lu, "Gold Nanoparticles-Modified Tapered Fiber Nanoprobe for Remote SERS Detection," IEEE Photonics Technology Letters, Vol. 26, No. 8, pp. 777-780, 2014.**

**[88]** **N. Kaur, J. O. Trevisanutto, and G. Das, "Plasmonic structure on a tapered optical fiber for application as a surface-enhanced Raman spectroscopy substrate," *Microwave and Optical Technology Letters*, Vol. 63, no. 11, pp. 2776-2781, 2021.**

**[89]** **K. Karapetyan, W. Alt, and D. Meshchede, "Optical fiber toolbox for MATLAB, version 2.1, http://www.mathworks.com/matlabcentral/fileexchange/27819," 2011.**

**[90]** **A. Ashkin, J. M. Dziedzic, and T. Yamane, "Optical trapping and manipulation of single cells using infrared laser beams," *Nature*, Vol. 330, no. 6150, pp.769-771, 1987.**

**[91]** **N. Kaur, J. O. Trevisanutto, and G. Das, "Tweezing and manipulating the distribution of gold nanorods (GNRs) on a tapered optical fiber to develop a plasmonic structure," *OSA Continuum*, Vol. 3, no. 9, pp. 2415-2422, 2020.**

**[92]** **R. D. Deegan, O. Bakajin, T. F. Dupont, G. Huber, S. R. Nagel, and T. A. Witten, "Capillary flow as the cause of ring stains from dried liquid drops," *Nature*, Vol. 389, pp. 827-829, 1997.**

**[93]** **N. Kaur and G. Das, " Three-dimensional plasmonic substrate as surface-enhanced Raman spectroscopy (SERS) tool for the detection of trace chemicals," *Journal of Raman Spectroscopy*, Vol. 55, no. 4, pp. 473-480, 2024.**

**[94]** **X. Fu, Z. Wang, J. Li, S. Ma, G. Fu, W. Jin, W. Bi, and Y. Dong, "Microcavity Fiber SERS Probe Coated With Ag Nanoparticles for Detecting Antibiotic in Milk," *IEEE Photonics Journal*, Vol. 13, no. 2, pp. 1-14, 2021.**

**[95]** **X. N. He, Y. Gao, M. Mahjouri-Samani, P. N. Black, J. Allen, M. Mitchell, W. Xiong, Y. S. Zhou, L. Jiang, and Y. F. Lu, "Surface-enhanced Raman spectroscopy using gold-coated horizontally aligned carbon nanotubes," *Nanotechnology*, Vol. 23, no. 20, pp. 1-9, 2012.**

**[96]** **P. Pino, F. Bosco, C. Mollea, and B. Onida, "Antimicrobial Nano-Zinc Oxide Biocomposites for Wound Healing Applications: A Review," *Pharmaceutics*, Vol. 15, no. 3, pp. 1-27, 2023.**

**[97]** **J. Jiang, J. Pi, and J. Cai, "The Advancing of Zinc Oxide Nanoparticles for Biomedical Applications," *Bioinorganic and Chemistry and Applications*, Vol. 3, pp. 1-18, 2018.**

**[98]** **D. M. Bagnall, Y. F. Chen, Z. Zhu, T. Yao, S. Koyama, M. Y. Shen, and T. Goto, "Optically pumped lasing of ZnO at room temperature," Vol. 70, no. 17, pp. 2230-2232, 1997.**

**[99]** **J. Hahm, "Fundamental Properties of One-Dimensional Zinc Oxide Nanomaterials and Implementations in Various Detection Modes of Enhanced Biosensing," *Annual Review of Physical Chemistry*, Vol. 67, pp. 691-717, 2016.**

**[100]** **R. Kumar, O. Al-Dossary, G. Kumar, and A. Umar, "Zinc Oxide Nanostructures for $NO_2$ Gas-Sensor Applications: A Review," *Nano-Micro Letters*, Vol. 7, pp. 97-120, 2015.**

**[101]** **S. Sabir, M. Arshad, and S. K. Chaudhari, " Zinc oxide nanoparticles for revolutionizing agriculture: synthesis and applications," *Scientific World Journal*, pp. 1-8, 2014.**

**[102]** **H. Q. Wang, G. H. Li, L. C. Jia, G. Z. Wang, and L. Li, "General in situ chemical etching synthesis of ZnO nanotips array," *Applied Physics Letters*, Vol. 93, no. 15, 2008.**

**[103]** **S. G. Leonardi, "Two- Dimensional Zinc Oxide Nanostructures for Gas Sensor Applications," *Chemosensors*, Vol. 5, no. 2, 2017.**

**[104]** **M. A. Shah, M. S. Al-Shahry, and A. M. Asiri, "Simple approach for the synthesis of zinc oxide nanorods," *International Journal of Nanoparticles*, Vol. 2, no. 1-6, pp. 66-73, 2009.**

**[105]** **L. Znaidi, "Sol-gel-deposited ZnO thin films: A review," *Materials Science and Engineering B*, Vol. 174, no. 1-3, pp. 18-30, 2010.**

**[106]** **L. Schlur, J. R. Calado, and D. Spitzer, " Synthesis of zinc oxide nanorods nanotubes on one side of a microcantilever," *Royal society of Open Science*, Vol. 5, no. 8, pp. 1-11, 2018.**

**[107]** **E. Mosayebi, S. Azizian, and A. Hajian, "Synthesis of nanostructured and microstructured ZnO and Zn(OH)2 on activated carbon cloth by hydrothermal and microwave-assisted chemical bath deposition methods," *Superlattices and Microstructures*, Vol. 81, pp. 226-232, 2015.**

**[108]** **T. Thilagavathi, and D. Geetha, "Nano ZnO structures synthesized in presence of anionic and cationic surfactant under hydrothermal process," *Applied Nanoscience*, Vol. 4, pp. 127-132, 2014.**

**[109]** **Y. D. Wang, S. Zhang, C. L. Ma, and H. D. Li, " Synthesis and room temperature photoluminescence of ZnO/CTAB ordered layered nanocomposite with flake-like architecture," *Journal of Luminescence*, Vol. 126, no. 2, pp. 661-664, 2007.**

**[110]** **C. M. Chou, L. T. T. Thi, N. T. Q. Nhu, S. Y. Liao, Y. Z. Fu, L. V. T. Hung, and V. K. S. Hsiao, "Zinc Oxide Nanorod Surface-Enhanced Raman Scattering Substrates without and with Gold Nanoparticles Fabricated through Pulsed-Laser-Induced Photolysis," *Applied Sciences*, Vol. 10, no. 14, pp. 1-11, 2020.**

**[111]** **S. Lee and J. K. Kim, " Surface-Enhanced Raman Spectroscopy (SERS) Based on ZnO Nanorods for Biological Applications," *Book: Zinc Oxide Based Nano Materials and Devices*, 2019.**

**[112]** **A. Colniță, V. A. Toma, I. A. Brezeștean, M. A. Tahir, and N. E. Dina, "A Review on Integrated ZnO-Based SERS Biosensors and Their Potential in Detecting Biomarkers of Neurodegenerative Diseases," *Biosensors*, Vol. 13, no. 5, pp. 499-1-499-33, 2023.**

**[113]** **S. Adesoye, S. Al AQbdullah, A. Kumari, G. Pathiraja, K. Nowlin, K., and K. Dellinger, "Au-Coated ZnO Surface-Enhanced Raman Scattering (SERS) Substrates: Synthesis, Characterization, and Applications in Exosome Detection," *Chemosensors*, Vol. 11, no. 11 pp. 554-1-554-14, 2023.**

**[114]** **M. E. Koleva, N. N. Nedyalkov, Ru. Nikov, Ro. Nikov, G. Atanasova, D. Karashanova, V. I. Nuzhdin, V. F., Valeev, A. M. Rogov, and A. L. Stepanov, "Fabrication of**

**Ag/ZnO nanostructures for SERS applications," *Applied Surface Science*, Vol. 508, pp. 1-9, 2020.**

**[115] N. H. Ke, N. H. Thanh, N. H. Long, D. A. Tuan, and L.V. T. Hung, "Fabrication of Ag–ZnO NRs SERS substrates for abamectin detection: the effect of Ag sputtering times and ZnO sol concentrations in seed layer preparation on SERS performance," *Journal of Materials Science: Materials in Electronics*, Vol. 32, no. 23, pp. 27318-27332, 2021.**

**[116] H. H. M. Yusof, H. R. A. Rahim, S. Thokchom, K. Dimyati, and S. W. Harun, " Uric acid sensing using tapered silica optical fiber coated with zinc oxide nanorods," *Microwave and Optical Technology Letters*, Vol. 60, no. 3, pp. 645-650, 2018.**

**[117] M. Batumalay, Z. Harith, H. A. Rafaie, F. Ahmad, M. Khasanah, S. W. Harun, R. M. Nor, and H. Ahmad, "Tapered plastic optical fiber coated with znO nanostructures for the measurement of uric acid concentrations and changes in relative humidity," *Sensors and Actuators A: Physical*, Vol. 210, pp. 190-196, 2014.**

**[118] M. Kosowska, P. Listewnik, D. Majchrowicz, M. Rycewicz, M. Bechelany, Y. Fleger, M. Chen, D. Fixler, K. Dholakia and M. Szczerska, "Microscale diamond protection for a ZnO coated fiber optic sensor," *Nature*, Vol. 10, pp. 1-8, 2020.**

**[119] T.V. Le, T. B. N. Vo, Y. J. Gwon, H. K. Lee, and S. W. Lee, "Fiber-Optic Sensing System Using Polyhedral Plasmonic Nanostructures as SERS-Active Substrates", ACS Applied Nano Materials, Vol. 7, no. 17, pp. 21114-21123, 2024.**

**[120] N. Kaur and G. Das, "ZnO Plasmonic Structure on a Tapered Optical Fiber," *OSA Optical Sensors and Sensing Congress*, JTh6A.39, Washington, DC, USA, July 2021.**

**[121] N. Kaur and G. Das, "Plasmonic structure of zinc (Zn) and zinc oxide (ZnO) on a tapered optical fiber," *Optical Materials Express*, Vol. 12, no. 9, pp. 3821-3828, 2022.**

**[122] A. Degen and M. Kosec, "Effect of pH and impurities on the surface charge of zinc oxide in aqueous solution," *Journal of the European Ceramic Society*, Vol. 20, no. 6, pp. 667-673, 2000.**

**[123]** **T. Ghoshal, S. Kar, and S. Chaudhuri, "Synthesis and optical properties of nanometer to micrometer wide hexagonal cones and columns of ZnO," *Journal of Crystal Growth*, Vol. 293, no. 2, pp. 438-446, 2006.**

**[124]** **G. M. Abdelghani, A. B. Ahmed, and A. B. Al-Zubaidi, "Synthesis, characterization, and influence of energy of irradiation on optical properties of ZnO nanostructures," *Nature*, Vol. 12, pp. 1-17, 2022.**

**[125]** **S. Abdi and D. Dorranian, "Effect of CTAB concentration on the properties of ZnO nanoparticles produced by laser ablation method in CTAB solution," *Optics and Laser Technology*, Vol. 108, pp. 372-377, 2018.**

**[126]** **J. C. Whitmer, "Using the Aufbau Principle," *Journal of Chemical Educatrion*, Vol. 55, no. 8, pp. 515, 1978.**

**[127]** **S. A. Meyer, E. C. Le Ru, and P. G. Etchegoin, "Combining Surface Plasmon Resonance (SPR) Spectroscopy with Surface-Enhanced Raman Scattering (SERS)," *Analytical Chemistry*, Vol. 83, no. 6, pp. 2337-2344, 2011.**

**[128]** **H. P. Myers, "Introductory Solid State Physics", 2nd ed 1997.**

**[129]** **L. Kool, F. Dekker, A. Bunschoten, G. J. Samles, B. R. Pauw, A. H. Velders, and V. Saggiomo, "Gold and silver dichroic nanocomposite in the quest for 3D printing the Lycurgus cup," Beilstein Journal of Nanotechnology, Vol. 11, pp. 16-23, 2020.**

**[130]** **G. Mie, "Beitrage zur Optik truber Medien, speziell kolloidaler Metallosungen," *Annalen der Physik*, Vol. 330, no. 3, pp. 377-445, 1908.**

**[131]** **C. F. Bohren and D. R. Huffman, "Absorption and Scattering of Light by Small Particles," 1983.**

**[132]** **J. A. Stratton, "Electromagnetic Theory," McGraw-Hill, New York, 1941.**

**[133]** **A. Garifullina, and A. Q. Shen, "Optimized Immobilization of Biomolecules on Nonspherical Gold Nanostructures for Efficient Localized Surface Plasmon Resonance Biosensing." Analytical Chemistry, Vol. 91, no.23, pp. 15090-15098, 2019.**

**[134]** **J. Perez-Juste, I. Pastoriza-Santos, L. M. Liz-Marzan, and P. Mulvaney, "Gold nanorods: Synthesis, characterization and applications," *Coordination Chemistry Reviews*, Vol. 249, no. 17, pp. 1870-1901, 2005.**

**[135]** **M. R. K. Ali, B. Snyder, and M. A. El-Sayed, "Synthesis and Optical Properties of Small Au Nanorods Using a Seedless Growth Technique," *Langmuir*, Vol. 28, no. 25, pp. 9807-9815, 2012.**

**[136]** **C. A. Foss, G. L. Hornyak, J. A. Stockert, and C. R. Martin, "Optical Properties of composite membranes containing arrays of nanoscopic gold cylinders," *The Journal of Physical Chemistry*, Vol. 96, no. 19, pp. 7497-7499, 1992.**

**[137]** **C. R. Martin, "Nanomaterials: A Membrane-Based Synthetic Approach," *Science*, Vol. 266, no. 5193, pp. 1961-1966, 1994.**

**[138]** **C. R. Martin, "Membrane-Based Synthesis of Nanomaterials," Chemistry of Materials, Vol. 8, no. 8, pp. 1739-1746, 1996.**

**[139]** **B. M. I. van der Zande, M. R. Bohmer, L. G. J. Fokkink, and C.Schonenberger, "Colloidal Dispersions of Gold Rods: Synthesis and Optical Properties," Langmuir, Vol. 16, no. 2, pp. 451-458, 2000.**

**[140]** **Y. Y. Yu, S. S. Chang, C. L. Lee, and C. R. C. Wang, "Gold Nanorods: Electrochemical Synthesis and Optical Properties," *The Journal of Physical Chemistry B*, Vol. 101, no. 34, pp. 6661-6664, 1997.**

**[141]** **S. S. Chang, C. W. Shih, C. D. Chen, W. C. Lai, and C. R. C. Wang, "The Shape Transition of Gold Nanorods," *Langmuir*, Vol. 15, no. 3, pp. 701-703, 1999.**

**[142]** **M. T. Reetz, and W. Helbig, "Size-Selective Synthesis of Nanostructured Transition Metal Clusters," *Journal of the American Chemical Society*, Vol. 116, no. 16, pp. 7401-7402, 1994.**

**[143]** **N. R. Jana, L. Gearheart, and C. J. Murphy, "Seed-Mediated Growth Approach for Shape-Controlled Synthesis of Spheroidal and Rod-like Gold Nanoparticles Using a Surfactant Template," *Advanced Materials*, Vol. 13, no. 18, pp. 1389-1393, 2001.**

**[144]** **B. Nikoobakht, and M. A. El-Sayed, "Preparation and Growth Mechanism of Gold Nanorods (NRs) Using Seed-Mediated Growth Method," *Chemistry of Materials*, Vol. 15, no. 10, pp. 1957-1962, 2003.**

**[145]** **N. R. Jana, L. Gearheart, and C. J. Murphy, "Wet Chemical Synthesis of High Aspect Ratio Cylindrical Gold Nanorods," *The Journal of Physical Chemistry B*, Vol. 105, no. 19, pp. 4065-4067, 2001.**

**[146]** **T. K. Sau, and C. J. Murphy, "Seeded High Yield Synthesis of Short Au Nanorods in Aqueous Solution," *Langmuir*, Vol. 20, no. 15, pp. 6414-6420, 2004.**

**[147]** **L. Gou, and C. J. Murphy, "Fine-Tuning the Shape of Gold Nanorods," *Chemistry of Materials*, Vol. 17, no. 14, pp. 3668-3672, 2005.**

**[148]** **D. K. Smith and B. A. Korgel, "The Importance of the CTAB Surfactant on the Colloidal Seed-Mediated Synthesis of Gold Nanorods," *Langmuir*, Vol. 24, no. 3, pp. 644-649, 2008.**

**[149]** **N. R. Jana, Gram-Scale Synthesis of Soluble, Near-Monodisperse Gold Nanorods and Other Anisotropic Nanoparticles," *Small*, Vol. 1, no. 8-9, pp. 875-882, 2005.**

**[150]** **K. Okitsu, K. Sharyo, K., and R. Nishimura, "One-Pot Synthesis of Gold Nanorods by Ultrasonic Irradiation: The Effect of pH on the Shape of the Gold Nanorods and Nanoparticles," *Langmuir*, Vol. 25, no. 14, pp. 7786-7790, 2009.**

**[151]** **C. Bullen, M. J. Latter, N. J. D'Alonzo, G. J. Willis, and C. L. Raston, "A seedless approach to continuous flow synthesis of gold nanorods," *The Royal Society of Chemistry*, Vol. 47, no. 14, pp. 4123-4125, 2011.**

**[152]** **X. Xu, Y. Zhao, X. Xue, S. Huo, F. Chen, G. Zou, and X. J. Liang, "Seedless synthesis of high aspect ratio gold nanorods with high yield," *Journal of Materials Chemistry A*, Vol.2, no. 10, pp. 3528-3535, 2014.**

**[153]** **J. Zhang, C. Xi, C. Feng, H. Xia, D. Wang, and X. Tao, "High Yield Seedless Synthesis of High-Quality Gold Nanocrystals with Various Shapes," *Langmuir*, Vol. 30, no. 9, pp. 2480-2489, 2014.**

**[154]** **V. Sebastian, S. K. Lee, C. Zhou, M. F. Kraus, and J. G. Fujimoto, "One-step continuous synthesis of biocompatible gold nanorods for optical coherence tomography," *Chemical Communications*, Vol. 48, no. 53, pp. 6654-6656, 2012.**

**[155]** **X. Ye, Y. Gao, J. Chen, D. C. Reifsnyder, C. Zheng, and C. B. Murray, "Seeded Growth of Monodisperse Gold Nanorods Using Bromide-Free Surfactant Mixtures," *Nano Letters*, Vol. 13, no. 5, pp. 2163-2171, 2013.**

**[156]** **Z. Lin, J. J. Cai, L. E. Scriven, and H. T. Davis, "Spherical-to-Wormlike Micelle Transition in CTAB Solutions," *The Journal of Physical Chemistry*, Vol. 98, no. 23, pp. 5984-5993, 1994.**

**[157]** **C. J. Murphy, L. B. Thompson, D. J. Chernak, J. A. Yang, S. T. Sivapalan, S. P. Boulos, J. Huang, A. M. Alkilany, and P. N. Sisco, "Gold nanorod crystal growth: From seed-mediated synthesis to nanoscale sculpting," *Current Opinion in Colloid and Interface Science*, Vol. 16, no. 2, pp. 128-134, 2011.**

**[158]** **J. A. da Silva, P. A. Netz, and M. R. Meneghetti, "Growth Mechanism of Gold Nanorods: the Effect of Tip-Surface Curvature as Revealed by Molecular Dynamics Simulations," *Langmuir*, Vol. 36, pp. 257-263, 2020.**

**[159]** **S. Lee, L. J. E. Anderson, C. M. Payne, and J. H. Hafner, "Structural Transition in the Surfactant Layer that Surrounds Gold Nanorods as Observed by Analytical Surface-Enhanced Raman Spectroscopy," *Langmuir*, Vol. 27, no. 24, pp. 14748-14756, 2011.**

**[160]** **S. Gomez-Grana, F. Hubert, F. Testard, A. Guerrero-Martinez, I. Grillo, L. M. Liz-Marzan, and O. Spalla, "Surfactant (Bi)Layers on Gold Nanorods," *Langmuir*, Vol. 28, no. 2, pp. 1453-1459, 2012.**

**[161]** **K. K. Caswell, J. N. Wilson, U. H. F. Bunz, and C. J. Murphy, "Preferential End-to-End Assembly of Gold Nanorods by Biotin-Streptavidin Connectors," *Journal of the American Chemical society*, Vol. 125, no. 46, pp. 13914-13915, 2003.**

**[162]** **A. K. Oyelere, P. C. Chen, X. Huang, I. H. El-Sayed, and M. A. El-Sayed, "Peptide-Conjugated Gold Nanorods for Nuclear Targeting," *Bioconjugate chemistry*, Vol. 18, no. 5, pp. 1490-1497, 2007.**

**[163]** **L. A. Dykman, and N. G. Khlebtsov, "Gold Nanoparticles in Biology and Medicine: Recent Advances and Prospects," *Acta Naturae*, Vol. 3, no. 2, pp. 34-55, 2011.**

**[164]** **J. Wan, J. H. Wang, T. Liu, Z. Xie, X. F. Yu, and W. Li, "Surface Chemistry but not aspect ratio mediates the biological toxicity of gold nanorods in vitro and in vivo," *Nature*, Vol. 5, pp. 1-16, 2015.**

**[165]** **M. Tebbe, C. Kuttner, M. Mannel, A. Fery, and M. Channa, "Colloidally Stable and Surfactant-Free Protein-Coated Gold Nanorods in Biological Media," *ACS Applied Materials and Interfaces*, Vol. 7, no. 10, pp. 5984-5991, 2015.**

**[166]** **E. Locatelli, I. Monaco, and M. C. Franchini, "Surface modifications of gold nanorods for applications in nanomedicine," *The Royal Society of Chemistry*, Vol. 5, no. 8, pp. 21681-21699, 2015.**

**[167]** **X. Shi, H. L. Perry, and J. D. E. T. Wilton-Ely, "Strategies for the functionalisation of gold nanorods to reduce toxicity and aid clinical translation," *Nanotheranostics*, Vol. 5, No. 2, pp. 155-165, 2021.**

**[168]** **J. Zhou, Z. Cao, N. Panwar, R. Hu, X. Wang, J. Qu, S. C. Tjin, G. Xu, and K. T. Yong, "Functionalized gold nanorods for nanomedicine: Past, present and future," *Coordination Chemistry Reviews*, Vol. 352, pp. 15-66, 2017.**

**[169]** **K. Liu, Y. Zheng, X. Lu, T. Thai, N. A. Lee, U. Bach, and J. J. Gooding, "Biocompatible Gold Nanorods: One-Step Surface Functionalization, Highly Colloidal Stability, and Low Cytotoxicity," *Langmuir*, Vol. 31, no. 17, pp. 4973-4980, 2015.**

**[170]** **H. Liao and J. H. Hafner, "Gold Nanorod Bioconjugates," *Chemistry of Materials*, Vol. 17, no. 18, pp. 4636-4641, 2005.**

**[171]** **S. Pierrat, I. Zins, A. Breivogel, and C. Sonnichsen, "Self-Assembly of Small Gold Colloids with Functionalized Gold Nanorods," *Nano Letters*, Vol. 7, no. 2, pp. 259-263, 2007.**

**[172]** **Z. Zhang and M. Lin, "Fast loading of PEG-SH on CTAB-protected gold nanorods," *The Royal Society of Chemistry Advances*, Vol. 4, no. 34, pp. 17760-17767, 2014.**

**[173]** **A. Agarwal, K. Venkatakrishnan, and B. Tan, "Cancer signaling by plasmonic quantum probes," *Applied Materials Today*, Vol. 18, 2020.**

**[174]** **T. Niidome, M. Yamagata, Y. Okamoto, Y. Akiyama, H. Takahashi, T. Kawano, Y. Katayama, and Y. Niidome, "PEG-modified gold nanorods with a stealth character for in vivo applications," *Journal of Controlled Release*, Vol. 114, no. 3, pp. 343-347, 2006.**

**[175]** **L. Uson, V. Sebastian, M. Arruebo, and J. Santamaria, "Continuous microfluidic synthesis and functionalization of gold nanorods," *Chemical Engineering Journal*, Vol. 285, pp. 286-292, 2016.**

**[176]** **F. Barbero, O. H. Moriones, N. G. Bastus, and V. Puntes, "Dynamic Equilibrium in the Cetyltrimethylammonium Bromide-Au Nanoparticle Bilayer, and the Consequent Impact on the Formation of the Nanoparticle Protein Corona," *Bioconjugate chemistry*, Vol. 30, no. 11, pp. 2917-2930, 2019.**

**[177]** **C. J. Murphy, L. B. Thompson, A. M. Alkilany, P. N. Sisco, S. P. Boulos, S. T. Sivapalan, J. A. Yang, D. J. Chernak, and J. Huang, "The Many Faces of Gold Nanorods," *The Journal of Physical Chemistry Letters*, Vol. 1, no. 9, pp. 2867-2875, 2010.**

**[178]** **Z. Khan, T. Singh, J. I. Hussain, and A. A. Hashmi, "Au(III)-CTAB reduction by ascorbic acid: Preparation and characterization of gold nanoparticles," *Colloids and Surfaces B Biointerfaces*, Vol. 104, pp. 11-17, 2013.**

**[179]** **L. Scarabelli, A. Sanchez-Iglesias, J. Perez-Juste, and L. M. Liz-Marzan, "A "Tips and Tricks" Practical Guide to the Synthesis of Gold Nanorods," The Journal of Physical Chemistry Letters, Vol. 6, no. 21, pp. 4270-4279, 2015.**

**[180]** **S. S. Chang, C. W. Shih, C. D. Chen, W. C. Lai, and C. R. C. Wang, "The Shape Transition of Gold Nanorods," *Langmuir*, Vol. 15, no. 3, pp. 701-709, 1999.**

**[181]** **C. J. Murphy, T. K. Sau, A. M. Gole, C. J. Orendroff, J. Gao, L. Gou, S. E. Hunyadi, and T. Li, "Anisotropic Metal Nanoparticles: Synthesis, Assembly, and Optical Applications," *The Journal of Physical Chemistry B*, Vol. 109, no. 29, pp. 13857-13870, 2005.**

**[182]** **L. Roach, P. L. Coletta, K. Critchley, and S. D. Evans, "Controlling the Optical Properties of Gold Nanorods in One-Pot Syntheses," *The Journal of Physical Chemistry C*, Vol. 126, no. 6, pp. 3235-3243, 2022.**

**[183]** **H. Li, G. Zheng, L. Xu, and W. Su, "Influence of amount of CTAB and ascorbic acid concentration on localized surface plasmon resonance property of gold nanorod," *Optik*, Vol. 125, no. 9, pp. 2044-2047, 2014.**

**[184]** **C. M. Aguirre, C. E. Moran, J. F. Young, and N. J. Halas, "Laser-Induced Reshaping of Metallodielectric Nanoshells under Femtosecond and Nanosecond Plasmon Resonant Illumination," *The Journal of Physical Chemistry B*, Vol. 108, no. 22, pp. 7040-7045, 2004.**

**[185]** **N. D. Burrows, W. Lin, G. H. Hinman, J. M. Dennison, A. M. Vartanian, N. S. Abadeer, E. M. Grzincic, L. M. Jacob, J. Li, and C. J. Murphy, "Surface Chemistry of Gold Nanorods," Langmuir, Vol. 32, no. 39, pp. 9905-9921, 2016.**

**[186]** **C. L. John, S. L. Strating, K. A. Shephard, and J. X. Zhao, "Reproducibility synthesize gold nanorods and maintain their stability," *The Royal Society of Chemistry Advances*, Vol. 3, no. 10909-10918, 2013.**

**[187]** **V. Sharma, K. Park, and M. Srinivasarao, "Colloidal dispersion of gold nanorods: Historical background, optical properties, seed-mediated synthesis, shape separation and self-assembly," *Materials Science and Engineering: R: Reports*, Vol. 65, no. 1-3, 2009.**

**[188]** **R. Goel, S. Chakraborty, V. Awasthi, V. Bhardwaj, and S. K. Dubey, "Exploring the various aspects of Surface enhanced Raman spectroscopy (SERS) with focus on the recent progress: SERS-active substrate, SERS-instrumentation, SERS-application," *Sensors and Actuators: A: Physical*, Vol. 376, no. 2, pp. 1-40, 2024.**

**[189]** **J. M. Bello, V. A. Narayan, D. L. Stokes, and V. D. Tuan, "Fiber-Optic Remote Sensor for in Situ Surface-Enhanced Raman Scattering Analysis," *Analytical Chemistry*, Vol. 62, no. 42, pp. 2437-2441, 1990.**

**[190]** **D. L. Stokes, J. P. Alarie, and T. Vo-Dinh, "Surface-enhanced Raman fiber optic sensors for remote monitoring," *Environmental Monitoring and Hazardous Waste Site Remediation*, Vol. 2504, pp. 552-558, 1995.**

**[191]** **D. L. Stokes, and T. Vo-Dinh, "Development of an integrated single-fiber SERS sensor," *Sensors and Actuators B: Chemical*, Vol. 69, no. 1-2, pp. 28-36, 2000.**

**[192]** **X. Zheng, D. Guo, Y. Shao, S. Jia, S. Xu, B. Zhao, W. Xu, C. Corredor, and J. R. Lombardi, "Photochemical Modification of an Optical Fiber Tip with a Silver Nanoparticle Film: A SERS Chemical Sensor," *Langmuir*, Vol. 24, no. 8, pp. 4394-4398, 2008.**

**[193]** **X. Zhi-Guo, L. Yong-Hua, W. Pei, L. Kai-Qun, Y. Jie, and M. Hai, "Photonic Crystal Fibre SERS Sensors Based on Silver Nanoparticle Colloid," *Chinese Physical Letters*, Vol. 25, no. 12, pp. 4473-4475, 2008.**

**[194]** **Z. Sun, X. Fang, L. Zha, T. Cheng, C. Kang, Y. Han, and X. Zhang, "Surface mode enhanced by avoided crossing in microstructure fibers for improved SERS sensing," *Sensors and Actuators B: Chemical*, Vol. 368, pp. 1-8, 2022.**

**[195]** **M. Li, M. Yan, B. Xu, C. Zhao, D. Wang, Y. Wang, and H. Chen, "A dual-mode optical fiber sensor for SERS and fluorescence detection in liquid," *Spectrochimica Acta Part A: Molecular and Biomolecular Spectroscopy*, Vol. 290, pp. 1-6, 2023.**

**[196]** **D. Zheng, F. Pisano, L. Collard, A. Balena, M. Pisanello, B. Spagnolo, R. Mach-Batlle, F. Tantussi, L. Carbone, F. De Angelis, M. Valiente, L. M. de la Prida, C. Ciraci, M. De Vittorio, and F. Pisanello, "Toward Plasmonic Neural Probes: SERS Detection of Neurotransmitters through Gold-Nanoislands-Decorated Tapered Optical Fibers with Sub-10 nm Gaps," *Advanced Materials*, Vol. 35, no. 1-10, 2023.**

**[197]** **D. Zheng, M. F. Kashif, L. Piscopo, L. Collard, C. Ciraci, M. De Vittorio, and F. Pisanello, "Tunable Nanoislands Decorated Tapered Optical Fibers Reveal Concurrent Contributions in Through-Fiber SERS Detection," *ACS Photonics*, Vol. 11, no. 9, pp. 3774-3783, 2024.**

**[198]** **A. Lucotti and G. Zerbi, "Fiber-optic SERS sensor with optimized geometry," *Sensors and Actuators B*, Vol. 121, pp. 356-364, 2006.**

**[199]** **J. Cao, D. Zhao, X. Lei, Y. Liu, and Q. Mao, "One-pot hydrothermal synthesis of silver nanoplates on optical fiber tip for surface-enhanced Raman scattering," *Applied Physics Letters*, Vol. 104, no. 20, [201906], 2014.**

**[200]** **J. Cao and J. Wang, "Development of Ag nanopolyhedra based fiber-optic probes for high performance SERS detection," *New Journal of Chemistry*, Vol. 39, no. 4, pp. 2421-2424, 2015.**

**[201]** **S. Liu, J. Huang, Z. Chen, N. Chen, F. Pang, T. Wang, and L. Hu, "Raman spectroscopy measurement of levofloxacin lactate in blood using an optical fiber nano-probe," *Journal of Raman Spectroscopy*, Vol. 46, no. 2, pp. 197-201, 2015.**

**[202]** **Z. Huang, X. Lei, Y. Liu, Z. Wang, X. Wang, Z. Wang, Q. Mao, and G. Meng, "Tapered optical fiber probe assembled with plasmonic nanostructures for surface-enhanced Raman scattering application," *ACS Applied Materials and Interfaces*, Vol. 7, no. 31, pp. 17247-17254, 2015.**

**[203]** **J. Cao, D. Zhao, and Y. Qin, "Novel strategy for fabrication of sensing layer on thiol-functionalized fiber-optic tapers and their application as SERS probes," *Talanta*, Vol. 194, pp. 895-902, 2019.**

**[204]** **G. Zhu, L. Singh, Y. Wang, R. Singh, B. Zhang, F. Liu, B. K. Kaushik, and S. Kumar, "Tapered Optical Fiber-Based LSPR Biosensor for Ascorbic Acid Detection," *Photonic Sensors*, Vol. 11, no. 4, pp. 418-434, 2021.**

**[205]** **W. Zhengkun, Y. Zhinan, W. Ning, G. Yong, and Z. Jie, "Raman enhancement mechanism and experiments of cavity-enhanced AgNP decorated tapered fiber sensor," Optics Letters, Vol. 46, no. 17, pp. 4300-4303, 2021.**

**[206]** **Y. Liu, R. Liu, C. Ai, B. Wang, R. Chu, H. Wang, L. Shui, and F. Zhou, "Stick-slip-motion-assisted interfacial self-assembly of noble metal nanoparticles on tapered optical fiber surface and its application in SERS detection," *Applied Surface Science*, Vol. 602, pp. 1-7, 2022.**

**[207]** **A. H. C. Van Bruggen, M. M. He, K. Shin, V. Mai, K. C. Jeong, M. R. Finckh, and J. G. Morris Jr, "Environmental and health effects of the herbicide glyphosate," *Science of The Total Environment*, Vol. 616-617, pp. 255-268, 2018.**

**[208]** **P. Ingaramo, R. Alarcon, M. Munaz-de-Toro, and E. H. Luque, "Are glyphosate and glyphosate-based herbicides endocrine disruptors that alter female fertility? *Molecular and Cellular Endocrinology*, Vol. 518, no. 3, pp. 1-12, 2020.**

**[209]** **S. Thonprakaisang, A. Thiantanawat, N. Rangkadilok, T. Suriyo, and J. Satayavivad, "Glyphosate induces human breast cancer cells growth via estrogen receptors," *Food and Chemical Toxicology*, Vol. 59, pp. 129-136, 2013.**

**[210]** **L. Mikac, I. Rigo, M. Skrabic, M. Ivanda, and M. Veres, "Comparison of Glyphosate Detection by Surface-Enhanced Raman Spectroscopy Using Gold and Silver Nanoparticles at Different Laser Excitations," *Molecules*, Vol. 27, no. 18, pp. 1-14, 2022.**

**[211]** **F. B. Fuenzalida, P. Slepcikova, M. Repovska, A. Jutkova, M. V. Canamares, P. Miskovsky, Z. Jurasekova, and S. Sanchez-Cortes, "Selective and ultrasensitive detection of the herbicide glyphosate by means of plasmon catalysis on Ag nanoparticles," *Spectrochimica Acta Part A: Molecular and Biomolecular Spectroscopy*, Vol. 323, pp. 1-13, 2024.**

**[212]** **R. Eleodoro De Goes, M. Muller, and J. L. Fabris, "Spectroscopic Detection of Glyphosate in Water Assisted by Laser-Ablated Silver Nanoparticles," *Sensors*, Vol. 17, no. 5, pp. 1-15, 2017.**

**[213]** **B. R. Heidemann, I. Chiamenti, M. M. Oliveira, M. Muller, and J. L. Fabris, "Functionalized Long Period Grating-Plasmonic Fiber Sensor Applied to the Detection of Glyphosate in Water," *Journal of Lightwave Technology*, Vol. 36, no. 4, pp. 863-870, 2018.**

**[214]** **G. Alberti, S. Spina, F. Arcadio, M. Pesavento, L. De Maria, N. Cennamo, L. Zeni, and D. Merli, "MIP-Assisted 3-Hole POF Chip Faced with SPR-POF Sensor for Glyphosate Detection,". *Chemosensors*, Vol. 11, no. 7, pp. 1-13, 2023.**

**[215]** **F. Sequeira, S. Reis, R. Oliveira, M. I. S. Verissimo, M. T. S. dos Reis Gomes, A. Rudnitskaya, and L. Bilro, "Glyphosate Detection Through Piezoelectric and Fiber Optic Sensors Based on Molecular Imprinted Polymers," *IEEE Sensors Journal*, Vol. 24, no. 13, pp. 20331-20342, 2024.**

**[216]** **G. V. de Andrade Silva, G. D. Arend, A. A. Zielinski, M. D. Luccio, and A. Ambrosi, "Xanthohumol properties and strategies for extraction from hops and brewery residues: A review," Food Chemistry, Vol. 404, no. 2, pp. 1-10, 2023.**

**[217]** **D. P. Killeen, D. H. Andersen, R. A. Beatson, K. C. Gordon, and N. B. Perry, "Vibrational Spectroscopy and Chemometrics for Rapid, Quantitative Analysis of Bitter Acids in Hops (Humulus Lupulus)," *Journal of Agricultural and Food Chemistry*, Vol. 62, no. 52, pp. 12521-12528, 2014.**

**[218]** **J. A. Yael, J. D. Fuhr, G. A. Bocan, A. D. Millone, N. Tognalli, M. Dos Santos Afonso, and M. L. Martiarena, "Abiotic Degradation of Glyphosate into Aminomethylphosphonic Acid in the Presence of Metals," *Journal of Agricultural and Food Chemistry*, Vol. 62, no. 40, pp. 9651-9656, 2014.**

**[219]** **J. C. S. Costa, R. A. Ando, A. C. Sant'Ana, and P. Corio, "Surface-enhanced Raman spectroscopy studies of organophosphorous model molecules and pesticides," *Physical Chemistry Chemical Physics*, Vol. 14, no. 45, 15645-15651, 2012.**

**[220]** **D. P. Killeen, O. C. Watkins, C. E. Sansom, D. H. Anderson, K. C. Gordon, and N. B. Perry, "Fast Sampling, Analyses and Chemometrics for Plant Breeding: Bitter Acids, Xanthohumol and Terpenes in Lupulin Glands of Hops (Humulus lupulus)," *Photochemical Analysis*, Vol. 28, no. 1, pp. 50-57, 2016.**

**[221]** **A. Grudniewska and J. Poplonski, "Simple and green method for the extraction of xanthohumol from spent hops using deep eutectic solvents," *Separation and Purification Technology*, Vol. 250, pp. 1-7, 2020.**